

Calculation of the Radiative Lifetime and Optical Properties for Three-dimensional (3D) Hybrid Perovskites.

Khaled Shehata Baiuomy Mohammad
(1133140@students.wits.ac.za)
Supervised by: Professor Alexander Quandt.
Co-Supervisor: Dr. Robert Warmbier.
University of Witwatersrand

June 2016

*A dissertation submitted for the fulfilment of the requirements of the degree of Master of Science
to the Faculty of Science, Witwatersrand University*



Declaration

This work was carried out at the University of Witwatersrand, Johannesburg. It is being submitted for the fulfilment of the requirements of the degree of Master of Science.

I hereby declare that except where due acknowledgement is made, this work has never been presented wholly or in part for the award of a degree at any other University.

Student: Khaled Shehata Baiuomy Mohamad



Supervisor: Prof. Alexander Quandt

Co-supervisor: Dr. Robert Warmbier

Abstract

The combination of effective numerical techniques and scientific intuition to find new and novel types of materials is the process used in the discovery of materials for future technologies. Adding to that, being able to calculate the radiative lifetimes of excitons, exciton properties, and the optical properties by using efficient numerical techniques gives an estimation and identification of the best candidate materials for a solar cell. This approach is inexpensive and stable. Present ab initio methods based on Many-body perturbation theory and density functional theory are capable of predicting these properties with a high enough level of accuracy for most cases.

The electronic properties calculated using GaAs as a reference system and the 3D hybrid perovskite $CH_3NH_3PbI_3$ are based on density functional theory. The optical properties are investigated by calculating the dielectric function. The theoretical framework of the radiative lifetime of excitons and calculating the exciton properties are based on Wannier model of the exciton and the Bethe-Salpeter equation.

Acknowledgements

First of all, I thank God and praise Him for helping me and giving me this opportunity to do my Masters' degree at Witwatersrand University, Physics school. This Master has been one of the most important and formative experiences in my life and I thank Him for completing and for doing something that I like.

Special thanks to my supervisor, Prof. Alexander Quandt and my Co-supervisor, Dr. Robert Warmbier for persevering with me as my advisors and supporting me throughout the time it took me to complete this research and write this dissertation.

I must acknowledge as well the many friends and colleagues who assisted, advised, and supported my research and writing efforts.

Contents

Declaration	i
Abstract	ii
Acknowledgements	iii
1 Introduction	1
1.1 Introduction	1
1.2 Motivation and Aim	1
1.3 Hypothesis and Questions	2
1.4 Objectives	2
1.5 Tools	2
1.5.1 Quantum Espresso	3
1.5.2 Yambo	3
1.6 Methodology	3
2 Theoretical approach	5
2.1 Introduction	5
2.2 Many body systems	5
2.3 Density Functional Theory (DFT)	6
2.3.1 Hohenberg-Kohn Theorems	6
2.3.2 Kohn-Sham equations	7
2.4 Exchange and correlation functionals	8
2.4.1 Local Density Approximation (LDA)	8
2.4.2 Generalized Gradient Approximation (GGA)	8
2.5 k-points	9
2.6 Plane wave basis sets	10
2.6.1 Truncating the plane wave expansion	10
2.6.2 Pseudopotentials	10
2.7 The dielectric function	11
2.8 Local field effects	12
3 Many body perturbation theory	13
3.1 Introduction	13
3.2 Quasiparticles	13
3.3 Green's function method	14
3.3.1 The single particle Green's function	14
3.3.2 Dyson equation	16
3.4 Self-energy and the GW approximation	17
3.4.1 Hedin's equation	17
3.4.2 Random Phase Approximation (RPA)	19

3.4.3	Plasmon Pole Approximation (PPA)	20
3.4.4	Solving Dyson's equation	21
3.5	The Bethe-Salpeter equation (BSE)	21
3.6	Solving the Bethe-Salpeter equation	23
4	Exciton models and lifetimes.	28
4.1	Excitons	28
4.1.1	The Wannier exciton	28
4.2	Optical transition	29
4.2.1	Fermi's golden rule	29
4.2.2	Electric dipole approximation	31
4.3	Basic properties that enter the exciton lifetime	32
4.3.1	Wannier approach with Fermi's golden rule.	32
4.3.2	Evaluating the dipole matrix elements that enter the exciton lifetime in the Wannier approach	35
4.3.3	Bethe Salpeter approach with Fermi's golden rule	36
5	Results	37
5.1	GaAs	37
5.1.1	Crystal Structure	37
5.1.2	Band structure and the band gap of GaAs	38
5.1.3	Extracting the effective mass of an exciton from the band structure	39
5.1.4	The static dielectric constant	40
5.1.5	Absorption Spectrum	40
5.1.6	Exciton analysis	44
5.2	$\alpha - CH_3NH_3PbI_3$	52
5.2.1	Crystal Structure	52
5.2.2	Band structure and the band gap of $\alpha - CH_3NH_3PbI_3$	53
5.2.3	Extracting the effective mass of an exciton from the band structure	55
5.2.4	The static dielectric constant	55
5.2.5	Absorption Spectrum.	55
5.2.6	Exciton analysis	57
6	Summary and Discussion	61
6.1	Summary and conclusion	61
6.1.1	Basic Calculations	61
6.1.2	Exciton analysis	62
6.1.3	The theoretical framework for calculating the radiative lifetime of the excitons	62
6.2	Future work	62
A	Many-body perturbation theory and Bethe-Salpeter equation implementation.	63
A.0.1	GWA and QP corrections	64
A.0.2	Bethe Salpeter equation (BSE) and the solution of the BS matrix	67
B	Convergence test of $\alpha - CH_3NH_3PbI_3$	70
B.1	Convergence test for system dependent parameters at the ground states calculation	70
B.1.1	Convergence test with respect to cut off energy	70
B.1.2	Convergence test with respect to k-points	70
B.2	Convergence test for system dependent parameters at the excited states calculation	70

B.2.1	Convergence test for the parameters that are responsible for calculating the static dielectric function	73
B.2.2	Convergence test for the parameters that are responsible for establishing BS Kernel.	73
C	The relation between the matrix elements of a momentum operator and the matrix elements of a position vector	81
	References	87

Chapter 1

Introduction

1.1 Introduction

The search for alternative energy resources is necessary because the conventional energy resources are finite and will be depleted. In addition some of them are a big threat to the environment and public health causing global warming, green house effect, acid rain and are very costly to mine and produce. In contrast, the renewable energy resources such as wind and solar energy, which are by definition constantly replenished as well as have a much lower environmental impact. Most renewable energy comes either directly or indirectly from the sun. Research is still being conducted to develop materials with high absorption efficiency and low cost to make photovoltaic technologies more effective and allowed choice to cover energy needs.

In this work we are concerned with photovoltaic (Solar cell) systems, specifically excitonic solar cells. They are a promising research area where researchers use quantum dots, dye molecules, or polymers to improve the efficiency of solar cells [1]. Excitonic solar cells are advantageous because the polymers, dyes and quantum dots used to make these cells in the are good absorbers of light. As such, these cells require only a very thin film (100 nm or so) to capture the minimum amount of incident light. This means that these cells are relatively cheap to manufacture a large area devices using simple processes, namely screen and ink-jet printing, roll to roll processing and spin coating [1]. Consequently, these solar cells could be prepared as relatively cheap, flexible devices. Additionally, these types of solar cells perform well under low or diffuse light conditions, can be used indoors due to their strong absorption properties [1].

Excitonic solar cells derive their name from the short-lived quasiparticles called excitons, which are created upon absorption of light. These excitons are bound electron-hole pairs with a neutral overall charge. In the excitonic solar cells the electric current is produced by the diffusion of the exciton into the adjacent charge carrier materials. Therefore, the charges are separated and migrate to different electrodes. For the solar cell to achieve efficient conversion, a high photon absorption rate and a long exciton lifetime is required [2]. The exciton lifetime is the main characteristic of an exciton. It is the time taken for the process of radiative recombination. Information on the lifetimes is useful in understanding the decay mechanism and the nature of the optical excitation, as it has a strong impact on the efficiency of photovoltaic cells.

1.2 Motivation and Aim

One of the challenges of current solar panels is to increase their efficiency in converting light energy to electrical energy. It is therefore necessary to examine new ways to optimize this process. The basic energy conversion process consists of four steps : Exciton generation by an incoming

photon, exciton energy transfer, charge separation of the exciton and injection into electrodes. For the first two steps, an efficient energy conversion requires both a high photon absorption rate and long exciton lifetime [2]. In particular long exciton lifetimes are crucial for efficient photovoltaic cells. The determination of radiative lifetimes is an important factor to understand the nature of the optical excitations and their applications in solar cell design, opto-electronics and photonics.

The aim of this project is to propose a general theoretical framework to determine the radiative lifetime and the optical properties of three dimensional (3D) hybrid perovskite $CH_3NH_3PbI_3$ and to carry out numerical studies of the materials properties involved. Perovskites are found to have very high electron and hole mobilities [3]. Therefore these materials have been used to improve the efficiency of dye sensitized solar cells (DSSC), which is providing the way to a new class of low-cost solar cells [4].

The methodology is to start with GaAs as a reference system to test the basics procedures of the whole calculation. This will give us some information about the quality of the results and the computational resources that we will need to perform the same calculation for $CH_3NH_3PbI_3$.

1.3 Hypothesis and Questions

Presently, excitonic solar cells are less efficient and have shorter lifetimes than the traditional silicon based solar cell. Recently, the excitonic solar cells have been brought onto the commercial market and thus there is a large focus now on overcoming the limitations given above [2]. 3D hybrid perovskites have been suggested as new materials for DSSC. This lead them to a new class of Hybrid Semiconductor Photovoltaic Cells (HSPC) [5]. The long term goal is to reduce the cost and increase their efficiencies in order to make photovoltaic technologies more effective and the preferred choice to cover energy needs. The best performance of the solar cells at the time of writing have been obtained with technologies like $III - V$ silicon multiple junction cells under conditions of concentrated light but they require sophisticated technologies to implement. The following references provide more information on this interesting topic [5][4]. Therefore, being able to calculate the radiative lifetime and optical properties of 3D hybrid perovskites by using well tested and efficient numerical techniques is very important and is a rather inexpensive approach to study the basic material aspects involve. The efficiency of a solar cell material can be estimated on the basis of numerical data and this will allow for the identification of the best candidate materials for a solar cell.

1.4 Objectives

The objectives of this project are as follows :

1. Numerically studying the structure of GaAs to test the quality of the computational methods being used. Afterwards (3D) hybrid perovskite $\alpha - CH_3NH_3PbI_3$ will be studied using the same techniques. We will focus on exciton states and on the optical properties.
2. Understanding the theory for calculating the radiative lifetime of excitons and study the basics materials properties involved for GaAs and perosvskite $\alpha - CH_3NH_3PbI_3$.

1.5 Tools

The numerical study is based on Many-Body Perturbation Theory (MBPT) and Time Dependent Density Function Theory (TD-DFT). We use these methods to examine quasiparticles and the

optical properties of many-electron systems. We can also study the basic materials properties to calculate the radiative lifetime of (3D) hybrid perovskites. Efficient numerical techniques are included in the Yambo package [6], which uses the input data from standard Density Function theory (DFT) calculations obtained by means of the Quantum Espresso package [7]. We will also use Python to develop our own numerical tools, whenever necessary.

1.5.1 Quantum Espresso

Quantum Espresso is an open source code, which can simulate the quantum mechanical properties of a material. Quantum Espresso features DFT based on plane wave basis sets and various types of pseudopotentials. Quantum Espresso has the following useful features relevant to this project :

- a) Ground state calculations based on DFT, Kohn-Sham orbitals, implementation of spin-orbit coupling necessary to treat the influence of the heavy lead atoms and non-collinear magnetism.
- b) Structure Optimization [7].

1.5.2 Yambo

Yambo is a computer code, which features MBPT and TD-DFT for solid state and molecular simulations. Yambo relies on the Kohn-Sham eigenstates and eigenvalues generated by a standard DFT calculation, like the ones obtained using the Quantum Espresso package as input [6]. Yambo contains the following useful features to carry out this project :

- a) Quasiparticle energies within the GW approximation [8].
- b) Electron energy loss function, optical absorption spectra of solids and dynamical polarizabilities at different level of theory [9].
- c) Electron-hole wavefunctions and exciton properties based on the Bethe Salpeter equation (BSE).

1.6 Methodology

In this work we are going to carry out basic DFT calculations by using Quantum Espresso, which is based on pseudopotentials. The latter were obtained using The Generalized Gradient Approximation (GGA) included in the Unified Pseudopotential Format (UPF) at version 2.0.1. They are scalar relativistic and norm-conserving for all atoms except lead and iodine, which are treated as fully relativistic including the spin orbital coupling (SOC). For excited state calculation we are going to carry out ab initio calculations to obtain quasiparticles and the optical properties of electronic systems for 3D hybrid perovskites. Quasiparticle energy eigenvalues are determined by the *GW* approximation method [10][11]. The implementation of *GW* approximation in the Yambo package is given in [8]. The exciton states are determined by solving the BSE. The numerical solution of the BSE provides us with the exciton energies and wave functions [2]. The implementation of BSE in the Yambo package is given in [9][12]. We will then discuss the radiative lifetimes calculation of 3D hybrid perovskites as follows :

- a) Using excitons eigenstates from the solution of the BSE we will then apply Fermi's Golden rule to describe the theoretical framework for transition rates and exciton lifetimes. Here, we are going to use the Yambo code.

- b) Calculating dipole matrix elements, which has a direct proportional relation to the transition rates and inverse proportional relation to the lifetimes. These are functions of the electronic band gap and effective masses of electron and hole pairs. Here, we will develop our own code.

Chapter 2

Theoretical approach

2.1 Introduction

Quantum mechanics provides the tools to understand the fundamental properties of matter at the atomic level. The fundamental interactions between ions and electrons characterise the properties of a material, such as optical, electrical, and magnetic properties.

2.2 Many body systems

The core problem of condensed matter physics is the study of complex systems with many atoms and electrons and the manifold interactions between them (Many body system). These systems can be described as follows

$$\hat{\mathbf{H}}(\mathbf{r}_1, \dots, \mathbf{r}_m; \mathbf{R}_1, \dots, \mathbf{R}_N) \Psi(\mathbf{r}_1, \dots, \mathbf{r}_m; \mathbf{R}_1, \dots, \mathbf{R}_N) = E \Psi(\mathbf{R}_1, \dots, \mathbf{R}_N; \mathbf{r}_1, \dots, \mathbf{r}_m), \quad (2.1)$$

where $\hat{\mathbf{H}}$ is the Hamiltonian of the system, Ψ is the wavefunction, $\mathbf{r} = \{\mathbf{r}_i\}$ represents the electron coordinates, $\mathbf{R} = \{\mathbf{R}_j\}$ represents the nuclear coordinates, and E represents the total energy being an eigenvalue of the Schrödinger equation. The Hamiltonian $\hat{\mathbf{H}}$ takes into account all of the interactions between electrons and the nuclei. It is given as

$$\hat{\mathbf{H}}(\{\mathbf{r}, \mathbf{P}\}; \{\mathbf{R}, \mathbf{P}_I\}) = \sum_i \frac{P_i^2}{2m} + \sum_I \frac{P_I^2}{2M_I} + \sum_{i \gtrsim j} \frac{e^2}{|\mathbf{r}_j - \mathbf{r}_j|} - \sum_{i,I} \frac{Z_I e^2}{|\mathbf{r}_i - \mathbf{R}_I|} + \sum_{I \gtrsim J} \frac{Z_I Z_J}{|\mathbf{R}_I - \mathbf{R}_J|}, \quad (2.2)$$

where m represents the electron mass, \mathbf{P}_i are the electron momenta, while the nuclei have mass M_I , momentum \mathbf{P}_I , and Z_I being the atomic number [9]. The Hamiltonian in Eq.(2.2), can be rewritten as follows

$$\hat{\mathbf{H}} = \hat{\mathbf{T}}_e + \hat{\mathbf{T}}_n + \hat{\mathbf{V}}_{en} + \hat{\mathbf{V}}_{ee} + \hat{\mathbf{V}}_{nn}. \quad (2.3)$$

where $\hat{\mathbf{T}}_e = \sum_i \frac{P_i^2}{2m}$ is the electronic kinetic energy operator, $\hat{\mathbf{T}}_n = \sum_I \frac{P_I^2}{2M_I}$ is the nuclei kinetic energy operator, $\hat{\mathbf{V}}_{en} = - \sum_{i,I} \frac{Z_I e^2}{|\mathbf{r}_i - \mathbf{R}_I|}$ is the nuclei potential operator, that acts on the electrons, $\hat{\mathbf{V}}_{ee} = \sum_{i \gtrsim j} \frac{e^2}{|\mathbf{r}_j - \mathbf{r}_j|}$ is the electron-electron interaction operator, and $\hat{\mathbf{V}}_{nn} = \sum_{I \gtrsim J} \frac{Z_I Z_J}{|\mathbf{R}_I - \mathbf{R}_J|}$ is the repulsion due to the nucleus-nucleus interaction operator. Because of the large number of interactions, the problem becomes extremely complex. Therefore, we must approximate our system to simplify the problem, refer to [31], [32], and [34]. One of these approximations is the Born-Oppenheimer or adiabatic approximation. This approximation considers only the movement of electrons, assuming that ions are much heavier and so will seem to be at rest when compared to the electrons [30].

2.3 Density Functional Theory (DFT)

DFT has become a primary tool for calculating the properties of many-electron systems in condensed matter, molecules and mesoscopic systems. In DFT, any property of many body system is related to the ground state electron density $n_0(\mathbf{r})$ [13]. Currently, there are many ab initio codes to perform DFT calculations. The one being considered here is Quantum Espresso. The latter uses the plane-wave basis sets and pseudopotentials [7]. What follows is a brief discussion and description of DFT.

2.3.1 Hohenberg-Kohn Theorems

Hohenberg-Kohn proved two theorems, where DFT is based upon them [32][33]. They can be applied to any interacting electrons system subjected to an external potential $V_{ext}(\mathbf{r})$. The Theorems are given as follows :

Theorem I : For an interacting electrons system in an external potential $V_{ext}(\mathbf{r})$. There is one-to-one correspondence between a Hamiltonian with external potential $V_{ext}(\mathbf{r})$ and the ground state density $n_0(\mathbf{r})$, up to a constant [32].

Proof I : Assume we have a many body system subject to two different external potentials $V_{ext}^{(1)}$ and $V_{ext}^{(2)}$ with the following Hamiltonians and ground state wavefunctions associated with each potential : $\hat{\mathbf{H}}^{(1)}$, $\hat{\mathbf{H}}^{(2)}$, and $\Psi^{(1)}$, $\Psi^{(2)}$. Let us further assume now that the wavefunctions have the same ground state density $n_0(\mathbf{r})$. Since the Hamiltonian related to the ground state wavefunction $\Psi^{(1)}$ is $\hat{\mathbf{H}}^{(1)}$ and according to the related variational principle, no wavefunction is able to have an energy that is less than the energy of $\Psi^{(1)}$ with respect to $\hat{\mathbf{H}}^{(1)}$. This gives

$$E^{(1)} = \langle \Psi^{(1)} | \hat{\mathbf{H}}^{(1)} | \Psi^{(1)} \rangle < \langle \Psi^{(2)} | \hat{\mathbf{H}}^{(1)} | \Psi^{(2)} \rangle. \quad (2.4)$$

The ground state is assumed to be non-degenerate, and thus there is inequality holds strictly. The expectation value of the last term in Eq.(2.4) can be written as

$$\begin{aligned} \langle \Psi^{(2)} | \hat{\mathbf{H}}^{(1)} | \Psi^{(2)} \rangle &= \langle \Psi^{(2)} | \hat{\mathbf{H}}^{(2)} | \Psi^{(2)} \rangle + \langle \Psi^{(2)} | \hat{\mathbf{H}}^{(1)} - \hat{\mathbf{H}}^{(2)} | \Psi^{(2)} \rangle \\ &= E^{(2)} + \int d^3\mathbf{r} [V_{ext}^{(1)}(\mathbf{r}) - V_{ext}^{(2)}(\mathbf{r})] n_0(\mathbf{r}), \end{aligned} \quad (2.5)$$

Similarly

$$E^{(2)} = \langle \Psi^{(2)} | \hat{\mathbf{H}}^{(2)} | \Psi^{(2)} \rangle < \langle \Psi^{(1)} | \hat{\mathbf{H}}^{(2)} | \Psi^{(1)} \rangle. \quad (2.6)$$

and

$$\begin{aligned} \langle \Psi^{(1)} | \hat{\mathbf{H}}^{(2)} | \Psi^{(1)} \rangle &= \langle \Psi^{(1)} | \hat{\mathbf{H}}^{(1)} | \Psi^{(1)} \rangle + \langle \Psi^{(1)} | \hat{\mathbf{H}}^{(2)} - \hat{\mathbf{H}}^{(1)} | \Psi^{(1)} \rangle \\ &= E^{(1)} + \int d^3\mathbf{r} [V_{ext}^{(2)}(\mathbf{r}) - V_{ext}^{(1)}(\mathbf{r})] n_0(\mathbf{r}), \end{aligned} \quad (2.7)$$

Note that the above equations imply that $\Psi^{(1)}$ and $\Psi^{(2)}$ give rise to the same ground state density $n_0(\mathbf{r})$. Adding Eq.(2.5) and Eq.(2.7), we find that

$$E^{(1)} + E^{(2)} < E^{(2)} + E^{(1)}. \quad (2.8)$$

where $E^{(1)}$ and $E^{(2)}$ represent the ground state energies corresponding to $\hat{\mathbf{H}}^{(1)}$ and $\hat{\mathbf{H}}^{(2)}$ respectively. At this point, we arrive at a contradiction. As a result, the ground state density is the one-to-one correspondence with a Hamiltonian with $V_{ext}(\mathbf{r})$ up to a constant [13].

Theorem II : A universal functional for the energy $E[n]$ in terms of density $n(\mathbf{r})$ can be defined, valid for any external potential $V_{ext}(\mathbf{r})$. For any particular $V_{ext}(\mathbf{r})$, the exact ground state energy of the system is the global minimum value of this functional, and the density $n(\mathbf{r})$ that minimizes the functional is the exact ground state density $n_0(\mathbf{r})$ [32][33].

Proof II : As we proved in theorem I, a Hamiltonian with the external potential is uniquely determined by the ground state density, and the Hamiltonian in turn determines the ground state wavefunction (except in degenerate conditions). Since all the system properties written are uniquely determined if $n(\mathbf{r})$ is specified, then each property can be a functional of $n(\mathbf{r})$, which leads to the following total energy

$$\begin{aligned} E[n] &= T[n] + E_{intr}[n] + \int V_{ext}(\mathbf{r}) n(\mathbf{r}) \\ &\equiv F[n] + \int V_{ext}(\mathbf{r}) n(\mathbf{r}), \end{aligned} \quad (2.9)$$

where $T[n]$ represents the kinetic energy, and $E_{intr}[n]$ represents the interaction energy between the electrons. The functional $F[n]$ includes all internal energies of the interacting electron system, such as kinetic and potential energies. As long as the kinetic and interaction energies are a functional of the density only, $F[n]$ must be a universal functional by construction [13]. Following the discussion in theorem I. If a system has a ground state density $n^{(1)}(\mathbf{r})$ corresponding to a Hamiltonian $\hat{H}^{(1)}$ with external potential, a distinct wavefunction $\Psi^{(1)}$ results, which has the ground state energy

$$E^{(1)} = E[n^{(1)}] = \langle \Psi^{(1)} | \hat{H}^{(1)} | \Psi^{(1)} \rangle.$$

Finally, consider a different density $n(\mathbf{r})$ corresponding to different wavefunction $\Psi^{(2)}$. By the variation principle, a different density $n^{(2)}(\mathbf{r})$ will necessary give a higher energy

$$E^{(1)} = E[n^{(1)}] = \langle \Psi^{(1)} | \hat{H}^{(1)} | \Psi^{(1)} \rangle < \langle \Psi^{(2)} | \hat{H}^{(1)} | \Psi^{(2)} \rangle = E^{n^{(2)}}. \quad (2.10)$$

If the $F[n]$ of the system was known, it follows that by minimizing the total energy with respect to the density function $n(\mathbf{r})$, we obtain the exact ground state energy and density.

The Hohenberg-Kohn Theorems (HK) postulate the existence of the universal functional $F[n]$ without actually determining it, since the approximations for $T[n]$ lead to large errors, and the exact functional is not known. These shed some doubts on the practical side of DFT, but this doubt disappeared when Kohn and Sham introduced their method [13] and [34].

2.3.2 Kohn-Sham equations

Kohn and Sham (KS) assumed that the density of a non-interacting reference system is the same as for the interacting system associated with [34]. Consider a system of N interacting electrons with Hamiltonian $\hat{H} = T + W + V$, where T represents the kinetic term, W represents the interaction with the external field, and V represents the electron-electron interaction. Now consider an auxiliary system of N non-interacting electrons with Hamiltonian $\hat{H} = T' + W'$, where the two system have the same density. W' is the KS potential, which represents the total (effective) potential for a single electron. This potential consists of the external potential, the Hartree potential, and the exchange-correlation potential V_{xc} . The latter potential is a functional of the density, which follow from the Pauli exclusion principle for electrons. In the so-called KS scheme, the density of the auxiliary system is given by the sum of square of the orbitals

$$n(\mathbf{r}) = n(\mathbf{r})' = \sum_i^{\text{occu}} |\phi_i(\mathbf{r})|^2, \quad (2.11)$$

where ϕ_i represents the single particle states of the non-interacting reference system. Using the KS approach for an interacting system, the ground state energy functional expression is re-written in the form

$$E_{KS}[n] = T[n] + E_{ext}[n] + E_{Hartree}[n] + E_{xc}[n], \quad (2.12)$$

where T represents an independent-particle kinetic energy, E_{ext} represents the external energy due to the nuclei or any other external fields, $E_{Hartree}$ represents the coulomb interaction of the electron density interacting with itself, and E_{xc} contains all the many-body effects of the exchange and correlation energy. The $E_{KS}[n]$ is minimized with respect to ϕ_i under the constraint of orthonormal $\{\phi_i\}$. The chain rule is employed for the functional derivatives, where all terms are functionals of the density except T , which is expressed as a functional of the orbitals. This gives

$$\frac{\delta E_{tot}}{\delta \phi_i^*(\mathbf{r})} = \frac{\delta T}{\delta \phi_i^*(\mathbf{r})} + \left[\frac{\delta E_{ext}}{\delta n(\mathbf{r})} + \frac{\delta E_{Hartree}}{\delta n(\mathbf{r})} + \frac{\delta E_{xc}}{\delta n(\mathbf{r})} \right] \frac{\delta n(\mathbf{r})}{\delta \phi_i^*(\mathbf{r})} = \varepsilon_i \phi_i(\mathbf{r}). \quad (2.13)$$

Eq.(2.12) can now be written as

$$-\frac{1}{2}\nabla^2 \phi_i(\mathbf{r}) + [V_{ext}[n] + V_{Hartree}[n] + V_{xc}[n]] \phi_i(\mathbf{r}) = \varepsilon_i \phi_i(\mathbf{r}). \quad (2.14)$$

Eq.(2.14) represents the mean field equations for the non-interacting reference system. These system of equations can be solved self-consistently.

2.4 Exchange and correlation functionals

The term V_{xc} , in Eq.(2.14) and E_{xc} contains exchange and correlation effects for a system of electrons. The exchange-correlation energy is considered to be a crucial quantity in the KS approach, on which the whole accuracy of the DFT calculations depends. This quantity is a functional of the density, i.e. $E_{xc}[n]$. Some popular approximations for E_{xc} are discussed below.

2.4.1 Local Density Approximation (LDA)

LDA was the first and simplest approximation for the exchange and correlation functional, where we assume that the electrons would behave like a homogeneous gas. In this case the effects of the exchange and correlation are local in character. Kohn and Sham made LDA, their E_{xc} is an integral over all space, and assuming that the exchange-correlation energy density is the same as for a homogeneous electron gas at each point [34]

$$E_{xc}^{LDA}[(n\mathbf{r})] = \int \varepsilon_{xc}^{homg}(n(\mathbf{r})) d^3\mathbf{r}. \quad (2.15)$$

where ε_{xc}^{homg} is the exchange-correlation energy in a homogeneous electron gas per electron. The ε_{xc}^{homg} can be accurately computed at any density $n(\mathbf{r})$, using Monte Carlo methods [36]. The LDA formalism has several weaknesses. It underestimates the band gap by up to 50% and it wrongly predicts the magnetic properties of bulk materials, see [37] and [38].

2.4.2 Generalized Gradient Approximation (GGA)

The GGA is another widely used approximation for the exchange and correlation energy. It has marked improvements over LDA for many reasons [13]. It generalizes the Eq.(2.15), which is now defined as follows

$$E_{xc}^{GGA}[n] = \int d^3\mathbf{r} \varepsilon(n, \nabla n), \quad (2.16)$$

where E_{xc}^{GGA} denotes the exchange correlation energy in the GGA model. Obviously, the energy density ε now depends on the gradient of the density as well. This describes an inhomogeneous electron system. Although GGA gives better results for the ground state energies, for predicting molecular geometries, and predicting the magnetic properties of 3D transition metals, see [39], [40] and [41], the GGA has some limitation. It is computationally more expensive than the LDA [41], fails to predict the lattice parameter of graphite correctly, and treats the Hydrogen bond in an incorrect way [42].

2.5 k-points

k-points are a significant parameter in DFT calculation. Many important quantities are determined using a summation over k-points. These points allow us to keep track of and reconstruct $\psi(\mathbf{r})$. k-points are used to sample the first Brillouin zone (1BZ), which is defined as the Wigner-Seitz cell of the reciprocal lattice [13]. The technique that is used to sample the 1BZ is the uniformly spaced Monkhorst-Pack k-point grid [14], which is the most common approach. The Monkhorst-Pack grids are denoted as $N_{k_x} \times N_{k_y} \times N_{k_z}$, where N_{k_i} specify the size of the grid in different directions. The k-point grid is a computationally expensive parameter, which implies that the denser the k-points size, the heavier the computational cost will be. In principle, we need an infinite number of k-points, but practically, we work with finite grids and make a convergence test to get the balance between the computational cost of the calculation and the accuracy of the results. In Fig.(2.1), we show the convergence of k-point grids with respect to the total energy of the system at a fixed cut-off energy for GaAs.

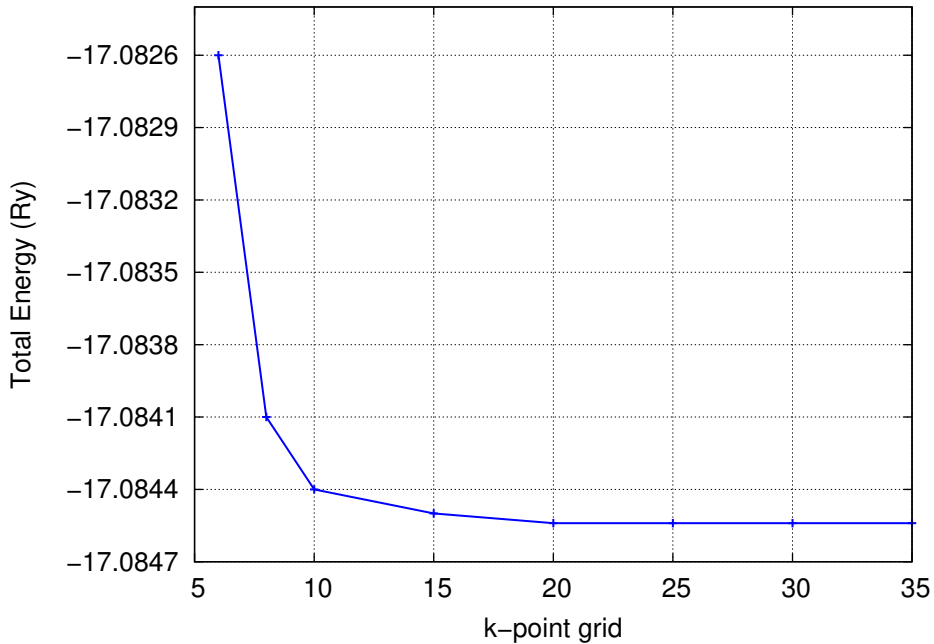


Figure 2.1: Convergence test for k-point grid with different dimensions around Γ with respect to the total energy at a fixed cut-off energy for GaAs.

2.6 Plane wave basis sets

In order to solve the KS equation Eq.(2.14), the wavefunction ψ should be expanded in a basis set

$$\psi_i(r) = \sum_j^{N_b} c_{ij} f_j(r),$$

where c is the weight of the plane wave, N_b is the size of the basis, and $f(r)$ is the basis function. There are popular sets of basis functions, like plane waves, localized set e.g Gaussian and mixed basis sets. Plane waves are commonly used as a basis set, since they allow for easy calculations of derivatives and integrals. The plane wave are also independent of atomic position. Moreover, the method of Fast Fourier Transform (FFT) can be used to rapidly transform our plane wave from r-space to k-space and back. This is essential, because we will use the Bloch wavefunctions for a periodic systems like a solid, which are given as follows

$$\psi_{\mathbf{k}}(r) = e^{i\mathbf{k}\cdot\mathbf{r}} u_{\mathbf{k}}(r), \quad (2.17)$$

where $u_{\mathbf{k}}(r)$ is an amplitude factor with the periodicity of the system. Therefore its Fourier transform can be written as

$$u_{\mathbf{k}}(r) = \frac{1}{\Omega} \sum_{\mathbf{G}} c_{\mathbf{k},\mathbf{G}} e^{i\mathbf{G}\cdot\mathbf{r}}, \quad (2.18)$$

where \mathbf{G} is the reciprocal lattice vector and Ω is the lattice volume. From Eq.(2.17) and Eq.(2.18), the final form of the plane wave expansion for a Bloch state in the periodic system becomes

$$\psi_{\mathbf{k}}(r) = \frac{1}{\Omega} \sum_{\mathbf{G}} c_{\mathbf{k},\mathbf{G}} e^{i(\mathbf{k}+\mathbf{G})\cdot\mathbf{r}}. \quad (2.19)$$

2.6.1 Truncating the plane wave expansion

Every lattice periodic function can be expand into plane waves that involve reciprocal lattice vectors \mathbf{G} . However a larger summation over \mathbf{G} requires long time of computing, so we must determine an appropriate point to terminate the summation in Eq.(2.19). In practice, we will truncate the expansion at some value of $|\mathbf{k} + \mathbf{G}|$. Traditionally, we express this truncating in energy units and it follows the condition $\frac{\hbar^2|\mathbf{k}+\mathbf{G}|^2}{2m} \leq E_{\text{cut}}$. The cut-off energy is the most important parameter in DFT calculations. Checking the convergence of the cut-off energy with respect to the total energy of the system is very important. It will reduce the computational effort without affecting the accuracy of the results and also avoids artefact of unit cell orientation on the numerical results. In Fig.(2.2), we evaluated this convergence at a fixed k-point mesh for GaAs. As one can see, the monotonic behaviour starts in the range of energy from 50 Ry to 60 Ry; a cut-off below 50 Ry is insufficient. We prefer to use the energy cut-off 60 Ry (816 eV) to grantee accurate results.

2.6.2 Pseudopotentials

The Coulomb potential that is experienced by the electrons due to the nuclei leads to computational problems, especially when using plane waves as a basis set for a wavefunction expansion. To avoid this problem we divide the atom into core and valence (orbitals) electrons. The core electrons are forming a rare gas configuration plus full d or f sub-shells. The core electrons wavefunction are sharply peaked near the nucleus, whereas the valence electrons wavefunctions have a lot of wiggles near the nucleus, due to their orthogonality to the core states. In principle this will require high Fourier components, i.e a large cut-off energy. The problem is avoided by using the pseudopotential approximation. In the pseudopotential approximation, the atoms that

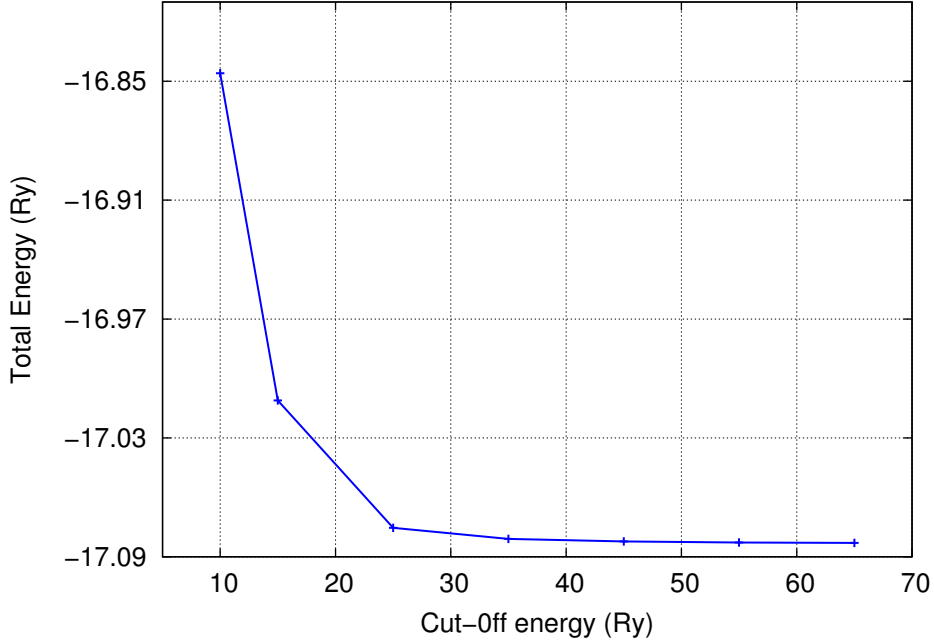


Figure 2.2: Convergence test for cut-off energy with respect to the total energy at a fixed k-point mesh for GaAs.

comprise the chemical system are modified by removing the core electrons degrees of freedom and the valence electrons are described by pseudo-wavefunction, which are relatively smooth compared to the real wavefunctions within the core region, see [15], [16], [17], and [18]. The pseudopotential approximation method has a advantages over all the full potential methods. The most important advantages of the pseudopotential approach comes from making use of the plane waves basis set, as described in [16]. The smooth behaviour of the pseudo-wavefunctions and the strongly related numbers of orbitals significantly reduce the computational cost [19][20][21]. There are typical families of pseudopotentials, these are Projector Augmented Wave (PAW), Ultra-soft, and Norm-conserving types of Pseudopotentials, for more details, refer to [22], [23], [24], [25], and [26].

2.7 The dielectric function

The dielectric properties of a solids are of practical importance since there is a relation between the dielectric properties and the optical properties. For example the complex refractive index is directly related to the dielectric constant by the relation $\tilde{n} = \sqrt{\epsilon}$. A dielectric experiences a polarization that varies linearly with the field, when it is placed in an external field. The constant of proportionality in this process determines the dielectric constant. The dielectric constant is practically independent of frequency at lower frequencies, but at certain frequencies the atoms are able to absorb energy, which are called resonance frequencies or inter-band frequencies in the case of solids. These resonances are often in a visible or ultraviolet range of frequencies. In an external periodically varying electric field with frequencies, the material exhibits a linear response to that field, which is described by frequency dependent dielectric tensor $\epsilon(\omega)$

$$\epsilon(\omega) = \epsilon_1(\omega) + i\epsilon_2(\omega) \quad (2.20)$$

$$\epsilon(\omega) = \begin{vmatrix} \epsilon_{xx} & \epsilon_{xy} & \epsilon_{xz} \\ \epsilon_{yx} & \epsilon_{yy} & \epsilon_{yz} \\ \epsilon_{zx} & \epsilon_{zy} & \epsilon_{zz} \end{vmatrix}.$$

where $\epsilon_{i,j}$ and $i,j = x, y, \text{ or } z$ are the subscripts that correspond to the Cartesian coordinates. The dielectric tensor is symmetric, this implies that $\epsilon_{xy} = \epsilon_{yx}$, $\epsilon_{zx} = \epsilon_{xz}$, and $\epsilon_{zy} = \epsilon_{yz}$. The imaginary part of the dielectric function $\epsilon_2^{i,j}(\omega)$ for each sample frequency is related to the transition energies and the oscillator strength.

$$\epsilon_2^{i,j}(\omega) = \frac{4\pi^2 e^2}{\Omega} \lim_{\mathbf{q} \rightarrow 0} \frac{1}{q^2} \sum_{v,c,\mathbf{k}} 2w_{\mathbf{k}} \delta(E_{c\mathbf{k}} - E_{v\mathbf{k}} - \omega) \cdot \langle u_{c\mathbf{k}+\mathbf{e}_i q} | u_{v\mathbf{k}} \rangle \langle u_{c\mathbf{k}+\mathbf{e}_j q} | u_{v\mathbf{k}} \rangle^*, \quad (2.21)$$

where the transition probability $\langle u_{c\mathbf{k}+\mathbf{e}_i q} | u_{v\mathbf{k}} \rangle$ weight $w_{\mathbf{k}}$ and these weights sum to 1, Ω represents the primitive cell volume, \mathbf{e}_i is the unit vector for three Cartesian direction, q symbolizes the Bloch vector of the incident wave, v and c symbolize the valence and conduction band respectively, and $u_{\mathbf{k}}$ or $u_{v\mathbf{k}}$ symbolizes the cell periodic part of the Bloch states at \mathbf{k} [27]. The real part $\epsilon_1^{i,j}(\omega)$ is determined by using the Kramers-Kronig transformation [27].

$$\epsilon_1^{i,j}(\omega) = 1 + \frac{2}{\pi} P \int_0^\infty \frac{\epsilon_2^{i,j}(\omega') \omega'}{\omega'^2 - \omega^2} d\omega'. \quad (2.22)$$

where P symbolizes a principle value [27]. The dielectric constant can be calculated using a Many Body approach or Density Functional Perturbation Theory (DFPT) approach [28][93].

2.8 Local field effects

When a electromagnetic wave with a wave vector \mathbf{k} is propagating through a crystal. The applied electric field gets modified due to the dipole dipole interactions. Each local dipole has a dipole moment $\mathbf{p}_i = 4\pi\epsilon_0\alpha_i\mathbf{E}_{loc}$, which is proportional to the local field rather than the applied field [29]. Hence, we can define the local field as the quantity that effectively determines the polarization of the electron.

Chapter 3

Many body perturbation theory

3.1 Introduction

Many-body perturbation theory (MBPT) is a semi-analytic method based on the Green's function. There are many codes based on MBPT. The one that we use in our calculation is the Yambo code, which uses the DFT Kohn-Sham (KS) equation as a first approximation for the electronic quasiparticles [6]. The KS equations Eq.(2.14) are

$$\left[-\frac{\nabla^2}{2} + V_{ext}(r) + V_{Hartree}(r) + V_{xc}(r) \right] \phi_i^{KS} = \varepsilon_i^{KS} \phi_i^{KS}.$$

3.2 Quasiparticles

The concept of a quasiparticle is not new to physics. To think about the quasiparticle is to look at an electron moving through a semiconductor. This electron will interact with its surroundings, and consequently shall undergo some form of a perturbation. This new interacting electron is called a quasiparticle, since it behaves in a manner that differs slightly from that of a free electron. The idea of the quasiparticle is better described by Fig(3.1), where every electron is screened by the coulomb forces surrounding its neighbouring electrons. This is similar to the non-interacting reference systems suggested by Kohn and Sham. Describing the interacting particle system by a weakly interacting quasiparticle system can be done by using a mathematical method called the Green's function method [9]. The latter will be described in the following sections in more detail. There is a physical process that allows us to distinguish between a quasiparticle and a bare particle in condensed matter physics. This physical process is the polarization of the surrounding medium, which leads to the screening of quasiparticles [6]. One method of determining the excitation of the quasiparticles is the MBPT method in the GW approximation. It is considered to be an accurate approach for determining the correct electronic band gaps of many systems [46].

The quasiparticle energies E_i and their wavefunctions ψ_i in MBPT can be obtained by solving the following Schrödinger like equation [9]

$$\left(\frac{1}{2} \nabla^2 + V_{Hartree}(\mathbf{r}) + V_{ext}(\mathbf{r}) \right) \psi_i(\mathbf{r}, \omega) + \int d\mathbf{r}' \Sigma(\mathbf{r}, \mathbf{r}', \omega) \psi_i(\mathbf{r}', \omega) = E_i(\omega) \psi_i(\mathbf{r}, \omega). \quad (3.1)$$

The difference between the free particle energy and the quasiparticle energy is given by the operator $\Sigma(\mathbf{r}, \mathbf{r}', \omega)$, which is called the self-energy operator. It is energy dependent, a non-Hermitian, non-local operator, and includes exchange and correlation effects.

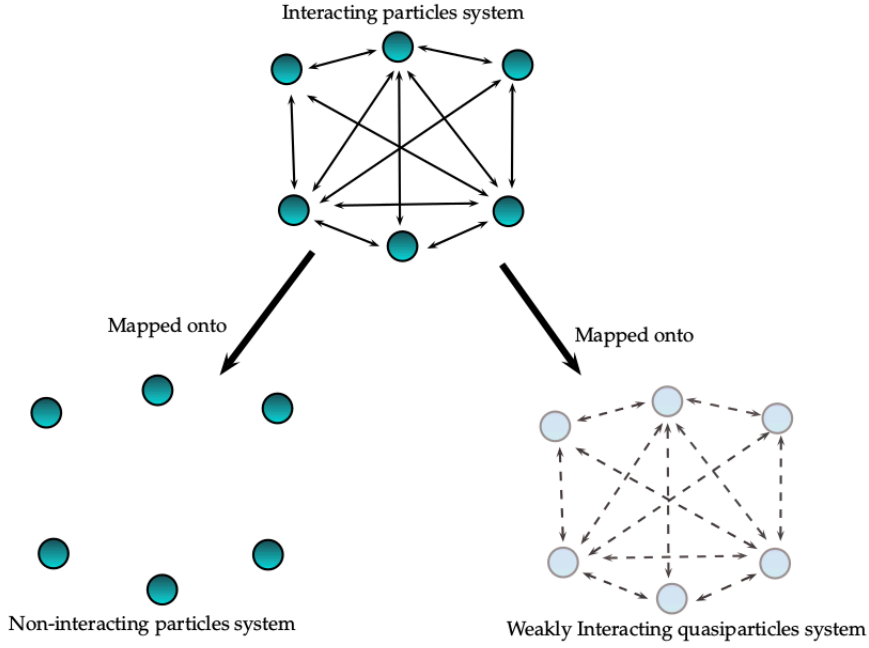


Figure 3.1: An interacting particle system in KS theory (left), and Green's function approach (right).

3.3 Green's function method

The Green's function method is a very useful technique. It has the ability to tackle problems like excitation calculation, ground state energies, polarizability, photoemission spectra, and absorption spectra.

3.3.1 The single particle Green's function

We can use the single particle Green's function to determine some of the quasiparticle's properties such as energies, lifetimes, and some expectation values of a single particle with respect to the many-electron ground state like the density and the total energy of the system [47]. The single particle Green's function is defined by the following equation

$$G(\mathbf{r}_1 t_1, \mathbf{r}_2 t_2) = -i \langle N | \hat{T} [\hat{\psi}(\mathbf{r}_1, t_1) \hat{\psi}^\dagger(\mathbf{r}_2, t_2)] | N \rangle, \quad (3.2)$$

where $|N\rangle$ represents the ground state of N interacting electrons, $\hat{\psi}$ and $\hat{\psi}^\dagger$ represent the creation and annihilation operators that act on N electrons. The matrix element in Eq.(3.2) is in the Heisenberg picture, \hat{T} symbolizes the time ordering operator and the particle has five coordinates : \mathbf{x} for three spatial coordinates, a spin coordinate $\sigma = \pm \frac{1}{2}$ and t as time. In Eq.(3.2), the expression $\hat{\psi}^\dagger(\mathbf{r}, t) | N \rangle$ describes the process of adding an electron to the system at point \mathbf{r} and time t to form state $|N + 1\rangle$. The time ordering operator between two operators $\hat{\psi}^\dagger$ and $\hat{\psi}$ is defined as

$$\hat{T} [\hat{\psi}(\mathbf{r}_1, t_1), \hat{\psi}^\dagger(\mathbf{r}_2, t_2)] = \begin{cases} \hat{\psi}(\mathbf{r}_1, t_1) \hat{\psi}^\dagger(\mathbf{r}_2, t_2) & \text{if } t_1 > t_2 \\ -\hat{\psi}^\dagger(\mathbf{r}_2, t_2) \hat{\psi}(\mathbf{r}_1, t_1) & \text{if } t_1 < t_2, \end{cases}$$

and the commutation relation between $\hat{\psi}^\dagger$ and $\hat{\psi}$ is

$$\begin{aligned} [\hat{\psi}(\mathbf{r}_1, t_1), \hat{\psi}^\dagger(\mathbf{r}_2, t_2)] &= \delta(\mathbf{r}_1 - \mathbf{r}_2) \delta(t_1 - t_2) \\ [\hat{\psi}(\mathbf{r}_1, t_1), \hat{\psi}(\mathbf{r}_2, t_2)] &= [\hat{\psi}^\dagger(\mathbf{r}_1, t_1), \hat{\psi}^\dagger(\mathbf{r}_2, t_2)] = 0, \end{aligned} \quad (3.3)$$

where $\tau = (t_1 - t_2)$. According to this expression, if $t_1 < t_2$, then Eq.(3.2) gives the probability amplitude of an electron propagate from position \mathbf{x}_1 at time t_1 to position \mathbf{x}_2 at time t_2 , at which the electron has been added in the electronic state $(N + 1)$. If $t_1 > t_2$, then Eq.(3.2) will describe the a hole propagation from which the electron has been removed in the electronic state $(N - 1)$. Following the last discussion, we can call the Green's function the propagator. The Green's function in Eq.(3.2) can be expressed as

$$G(1, 2) = -i\langle \Psi^N | \hat{T} [\hat{\psi}(1)\hat{\psi}^\dagger(2)] | \Psi^N \rangle. \quad (3.4)$$

where we used the ground state Ψ^N instead of $|N\rangle$. Once the Green's function is known, we can evaluate any single particle operator acting on the system and get some useful information about the charged excitation of the system by using the Lehmann representation, refer to [43], [44] and [45]. Before we introduce the Lehmann representation, we should first introduce the notations and the quantities that are used in this representation. The eigenstates $|N \pm 1\rangle$ of the system between the field operators in Eq.(3.2), are called Lehmann amplitudes. In the Schrödinger picture, they are defined as

$$\psi_i^{N-1}(\mathbf{r}) = \langle \Psi_i^{N-1} | \hat{\psi}(\mathbf{r}) | \Psi_0^N \rangle = |N - 1\rangle, \quad (3.5)$$

and

$$\psi_i^{N+1}(\mathbf{r}) = \langle \Psi_0^N | \hat{\psi}(\mathbf{r}) | \Psi_i^{N+1} \rangle = |N + 1\rangle,$$

The eigenvalues of the above eigenstates are the excitation energies, which are defined as

$$\epsilon_i^{N-1} = E_0^N - E_i^{N-1}, \quad \epsilon_i^{N+1} = E_i^{N+1} - E_0^N. \quad (3.6)$$

where $N \pm 1$ label the excited states and E_0^N represents the ground state energy. Now, the Lehmann representation of the Green's function is

$$G(\mathbf{r}_1, \mathbf{r}_2, \omega) = \sum_i \frac{\psi_i^{N+1}(\mathbf{r}_1)\psi_i^{*(N+1)}(\mathbf{r}_2)}{\hbar\omega - (E_i^{N+1} - E_0^N) + i\eta} + \sum_i \frac{\psi_i^{N-1}(\mathbf{r}_1)\psi_i^{*(N-1)}(\mathbf{r}_2)}{\hbar\omega - (E_i^{N-1} - E_0^N) - i\eta}. \quad (3.7)$$

where an infinitesimal imaginary part $i\eta$ is used to ensure the Fourier transform convergence in frequency space, E_i^{N+1} and E_i^{N-1} represent the excitation energy corresponding to a $N + 1$ particle state and $N - 1$ particle state respectively. $\psi_i^{N+1}(\mathbf{r})$ and $\psi_i^{N-1}(\mathbf{r})$ are their corresponding wavefunctions of the system.

Unfortunately, the Lehman representation does not provide us with a way to get an interacting system Green's function. In the next section, we are going to provide a way of finding these Green's function [44].

The Green's function plays a crucial role in the quasi-particle spectra. It also connects directly to photoemission spectra, because it contains the excitations of an $N \pm 1$ particle system. The spectral function can be obtained from the imaginary part of the Green's function

$$\mathbf{A}(\mathbf{r}_1, \mathbf{r}_2, \omega) = -\frac{1}{\pi} \text{Im} [G(\mathbf{r}_1, \mathbf{r}_2, \omega)]. \quad (3.8)$$

where \mathbf{A} is the spectral function. In the Fig.(3.2) we show a schematic representation of a spectral function. It contains information regarding the spectral strength. The peak position is the quasiparticle energy, which is at the excitation energy $E(\omega) = \varepsilon + \Delta\omega$. This is the quasiparticle energy, which is shifted by $\Delta\omega$ with respect to the non-interacting eigenvalue ε . The quasiparticle lifetime can be obtained by the width of the peak and its spectral weight is determined by the area under the peak [9].

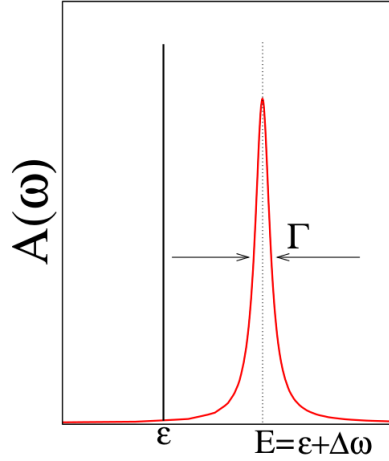


Figure 3.2: Schematic representation of a spectral function [9].

3.3.2 Dyson equation

The Dyson equation is an integral equation, which in principle allows to obtain the interacting particle system Green's function. To this end the self-energy and the non-interacting system Green's function must be known.

The non interacting Green's function

The Hamiltonian of a single particle is

$$H_0(1) = -\frac{1}{2}\nabla_1^2 + V(1), \quad (3.9)$$

By using the field operator from the Heisenberg equation of motion, we can derive the Green's function equation of motion as follows [44]

$$\left[i\frac{\partial}{\partial t_1} - H_0(1) \right] G(1, 2) - \int d3 \Sigma(1, 3)G(3, 2) = \delta(1, 2). \quad (3.10)$$

For a non-interacting particle, we have a similar equation to Eq.(3.10) with $\Sigma = 0$ and V_H is still contained in the Hamiltonian

$$\left[i\frac{\partial}{\partial t_1} - H_0(1) \right] G_0(1, 2) = \delta(1, 2). \quad (3.11)$$

The non-interacting Green's function that satisfies this equation is

$$G_0(\mathbf{r}_1, \mathbf{r}_2, \omega) = 2 \sum_n \sum_{\mathbf{k} \in \text{BZ}} \phi_{n\mathbf{k}}(\mathbf{r}_1) \phi_{n\mathbf{k}}^*(\mathbf{r}_2) \left[\frac{f_{n\mathbf{k}}}{\omega - \epsilon_{n\mathbf{k}} - i\eta} + \frac{1 - f_{n\mathbf{k}}}{\omega - \epsilon_{n\mathbf{k}} + i\eta} \right], \quad (3.12)$$

where $\epsilon_{n\mathbf{k}}$ are the eigenvalues, $\phi_{n\mathbf{k}}(\mathbf{r})$ are the eigenfunctions, $f_{n\mathbf{k}}$ are the occupation factors with values 1 or 0, η is a small complex value to get rid of the divergences in the denominators and the summation is summing over the non-interacting states n . $|n\mathbf{k}\rangle$ label the single particle levels, where n is the index of the band and \mathbf{k} is the grid vector in the BZ. The Dyson equation describes how an interacting Green's function can be determined from Eq.(3.10) and Eq.(3.11)

$$G(1, 2) = G_0(1, 2) + \int d3 d4 G_0(1, 3)\Sigma(3, 4)G(4, 2). \quad (3.13)$$

As we have seen in Eq.(3.13), the Dyson equation is a function of G_0 and Σ only. The only way to evaluate the Dyson equation at this moment is by approximating the self energy Σ . For more details, refer to [44], [9], [48] and [49].

3.4 Self-energy and the GW approximation

The GW approximation is considered the most accurate approximation for the self-energy operator in Eq.(3.13). We will use this approximation to determine the excitation energies [50], determine quasiparticle gaps in solids for many materials and quasiparticle lifetimes [12][52]. The self-energy operator is defined as

$$\Sigma(r, r', t) = \Sigma_x(r, r') + \Sigma_c(r, r', t). \quad (3.14)$$

The first term in the right hand side of Eq.(3.14) represents the exchange self-energy $\Sigma_x(r, r')$ and the second term represents the frequency dependent correlation term. In the next subsections we are going to discuss the details of evaluating Σ and solving Dyson equation.

3.4.1 Hedin's equation

Hedin's equations [11][53] consist of a closed set of coupled integral equations, one of them being the Dyson equation

$$\Sigma(1, 2) = i \int d(34) G(1, 3) \Gamma(3, 2, 4) W(4, 1^+), \quad (3.15)$$

$$G(1, 2) = G_0(1, 2) + \int d(34) G_0(1, 3) \Sigma(3, 4) G(4, 2), \quad (3.16)$$

$$\Gamma(1, 2, 3) = \delta(1, 2) \delta(1, 3) + \int d(4567) \frac{\partial \Sigma(1, 2)}{\partial G(4, 5)} G(3, 4) G(7, 5) \Gamma(6, 7, 3), \quad (3.17)$$

$$\tilde{\chi}(1, 2) = -i \int d(34) G(1, 3) G(4, 1^+) \Gamma(3, 4, 2). \quad (3.18)$$

$$W(1, 2) = v(1, 2) + \int d(34) v(1, 3) \tilde{\chi} W(4, 2), \quad (3.19)$$

Γ represents vertex function, W represents the screened interaction, v represents the bare coulomb interaction and $\tilde{\chi}$ represents the irreducible polarizability. The notation 1^+ for combined coordinates space, spin, and time, the plus subscript $+$ has the definition $1^+ = (\mathbf{r}_1, \sigma_1, t_1 + \delta)$, where $\delta > 0$ is infinitesimal. The irreducible polarizability $\tilde{\chi}$ is the change of electron density n due to the change of the total potential field $V_{total} = V_{ext} + V_H$

$$\tilde{\chi}(1, 2) = \frac{\delta n(1)}{\delta V_{total}(2)} = \frac{\delta n(1)}{\delta (V_{ext}(2) + V_H(2))}, \quad (3.20)$$

The vertex function is the change of the inverse Green's function due to the change in the total potential. This is equal to the change of Σ due to the change of the total potential field

$$\Gamma(1, 2, 3) = -\frac{\delta G^{-1}(1, 2)}{\delta V_{total}(3)} = \delta(1, 2) \delta(1, 3) + \frac{\delta \Sigma(1, 2)}{\delta V_{total}(3)}, \quad (3.21)$$

The screened interaction W is linked to the inverse dielectric function by the means of the bare coulomb interaction v

$$W(1, 2) = \int \epsilon^{-1}(1, 3) v(3, 2) d3, \quad (3.22)$$

and the dielectric function is related to the irreducible polarizability by the relation

$$\epsilon(1, 2) = \delta(1, 2) - \int v(1, 3) \tilde{\chi}(3, 2) d3. \quad (3.23)$$

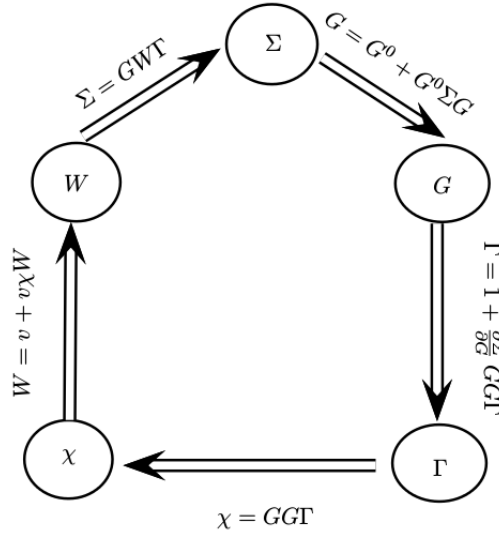


Figure 3.3: Hedin's pentagon of the iterative determination of Σ .

Hedin's equations can be described by an iterative scheme to determine Σ as shown in Fig.(3.3). The starting point for determining Σ is the top of the pentagon in Fig.(3.3). We could set $\Sigma = 0$ as a starting point. This leads to $G = G_0$ and gives the simplest vertex function, which becomes a delta function. The next step is to obtain the independent particle Green's function G_0 . This Green's function can be evaluated using KS wavefunctions. The initial polarizability becomes the independent particle polarizability, which is called the Random Phase Approximation (RPA) polarizability χ^0 . This leads us to evaluate the screened coulomb interaction by the RPA polarizability $W = W_0 = W^{RPA}$. Consequently, $\Sigma = iG_0W_0$. Theoretically, we should reach self-consistence by iterating this process. Since the scheme becomes computationally demanding, we stop the iteration process after one round, so that $\Sigma = iG_0W_0$. This non-iterative solution of Hedin's equations is called the GW approximation (GWA), which is widely used [11]. The GWA approximates the vertex function $\Gamma(1, 2, 3)$ using a delta functions, which simplifies the interaction between the virtual hole and electron excitations [54]

$$\Gamma(1, 2, 3) \approx \delta(1, 2)\delta(1, 3).$$

The equations of GWA are

$$\tilde{\chi}(1, 2) \approx \chi^0(1, 2) = -iG_0(1, 2)G_0(2, 1^+). \quad (3.24)$$

$$W_0(1, 2) = v(1, 2) + \int d3 d4 v(1^+, 3)\chi^0(3, 4)W_0(1^+, 2). \quad (3.25)$$

$$\Sigma(1, 2) = iG_0(1, 2)W_0(1^+, 2). \quad (3.26)$$

Once we have calculated the self-energy, we can determine the quasiparticle energies from equation (3.1). Finally, we can conclude with the following steps to get Σ

- a) Solve the Kohn-Sham equation (DFT ground state calculation) and determine G_0 in the KS basis.
- b) Use Eq.(3.24) to get χ^0 , W_0 and Σ ,
- c) Use Eq.(3.1) to get QP energies.

For further details, see [55].

3.4.2 Random Phase Approximation (RPA)

The Random Phase Approximation (RPA) was proposed by Bohm and Pines in a series of papers [56], [57] and [58]. It approximates the irreducible polarizability $\tilde{\chi}$ by the independent particle polarizability χ^0 , recall Eq.(3.24)

$$\tilde{\chi}(1, 2) \approx \chi^0(1, 2) = -iG_0(1, 2)G_0(2, 1^+),$$

where G_0 is the independent particle propagator. G_0 is evaluated in terms of KS eigenvalues and eigenvectors. χ^0 is defined in the frequency domain and in reciprocal space [11][53] as follows

$$\begin{aligned} \chi_{\mathbf{G}, \mathbf{G}'}^0(\mathbf{q}, \omega) &= 2 \sum_{nn'} \int_{\text{BZ}} \frac{d\mathbf{k}}{(2\pi)^3} \rho_{n' n\mathbf{k}}^*(\mathbf{q}, \mathbf{G}) \rho_{n' n\mathbf{k}}(\mathbf{q}, \mathbf{G}') f_{n\mathbf{k}-\mathbf{q}} (1 - f_{n'\mathbf{k}}) \\ &\times \left[\frac{1}{\omega + \varepsilon_{n\mathbf{k}-\mathbf{q}} - \varepsilon_{n'\mathbf{k}} + i\eta} - \frac{1}{\omega + \varepsilon_{n'\mathbf{k}-\mathbf{q}} - \varepsilon_{n\mathbf{k}} - i\eta} \right], \end{aligned} \quad (3.27)$$

where $\rho_{nn'}(\mathbf{k}, \mathbf{q}, \mathbf{G}) = \langle n\mathbf{k} | e^{i(\mathbf{q}+\mathbf{G})\cdot\mathbf{r}} | n'\mathbf{k} \rangle$ is the oscillators matrix elements. \mathbf{G} is the reciprocal lattice vectors. According to RPA, we can evaluate the inverse microscopic dielectric function, which is defined [11][53] as

$$\epsilon_{\mathbf{G}, \mathbf{G}'}^{-1}(\mathbf{q}, \omega) = \delta_{\mathbf{G}, \mathbf{G}'} + v(\mathbf{q} + \mathbf{G}) \tilde{\chi}_{\mathbf{G}, \mathbf{G}'}(\mathbf{q}, \omega). \quad (3.28)$$

The optical absorption spectrum within RPA is determined by the imaginary part of the macroscopic dielectric function, where the macroscopic dielectric function is related to the inverse of the microscopic dielectric function as follows

$$\epsilon_M^{LF}(\omega) = \lim_{q \rightarrow 0} \frac{1}{\epsilon_{\mathbf{G}=0, \mathbf{G}'=0}^{-1}(\mathbf{q}, \omega)}. \quad (3.29)$$

LF in Eq.(3.29) means that the local field effect is introduced, which is related to the dipole oscillations induced by the external potential. The optical absorption spectrum without local field is given by

$$\epsilon_M^{NLF}(\omega) = \lim_{q \rightarrow 0} \epsilon_{\mathbf{G}=0, \mathbf{G}'=0}(\mathbf{q}, \omega). \quad (3.30)$$

Eq.(3.29) with LF is more accurate than the Eq.(3.30) without LF because it gives the complete physical picture of the system. The difference between these two equations appears in the denominator of Eq.(3.29). It is related to the first element of the inverse of the whole microscopic dielectric matrix. This term cannot be evaluated by simply taking the inverse of the first element of the microscopic dielectric function matrix.

The absorption spectrum within RPA is often in disagreement with experiments. This is because the polarizability of the KS is not the response of the whole interacting system, even if we include the quasiparticle energies and the corrected band gap that is calculated in GWA. The reason for this failure is due to neglecting the proper electron-hole interaction that originally came from replacing the vertex function with a local and instantaneous function. This is an unrealistic and very drastic approximation for the polarizability. This problem is solved by improving the approximation for the vertex function to include the many-body effect in terms of the electron-hole interaction. There are more details, see Sec.(3.5). In chapter 5, we will calculate the optical absorption within RPA for some examples to support our discussion.

3.4.3 Plasmon Pole Approximation (PPA)

From the discussion in Sec.(3.4.1) and also from the Eqs.(3.14, 3.15, 3.22), we can write the exchange self energy term as

$$\Sigma_x(r, r') = iv(r, r')G_0(r, r', t), \quad (3.31)$$

and the second term, which is the frequency dependent self-energy term as

$$\Sigma_c(r, r', t) = iW(r, r', t)G_0(r, r', t) = i \left[\int dr'' v(r, r'') \bar{\epsilon}^{-1}(r, r', t) \right] G_0(r, r', t). \quad (3.32)$$

The screening interaction W can be deduced from Eq.(3.32) to be $W = \epsilon^{-1}v$. This equation links W to v by means of the inverse dielectric function, which is the frequency dependent

$$\epsilon^{-1}(r, r', \omega) = \delta(r - r') + \int dr'' v(r, r'') \chi(r'', r', \omega). \quad (3.33)$$

In the Plasmon Pole Approximation (PPA), we are going to substitute the frequency dependency of the imaginary part of every element of the inverse dielectric function (which is a frequency dependent matrix) with a narrow Lorentzian peak [9]. To this end, let us rewrite the exchange and correlation terms of the self-energy in reciprocal space. The exchange term is defined as

$$\Sigma^x(\mathbf{r}_1, \mathbf{r}_2) = -\frac{1}{|\mathbf{r}_1 - \mathbf{r}_2|} \sum_n \sum_{\mathbf{k} \in \text{BZ}} \phi_{n\mathbf{k}}(\mathbf{r}_1) \phi_{n\mathbf{k}}^*(\mathbf{r}_2) f_{n\mathbf{k}}. \quad (3.34)$$

As we see in this equation, the exchange term of the self-energy is described by the Fock term of the Hartree-Fock self-energy. The analytical expression for the matrix element of the exchange self energy $\langle n\mathbf{k} | \Sigma^x(\mathbf{r}_1, \mathbf{r}_2) | n\mathbf{k} \rangle$, follows from

$$\Sigma_{n\mathbf{k}}^x = - \sum_{n'} \int_{\text{BZ}} \frac{d\mathbf{q}}{(2\pi)^3} \sum_G v(q+G) |\rho_{nn'}(\mathbf{k}, \mathbf{q}, \mathbf{G})|^2 f_{n'}(\mathbf{k} - \mathbf{q}), \quad (3.35)$$

where $v(\mathbf{q} + \mathbf{G}) \equiv 4\pi/|\mathbf{q} + \mathbf{G}|^2$. The frequency dependent self-energy term is also called the correlation term. The analytical expression of its matrix element $\langle n\mathbf{k} | \Sigma^c(\mathbf{r}_1, \mathbf{r}_2, \omega) | n\mathbf{k} \rangle$, is the following

$$\begin{aligned} \Sigma^c(n\mathbf{k}) &= i \sum_{n'} \int_{\text{BZ}} \frac{dq}{(2\pi)^3} \sum_{\mathbf{G}, \mathbf{G}'} \frac{4\pi}{|\mathbf{q} + \mathbf{G}|^2} \rho_{n, n'}(\mathbf{k}, \mathbf{q}, \mathbf{G}) \rho_{n, n'}^*(\mathbf{k}, \mathbf{q}, \mathbf{G}') \\ &\times \int d\omega' G_{n', \mathbf{k}-\mathbf{q}}^0(\omega - \omega') \epsilon_{\mathbf{G}, \mathbf{G}'}^{-1}(\mathbf{q}, \omega'). \end{aligned} \quad (3.36)$$

If $\epsilon_{\mathbf{G}, \mathbf{G}'}^{-1}(\mathbf{q}, \omega')$ is known, the Eq.(3.36) can be solved. PPA solves this equation by achieving an integration over the frequency in Eq.(3.36). It considers all weights of a single excitation at the Plasmon pole frequency [61]

$$\epsilon_{G, G'}^{-1}(q, w) \approx \delta_{\mathbf{G}, \mathbf{G}'} + \left[\frac{R_{G, G'}(q)}{\omega - \tilde{\omega}_{G, G'}(q) + i\eta} - \frac{R_{G, G'}(q)}{\omega + \tilde{\omega}_{G, G'}(q) - i\eta} \right], \quad (3.37)$$

where $\tilde{\omega} = E_{\text{PPA}} \sqrt{\frac{\epsilon_2^{-1}}{\epsilon_1^{-1} - \epsilon_2^{-1}}}$ is the energy and $R = -\frac{\epsilon_1^{-1} \tilde{\omega}}{2}$ is the residual. These parameters determine the dielectric matrix by imposing the PPA model at $w = 0$ and at $w = \frac{iE_{\text{PPA}}}{\hbar}$, which is the plasmon pole frequency [54]

$$\epsilon_1^{-1} = \tilde{\epsilon}^{-1}(0 + i0) = -\frac{2R}{\tilde{\omega}},$$

$$\epsilon_2^{-1} = \tilde{\epsilon}^{-1} \left(\frac{iE_{\text{PPA}}}{\hbar} \right) = - \frac{2R\tilde{\omega}}{\frac{E_0^2}{\hbar^2} + \tilde{\omega}^2},$$

where E_{PPA} is the PPA imaginary energy and considered to be a user-defined parameter in the corresponding program packages.

3.4.4 Solving Dyson's equation

Dyson's equation can be written in the basis of the particle levels $|n\mathbf{k}\rangle$ as

$$G_{n\mathbf{k}}(\omega) = \left[(G_{n\mathbf{k}}^0)^{-1} - \Sigma_{n\mathbf{k}}(\omega) + V_{n\mathbf{k}}^{xc} \right]^{-1}, \quad (3.38)$$

where G_0 is defined in Eq.(3.12) and takes the basis form of the non-interacting reference system of the KS theory. For semiconductors the occupation factor $f_{n\mathbf{k}}$ is either 1 or 0. By substituting this value into Eq.(3.12), Eq.(3.38) becomes

$$G_{n\mathbf{k}}(\omega) = \frac{1}{\omega - \epsilon_{n\mathbf{k}} - [\Sigma_{n\mathbf{k}}^x + \Sigma_{n\mathbf{k}}^c(\omega) - V_{n\mathbf{k}}^{xc}]}. \quad (3.39)$$

To solve this equation, we are going to use the Newton approximation. In this approximation, the first order of the Taylor expansion of Σ around $\epsilon_{n\mathbf{k}}$ is taken. This leads to

$$\epsilon_{n\mathbf{k}}^{Qp} = \epsilon_{n\mathbf{k}} - \frac{G_{n\mathbf{k}}(\epsilon_{n\mathbf{k}})}{\partial G_{n\mathbf{k}} / \partial \omega(\epsilon_{n\mathbf{k}})}, \quad (3.40)$$

By substituting Eq.(3.40) into Eq.(3.39), we get

$$\epsilon_{n\mathbf{k}}^{Qp} = \epsilon_{n\mathbf{k}} + Z_{n\mathbf{k}} [\Sigma_{n\mathbf{k}}^x + \Sigma_{n\mathbf{k}}^c(\epsilon_{n\mathbf{k}}) - V_{n\mathbf{k}}^{xc}], \quad (3.41)$$

where Z is a re-normalization factor, defined by

$$Z_{n\mathbf{k}} \equiv \left[1 - \frac{\partial \Sigma_{n\mathbf{k}}^c(\omega)}{\partial \omega} \Big|_{\omega=\epsilon_{n\mathbf{k}}} \right]^{-1}. \quad (3.42)$$

According to equations Eq.(3.41) and Eq.(3.42), the quasiparticle energy looks quite easy to determine [61]. In particular the derivative in Eq.(3.42) can be evaluate using a finite difference method [61][62][64].

The success of GWA is limited to the description of energy levels, energy gaps and photoemission spectra. However, it does not yield proper absorption spectra and a reflectivity that are in good agreement with the experiments [54][9]. This is because the electronic correlation response function is not described in an adequate way. It does not include all possible interactions between all electrons and holes, which are represented by $G(1,2)$ for the electron and $G(2,1^+)$ for the hole. Many drawbacks of the GWA are resolved by involving two particle excitations. In other words we should take into account the two particle Green's function, which is the topic of the Bethe Salpeter equation [60]. To include the e-h pairs interactions in the calculations, it is important to relate the linear response function with the two particle Green's function for the electron and hole, which is discussed in detail in the next section.

3.5 The Bethe-Salpeter equation (BSE)

The BSE is introduced by using a two particle Green's function for electron-hole states [11][53]. It is defined as a four point function, which has the symbol \tilde{L} . The Green's function of non-interacting e-h pairs L^0 is related to the non-interacting response function in the limit $\mathbf{q} \rightarrow 0$

as follows

$$\lim_{\mathbf{q} \rightarrow 0} \chi_{\mathbf{G}, \mathbf{G}'}^0(\mathbf{q}, \omega) = -i \sum_{nn'\mathbf{k}} \lim_{\mathbf{q} \rightarrow 0} \left[\rho_{nn'\mathbf{k}}^*(\mathbf{q}, \mathbf{G}) \rho_{nn'\mathbf{k}}(\mathbf{q}, \mathbf{G}') \right] L_{nn'\mathbf{k}}^0(\omega). \quad (3.43)$$

The new interacting polarizability, which is used in BSE includes the vertex corrections. These corrections are obtained through a second iteration of Hedin's equations, see Sec.(3.4.1). For more further details, refer to [11], [53] and [70]. Then the \tilde{L} can be defined by the new interaction polarizability [54]

$$\lim_{\mathbf{q} \rightarrow 0} \tilde{\chi}_{\mathbf{G}, \mathbf{G}'}(\mathbf{q}, \omega) = -i \sum_{nn'\mathbf{k}} \sum_{mm'\mathbf{k}'} \lim_{\mathbf{q} \rightarrow 0} \left[\rho_{nn'\mathbf{k}}^*(\mathbf{q}, \mathbf{G}) \rho_{mm'\mathbf{k}'}(\mathbf{q}, \mathbf{G}') \right] \tilde{L}_{nn'\mathbf{k}}(\omega). \quad (3.44)$$

\tilde{L} can be related to the non-interacting Green's function for the electron and hole (e-h) L^0 , which leads to the BSE

$$\tilde{L}_{nn'\mathbf{k}, mm'\mathbf{k}'}(\omega) = L_{nn'\mathbf{k}}^0(\omega) \left[\delta_{nm} \delta_{n'm'} \delta_{\mathbf{k}\mathbf{k}'} + i \sum_{ll'\mathbf{k}''} \Xi_{nn'\mathbf{k}, ll'\mathbf{k}''} \tilde{L}_{ll'\mathbf{k}'', mm'\mathbf{k}'}(\omega) \right], \quad (3.45)$$

where $\Xi_{nn'\mathbf{k}, ll'\mathbf{k}''}$ is the kernel of the BSE. It is defined as

$$\Xi_{nn'\mathbf{k}, ll'\mathbf{k}''} = W_{nn'\mathbf{k}, ll'\mathbf{k}''} - 2\tilde{V}_{ll'\mathbf{k}'', ll'\mathbf{k}''}, \quad (3.46)$$

where W is the screened coulomb interaction between electron-hole pairs and \tilde{V} is the unscreened short range exchange interaction. The bar symbol refers to the exchange interaction without its long range Fourier component at $G = 0$. They are defined by the Bloch functions as

$$W_{nn'\mathbf{k}, ll'\mathbf{k}_1} = \frac{1}{\Omega N_q} \sum_{\mathbf{G}, \mathbf{G}'} \rho_{nl}(\mathbf{k}, \mathbf{q}, \mathbf{G}) \rho_{n'l'}^*(\mathbf{k}_1, \mathbf{q}, \mathbf{G}') \epsilon_{\mathbf{G}, \mathbf{G}'}^{-1}(\mathbf{q}, \omega) v(\mathbf{q}, \mathbf{G}'), \quad (3.47)$$

$$\tilde{V}_{nn'\mathbf{k}, ll'\mathbf{k}_1} = \frac{1}{\Omega N_q} \sum_{\mathbf{G} \neq 0} \rho_{nn'}(\mathbf{k}, \mathbf{q} = 0, \mathbf{G}) \rho_{l'l'}^*(\mathbf{k}_1, \mathbf{q} = 0, \mathbf{G}). \quad (3.48)$$

where N_q represents the number of points in the BZ. The exchange term includes the LF effects and the screened coulomb interaction is related to the creation of the excitons. BSE in Eq.(3.45) is described in a diagrammatic representation by Fig.(3.4), which shows the interaction between an electron and a hole in an elegant way.

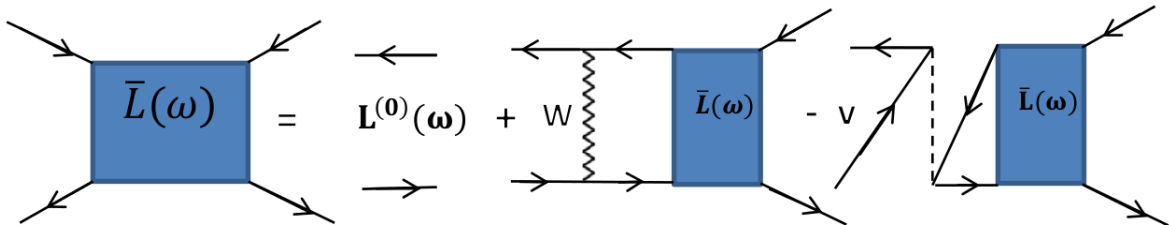


Figure 3.4: The BSE diagrammatic representation. The dashed lines represent the bare coulomb interaction, the wiggled line represents the screened interaction and the straight lines represent the propagation of the KS electron [6].

3.6 Solving the Bethe-Salpeter equation

In this section, we will discuss the derivation of the macroscopic dielectric function, which includes the excitonic effects. In other words we will discuss solving the BSE. There are two methods for solving the BSE. The first one is the Haydock recursive method and the second one is the diagonalization method. In this work, we are concerned with the diagonalization method for reasons that will be mentioned later on. For the former method, we invite the readers to study [9], [54], [59], [28], [65], [66], [67] and [68]. To solve BSE by using the diagonalization method, we should start with the macroscopic dielectric function, which directly relates to the inverse of the microscopic dielectric function according to [59] and [28],

$$\epsilon_M(q, w) = \frac{1}{\epsilon_{G, G'}^{-1}(q, w)} \Big|_{G=0, G'=0}. \quad (3.49)$$

The imaginary part of this equation compares well with the optical absorption spectrum based on the experimental data. To derive the macroscopic dielectric function using the diagonalization method, we need to re-write $\epsilon_M(q, w)$ [9][54]

$$\epsilon_M(w) = 1 - \lim_{q \rightarrow 0} \left[v_{G=0}(q) \int dr_1 dr_2 e^{-iq(r_1-r_2)} L(r_1, r_2, r_3, r_4, w) \right]. \quad (3.50)$$

We will carry on by using the standard approach of expressing the four point e-h Green's function L in the transition space, which are the products of single particle states. This is required to expand $L(r_1, r_2, r_3, r_4, w)$ into DFT Bloch states as follows

$$L(n_1, n_2)(n_3, n_4)(w) = \langle \phi_{n_1}^*(r_1) \phi_{n_2}(r_2) | L(r_1, r_2, r_3, r_4, w) | \phi_{n_3}^*(r_3) \phi_{n_4}(r_4) \rangle = \langle \langle L \rangle \rangle, \quad (3.51)$$

where n_1, n_2, n_3 and n_4 correspond to v, c, v' and c' respectively. Then the BSE equation Eq.(3.45) can be formally written as

$$L = [L^0 + L^0 \Xi L]. \quad (3.52)$$

It is easier to deal with the inverse BSE

$$L = [1 - L^0 \Xi]^{-1} L^0, \quad (3.53)$$

$$L = [(L^0)^{-1} - \Xi]^{-1}.$$

For the systems with the energy gaps, we can rewrite L in terms of the two particle Hamiltonian, which is the so-called excitonic Hamiltonian as follows

$$L_{(n_1, n_2), (n_3, n_4), (w)} = [H^{exc} - I\omega]_{(n_1, n_2), (n_3, n_4)}^{-1} (f_{n_4} - f_{n_3}), \quad (3.54)$$

where $I = \delta_{(n_1, n_2)} \cdot \delta_{(n_3, n_4)}$ and the complete form of the excitonic Hamiltonian is

$$H_{n_1 n_2 \mathbf{k}, n_3 n_4 \mathbf{k}'}^{exc} = (\varepsilon_{n_1 \mathbf{k}} - \varepsilon_{n_2 \mathbf{k}'}) \delta_{(n_1 n_3)} \cdot \delta_{(n_2 n_4)} \cdot \delta_{(k k')} + (f_{n_2 \mathbf{k}} - f_{n_1 \mathbf{k}}) \left[2\tilde{V}_{n_1 n_2 \mathbf{k}, n_3 n_4 \mathbf{k}'} - W_{n_1 n_2 \mathbf{k}, n_3 n_4 \mathbf{k}'} \right]. \quad (3.55)$$

For a complete derivation, see [43]. The excitonic Hamiltonian in the latter equation is a two particle Hamiltonian, which includes two parts : the first part represents the energy difference between the hole state and the electron state. The second part describes the interaction between

e-h. The equation for the effective two particle of the excitonic system is written in an energy independent form as

$$\sum_{n_3 n_4} (\varepsilon_{n_1 \mathbf{k}} - \varepsilon_{n_2 \mathbf{k}'}) \delta_{(n_1 n_3)} \cdot \delta_{(n_2 n_4)} \cdot \delta_{(k k')} + (f_{n_2 \mathbf{k}} - f_{n_1 \mathbf{k}}) \left[2\tilde{V}_{n_1 n_2 \mathbf{k}, n_3 n_4 \mathbf{k}'} - W_{n_1 n_2 \mathbf{k}, n_3 n_4 \mathbf{k}'} \right] A_\lambda^{(n_3 n_4)} = E_\lambda A_\lambda^{(n_1 n_2)}. \quad (3.56)$$

To solve Eq.(A.4), we need to write the excitonic Hamiltonian in a matrix form [9], which is given as

$$H_{(vc),(v'c')}^{exc} = \begin{pmatrix} H_{(vc),(v'c')}^{exc,res} & H_{(vc),(c'v')}^{coupling} \\ -[H_{(vc),(c'v')}^{coupling}]^* & -[H_{(vc),(v'c')}^{exc,res}]^* \end{pmatrix}. \quad (3.57)$$

It is important to note that, for non-metallic resonant optical transitions $(n_1, n_2) = (vck) \Rightarrow (vc)$ and $(n_3, n_4) = (v'c')$. The first block in the total matrix expression, $H_{(vc),(v'c')}^{exc,res}$ is called the resonant term, which is Hermitian. It contains positive frequency transitions. The fourth term is called the anti-resonant term. It contains negative frequency transitions. The off-diagonal terms are called coupling terms.

The resonant term is composed of three parts [9]. They are evaluated in momentum space as follows:

$$H_{(vc),(v'c')}^{exc,res} = H_{(vc),(v'c')}^{diag,res} + H_{(vc),(v'c')}^{exch,res} + H_{(vc),(v'c')}^{scr,res}. \quad (3.58)$$

- The diagonal part, $H^{diag,res}$, contains the difference between electron and hole energies. These energies could be also quasiparticle energies, which are calculated in the GW approximation

$$H_{(vck),(v'c'k')}^{diag,res} = (E_{ck} - E_{vk}) \delta_{vv'} \delta_{cc'} \delta_{kk'}. \quad (3.59)$$

- The second part is the unscreened short-range electron-hole exchange term, $H^{exch,res}$,

$$H_{(vck),(v'c'k')}^{exch,res} = 2 \frac{4\pi}{\Omega} \sum_{G \neq 0} \frac{1}{|G^2|} \langle cK | e^{iG \cdot r} | vK \rangle \langle v'K' | e^{-iG \cdot r} | c'K' \rangle. \quad (3.60)$$

- The third part is the screened coulomb term, $H^{scr,res}$, for electron-hole interaction

$$H_{(vck),(v'c'k')}^{scr,res} = -2 \frac{4\pi}{\Omega} \sum_{GG'} \frac{\tilde{\epsilon}_{GG'}^{-1}(q)}{|G+q||G'+q|} \langle cK | e^{i(G+q) \cdot r} | c'K' \rangle \times \langle v'K' | e^{-i(G'+q) \cdot r'} | vK \rangle \cdot \delta_{q, K-K'}, \quad (3.61)$$

where Ω is the volume of the crystal and $\tilde{\epsilon}_{GG'}^{-1}(q) = \epsilon_{GG'}^{-1}(q) \frac{|q+G'|}{|q+G|}$ is the symmetrized inverse dielectric function.

The coupling part of the excitonic Hamiltonian is composed of two parts [9]

$$H_{(vc),(c'v')}^{coupling} = H_{(vc),(c'v')}^{exch,coup} + H_{(vc),(c'v')}^{scr,coup}. \quad (3.62)$$

- The first part is an unscreened short-range exchange term, $H^{exch,coup}$,

$$H_{(vck),(c'v'k')}^{exch,coup} = 2 \frac{4\pi}{\Omega} \sum_{G \neq 0} \frac{1}{|G^2|} \langle cK | e^{iG \cdot r} | vK \rangle \langle c'K' | e^{-iG \cdot r} | v'K' \rangle. \quad (3.63)$$

- The second part is a screened coulomb term , $H^{scr,coup}$,

$$H_{(vck),(c'v'k')}^{scr,coup} = -2\frac{4\pi}{\Omega} \sum_{GG'} \frac{\tilde{\epsilon}_{GG'}^{-1}(q)}{|G+q||G'+q|} \langle cK | e^{i(G+q)\cdot r} | v'K' \rangle \quad (3.64)$$

$$\times \langle c'K' | e^{-i(G'+q)\cdot r'} | vK \rangle \cdot \delta_{q,K-K'}.$$

Once we diagonalize the excitonic Hamiltonian, we get exciton energies as eigenvalues and exciton wavefunctions as eigenvectors.

The next step is evaluating the macroscopic dielectric function. A useful spectral representation to determine L [9] in Eq.(3.54) is

$$[H^{exc} - I\omega]^{-1} = \sum_{\lambda,\lambda'} = \frac{|A_\lambda\rangle S_{\lambda,\lambda'}^{-1} \langle A_{\lambda'}|}{\omega - E_\lambda}, \quad (3.65)$$

where $S_{\lambda,\lambda'} = \langle A_\lambda | A_{\lambda'} \rangle$ is the overlap matrix of the excitonic Hamiltonian. Using the eigenvalues $\{E_\lambda\}$ and eigenvectors $\{A_\lambda\}$ of the excitonic Hamiltonian, we may write the polarizability function in transition space as

$$L_{(n_1,n_2),(n_3,n_4)}(\omega) = \sum_{\lambda,\lambda'} \frac{A_\lambda^{(n_1,n_2)} S_{\lambda,\lambda'}^{-1} A_{\lambda'}^{*(n_3,n_4)}}{\omega - E_\lambda} (f_{n_4} - f_{n_3}). \quad (3.66)$$

Now the macroscopic dielectric function can be evaluated by placing this L into equation (3.50), which defines the macroscopic dielectric function with the optical limit of $\mathbf{G} = \mathbf{G}' = 0$, a long an particular \mathbf{q} direction. The final form of the macroscopic dielectric function becomes

$$\epsilon_M(\omega) = 1 - \lim_{q \rightarrow 0} \left[v_{G=0}(q) \sum_{\lambda\lambda'} \left[\sum_{n_1,n_2} \langle n_1 | e^{-iq\cdot r_1} | n_2 \rangle \frac{A_\lambda^{n_1 n_2} S_{\lambda\lambda'}^{-1}}{\omega - E_\lambda + i\eta} \sum_{n_3,n_4} \langle n_4 | e^{iq\cdot r_2} | n_3 \rangle A^{*(n_3 n_4)} (f_{n_4} - f_{n_3}) \right] \right], \quad (3.67)$$

where the matrix element $\langle n_1 | e^{-iq\cdot r_1} | n_2 \rangle$ is the dipole operator matrix element in transition space. The imaginary constant in the last expression $i\eta$ is added to the frequency ω , which shifts the poles away from the real axis. It is a common practice in solid-state calculations to ignore the coupling term in the excitonic Hamiltonian. This is the so-called Tamm-Dancoff Approximation (TDA). The excitonic Hamiltonian in Eq.(3.57) becomes now

$$H_{(vc),(v'c')}^{exc} = \begin{pmatrix} H_{(vc),(v'c')}^{exc,res} & 0 \\ 0 & - [H_{(vc),(v'c')}^{exc,res}]^* \end{pmatrix}. \quad (3.68)$$

and the macroscopic dielectric function [9] becomes

$$\epsilon_M(\omega) = 1 - \lim_{q \rightarrow 0} v_{G=0}(q) \sum_{\lambda} \frac{|\sum_{n_1 n_2} \langle n_1 | e^{-iq\cdot r} | n_2 \rangle A_\lambda^{(n_1 n_2)}|^2}{\omega - E_\lambda + i\eta}. \quad (3.69)$$

The imaginary part of $\epsilon_M(\omega)$, which relates to the absorption spectrum is

$$\epsilon_2(\omega) = 2 \lim_{q \rightarrow 0} v_{G=0}(q) \sum_{\lambda} \text{Im} \frac{|\sum_{n_1 n_2} \langle n_1 | e^{-iq\cdot r} | n_2 \rangle A_\lambda^{(n_1 n_2)}|^2}{\omega - E_\lambda + i\eta}. \quad (3.70)$$

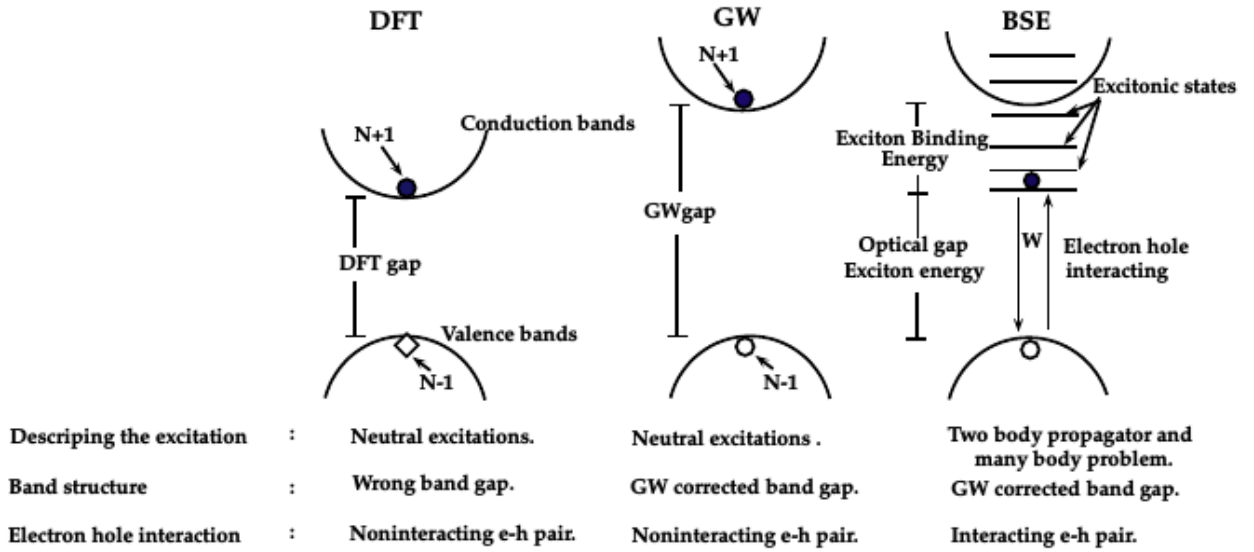


Figure 3.5: Schematic representation of the different levels of theories for the optical spectral description.

We conclude this discussion by showing a brief description of the optical spectra for different level of theory discussed in this chapter. This is shown in Fig.(3.5)

We close with a flow chart in Fig.(3.6) that shows a typical numerical implementation of the BSE.

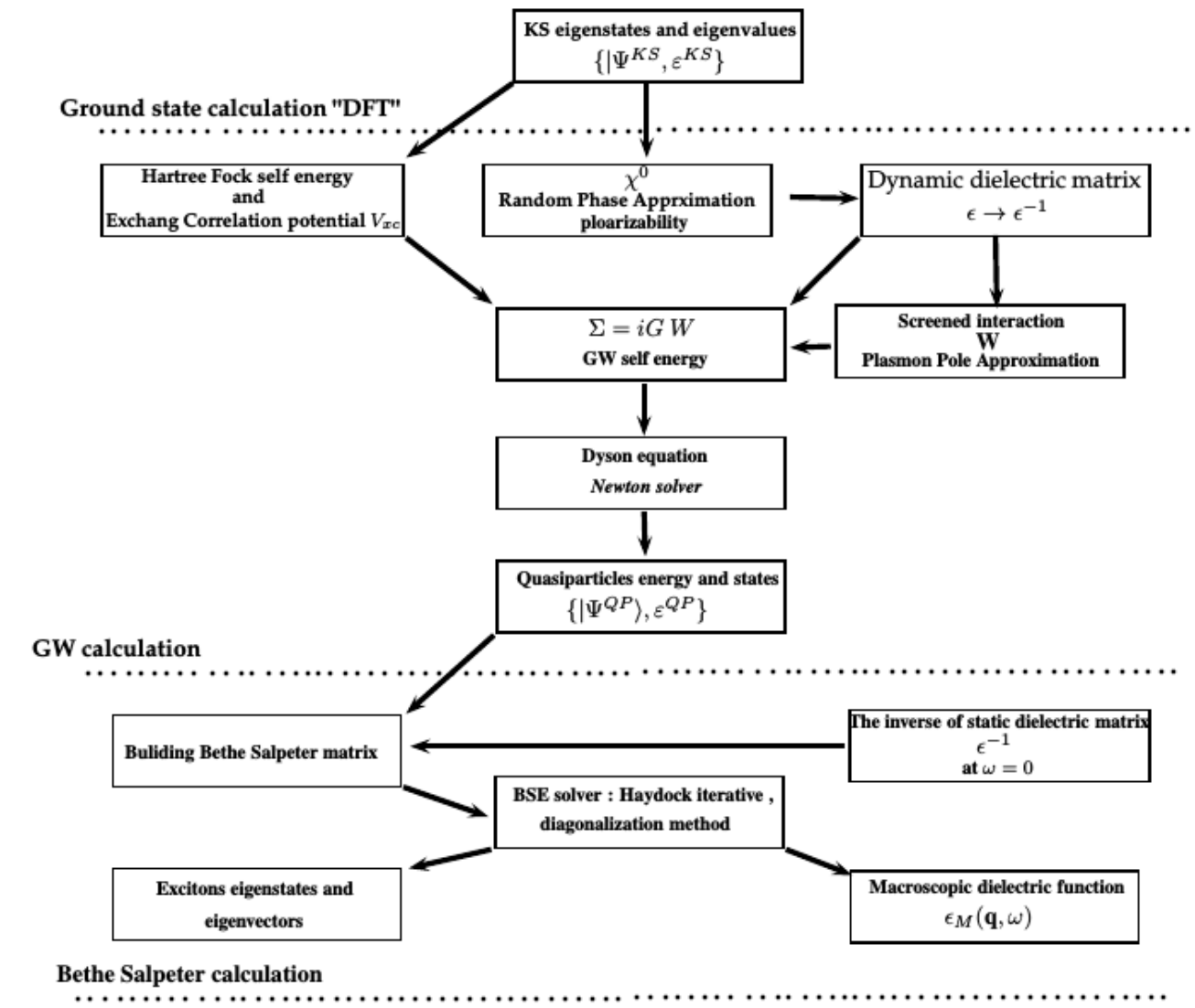


Figure 3.6: Schematic representation of the solution of Bethe Salpeter equation practically.

Chapter 4

Exciton models and lifetimes.

4.1 Excitons

Excitons are bound electron-hole pairs. The literature describes two major types of excitons :

- A tight bound exciton, also called the Frenkel exciton. The Frenkel exciton's radius is comparable to the interatomic spacing and according to that, they are localized states because they are tightly bound to specific molecules or atoms. The probability of finding the exciton on the same atom in the crystal is very high. Frenkel excitons are observed in materials which have large band gaps, large electron and hole effective masses and small dielectric constants. They have a large binding energy with values ranging from 0.1 eV to several eV and this is interpreted as the Frenkel excitons being stable at room temperature. Frenkel excitons are found in many inorganic crystal materials like alkali halide crystals but also in organic materials like aromatic molecules [29][72].
- A weaker or free exciton, also called Wannier-Mott excitons. Wannier excitons have a large radius. They are not tightly bound to specific atoms, and free to move through the crystal. Wannier excitons are found in semiconductors, which are characterised by small band gaps and high dielectric constants [29][72]. In this thesis, we are dealing with semiconductors, so we are concerned with Wannier-Mott excitons.

4.1.1 The Wannier exciton

We can model the Wannier exciton as a hydrogenic system by applying the Bohr model [29][72]. The effective Hamiltonian of a bound electron-hole pair in a direct gap semiconductor is

$$H_{exc} = E_g - \frac{\hbar^2}{2m_c} \nabla_e^2 - \frac{\hbar^2}{2m_v} \nabla_h^2 - \frac{e^2}{4\pi\epsilon_r(0)|\mathbf{r}_e - \mathbf{r}_h|}. \quad (4.1)$$

where m_v represents the effective mass of the hole, m_c represents the effective mass of the electron and \mathbf{r}_e and \mathbf{r}_h represent the position vectors for the electron and hole respectively. E_g represents the band gap of the semiconductor. The exciton is moving through a medium with dielectric constant $\epsilon_r(0)$. We can follow atomic physics and set up a Hamiltonian for the relative motion of electrons and holes with [73]

$$R = \frac{m_e \mathbf{r}_e + m_h \mathbf{r}_h}{m_e + m_h}, \quad \mu = \frac{m_e m_h}{m_e + m_h}, \quad \mathbf{r} = \mathbf{r}_e - \mathbf{r}_h, \quad (4.2)$$

and get

$$H_{exc} = E_g - \frac{\hbar^2}{2\mu} \nabla_{\mathbf{r}}^2 - \frac{\hbar^2}{2(m_e + m_h)} \nabla_R^2 - \frac{e^2}{4\pi\epsilon_{r0} \mathbf{r}}. \quad (4.3)$$

The wave function for the relative motion of an electron and a hole is described [29] as

$$\psi(\mathbf{r}_e, \mathbf{r}_h) = e^{-\mathbf{k}\cdot\mathbf{R}}\phi_n(\mathbf{r}). \quad (4.4)$$

where \mathbf{k} represents the photon wave vector. In other words, it is the wave vector, at which the electron-hole pair is propagating through the crystal, and $\phi_n(\mathbf{r})$ is a wavefunction that describes the relative motion of the electron and hole as a function of \mathbf{r} . This leads to a hydrogen like Schödinger equation

$$\left(-\frac{\hbar^2}{2\mu}\nabla_{\mathbf{r}}^2 - \frac{e^2}{4\pi\epsilon_{r0}\mathbf{r}}\right)\phi_n(\mathbf{r}) = E_n\phi_n(\mathbf{r}). \quad (4.5)$$

The total wavefunction of the exciton (in direct analogy to the treatment of impurity states in chapter (14) in Ref.[73] is

$$\psi_{\mathbf{k}\mathbf{r}}(\mathbf{R}, \mathbf{r}) = e^{\mathbf{k}\cdot\mathbf{r}}\phi_n(\mathbf{r})\phi_c(\mathbf{r}_e)\phi_v(\mathbf{r}_h), \quad (4.6)$$

where $\phi_c(\mathbf{r}_e)$ and $\phi_v(\mathbf{r}_h)$ represent the Bloch function for an electron in the conduction band and for a hole in the valence band at $\mathbf{k} = 0$ respectively. n is the principal quantum number, which characterises the hydrogen like exciton states [73].

The eigenvalues of the Hamiltonian in Eq.(4.3) are

$$E_{\mathbf{k}n} = E_B(n) + \frac{\mathbf{k}^2}{2(m_e + m_h)}, \quad (4.7)$$

and are measured from the conduction band edge. $E_B(n)$ are the eigenvalues of a bounded hydrogenic Hamiltonian in Eq.(4.5), which is given by

$$E_B(n) = -\frac{E_B}{n^2}. \quad (4.8)$$

where :

$$E_B = \frac{\mu}{m_0\epsilon_r(0)^2}E_{Ry}. \quad (4.9)$$

Here $E_{Ry} = \frac{m_0e^4}{2\hbar^2}$ is a known energy scale of the hydrogen atom (Rydberg energy) [72][29]. In analogy to hydrogen radius, exciton radius is

$$r_{exc} = \frac{m_0}{\mu}\epsilon_r(0)n^2r_{Ry}. \quad (4.10)$$

where r_{Ry} is the Bohr radius of a hydrogen atom. If we look at the two equations (4.9) and (4.10), we find that the exciton with $n = 1$ has the smallest radius and the largest binding energy compared to other excitons with $n > 1$ [72][29].

4.2 Optical transition

4.2.1 Fermi's golden rule

Fermi's golden rule is a simple formula for calculating quantum mechanical transition rates at which electronic or atomic transitions occur between initial and final quantum states. It was first derived by Dirac [76], not Fermi. It was given this name because Fermi considered the rule a golden one, in view of its instrumental role in his theory of Beta decay [74][77] [78]. It applies to optical and electronic processes for which the initial and final states can be described by wave functions. The rate of transition is defined by the probability of transition per unit time, which

can be determined by the transition matrix element in quantum mechanics, using the first order perturbation theory. In almost every textbook on quantum mechanics. Fermi's golden rule is discussed as an application of the lowest order time-dependent perturbation theory. It is given by

$$\gamma_i^f = \frac{2\pi}{\hbar} |\langle i|H'|f\rangle|^2 \delta(E_f - E_i - \hbar\omega), \quad (4.11)$$

where $|i\rangle$ represents the initial state, and $|f\rangle$ represents the final state. This transition is driven by a perturbation \mathbf{H}' . The way of deriving Eq.(4.11) is to start with time dependent perturbation theory and to take the limit for absorption under the assumption that the time of the measurement is much larger than the time needed for the transition. This derivation of Eq.(4.11) can be found in most textbooks [79][80][81][82][83][84][85][86][87]. Fermi's golden rule is also called the decay probability, which is related to the inverse of the lifetime.

A typical scenario would be a photon absorption causing a transition of an electron between a valence band and a conduction band. Let us start with the Hamiltonian that describes how an electron interacts with an electromagnetic field. The electromagnetic field is represented by ϕ and \mathbf{A} , which are scalar potential and a vector potential respectively. Their relation to electric field \mathbf{E} and magnetic field \mathbf{B} is given by

$$\mathbf{E} = -\nabla\phi - \frac{1}{c} \frac{\partial \mathbf{A}}{\partial t}, \quad \mathbf{B} = \nabla \times \mathbf{A}.$$

The quantum dynamics of a particle with mass m and charge e in an electromagnetic field can be described by the following Hamiltonian [90] [92]

$$H = \frac{1}{2m_c} \left(\mathbf{p} - \frac{e}{c} \mathbf{A} \right)^2 + e(\phi + V(r)), \quad (4.12)$$

where $V(r)$ represents the periodic potential in the absence of an electromagnetic field. Let us re-write this as

$$H = \frac{1}{2m} p^2 + \frac{e}{2m} \left(-(\mathbf{A} \cdot \mathbf{p} + \mathbf{p} \cdot \mathbf{A}) + \frac{e}{c} A^2 \right) + e(\phi + V(r)).$$

Now, $\mathbf{A} \cdot \mathbf{p} = \mathbf{p} \cdot \mathbf{A}$ and the usual gauge for \mathbf{A} , which satisfies the Coulomb gauge [90], is $\nabla \cdot \mathbf{A} = 0$. Suppose that the electromagnetic potential that is considered is a plane wave [92]. In this case we have

$$\mathbf{A} = \mathbf{A}_0 \hat{\mathbf{e}} (\exp [i(\mathbf{k} \cdot \mathbf{r} - \omega t)] + \exp [-i(\mathbf{k} \cdot \mathbf{r} - \omega t)]), \quad (4.13)$$

and $\phi = 0$, where $\hat{\mathbf{e}}$ represents the unit vector in the direction of polarization of an electromagnetic plane wave and \mathbf{k} is the wave vector. The Hamiltonian operator of a particle, which interacts with an electromagnetic field can be written as

$$H = H_0 + H', \quad H_0 = \frac{p^2}{2m} + eV,$$

with the perturbation

$$H' = -\frac{e}{mc} \mathbf{A} \cdot \mathbf{p}. \quad (4.14)$$

The quadratic term in \mathbf{A} has been neglected, because it is very small compared to the linear term in \mathbf{A} . By substituting Eq.(4.14) and Eq.(4.13) into Fermi's golden rule Eq.(4.11), we get the transition rate for an absorption process

$$\gamma_i^f = \frac{2\pi}{\hbar} \frac{e^2}{m^2 c^2} A_0^2 \sum_{\mathbf{k}} |\langle v\mathbf{k} | e^{i(\mathbf{k} \cdot \mathbf{r})} \hat{\mathbf{e}} \cdot \mathbf{p} | c\mathbf{k} \rangle|^2 \delta(E_f - E_i - \hbar\omega), \quad (4.15)$$

and for an emission process

$$\gamma_i^f = \frac{2\pi}{\hbar} \frac{e^2}{m^2 c^2} A_0^2 \sum_{\mathbf{k}} |\langle v\mathbf{k} | e^{(-i\mathbf{k}\cdot\mathbf{r})} \hat{\mathbf{e}} \cdot \mathbf{p} | c\mathbf{k} \rangle|^2 \delta(E_f - E_i - \hbar\omega). \quad (4.16)$$

where the energy E_i is the eigenvalue of the eigenstate $|v\mathbf{k}\rangle$ and the energy E_f is the eigenvalue of the eigenstate $|c\mathbf{k}\rangle$. For more details, see [90].

4.2.2 Electric dipole approximation

For the transition between two different states, the electromagnetic radiation wavelength is often much larger than the size of the atom or molecule. If we then expand the term $e^{-i\mathbf{k}\cdot\mathbf{r}}$ into a Taylor series [92]

$$e^{-i\mathbf{k}\cdot\mathbf{r}} \approx 1 - i\mathbf{k} \cdot \mathbf{r} + \dots,$$

we may as well approximate this sum by its first term only

$$e^{-i\mathbf{k}\cdot\mathbf{r}} \approx 1. \quad (4.17)$$

This approach is called the electric dipole approximation. Under this assumption the optical dipole transition matrix elements in Eq.(4.15, 4.16) becomes

$$\langle v\mathbf{k} | e^{(-i\mathbf{k}\cdot\mathbf{r})} \hat{\mathbf{e}} \cdot \mathbf{p} | c\mathbf{k} \rangle \approx \hat{\mathbf{e}} \cdot \langle v\mathbf{k} | \mathbf{p} | c\mathbf{k} \rangle. \quad (4.18)$$

The matrix elements of a momentum operator is related to the matrix elements of a position operator [92] by

$$\langle v\mathbf{k} | \mathbf{p} | c\mathbf{k} \rangle = \frac{im}{\hbar} (E_i - E_f) \langle v\mathbf{k} | \mathbf{r} | c\mathbf{k} \rangle. \quad (4.19)$$

This relation is proven in Appendix (C). From this relation, Eq.(4.18) becomes

$$|\langle v\mathbf{k} | \mathbf{p} | c\mathbf{k} \rangle|^2 = m^2 \omega^2 |\langle v\mathbf{k} | \mathbf{r} | c\mathbf{k} \rangle|^2. \quad (4.20)$$

Now, we can obtain a new expression for the transition rate by substituting Eq.(4.20) into Eq.(4.16) as follows

$$\gamma_i^f = \frac{2\pi}{\hbar} \frac{e^2 \omega^2}{c^2} A_0^2 \sum_{\mathbf{k}} |\langle v\mathbf{k} | \hat{\mathbf{e}} \cdot \mathbf{r} | c\mathbf{k} \rangle|^2 \delta(E_f - E_i - \hbar\omega). \quad (4.21)$$

Eq.(4.21) shows that the transition rate is totally proportional to the dipole matrix elements.

$$\gamma_i^f \propto \sum_{\mathbf{k}} |\langle v\mathbf{k} | \hat{\mathbf{e}} \cdot \mathbf{r} | c\mathbf{k} \rangle|^2 \quad (4.22)$$

We are going to deal only with Eq.(4.22), since the complete derivation will be done by Prof. Alexander Quandt in an upcoming article.

Now, we are concerned with the basic properties that enter the exciton lifetime, at which the transition rate is proportional to the transition dipole matrix elements, which includes the excitonic effect.

4.3 Basic properties that enter the exciton lifetime

The exciton lifetime is an important parameter to judge the efficiency of solar cells or photovoltaic devices. Sufficiently long lifetimes are critical, such that the exciton is able to diffuse a large distance to reach regions where it will disassociate, and electrons and holes will be separated. The exciton lifetime is the reciprocal of the transition rate, which is defined by Fermi's golden rule Eq.(4.21) or Eq.(4.22). We would like to include the excitonic effect in the transition dipole matrix elements that appears in Fermi's golden rule. We have two approaches to do this. The first is the Wannier approach with Fermi's golden rule and the second is the Bethe Salpeter approach with Fermi's golden rule.

4.3.1 Wannier approach with Fermi's golden rule.

In the following we describe the basic steps to determine dipole matrix elements and the parameters that enter the exciton lifetimes in the Wannier approach.

k.p perturbation theory

k · p perturbation theory or the **k · p** method determines wavefunction and energy bands in the vicinity of a known Bloch state. In the perturbation theory, the Hamiltonian is the sum of the unperturbed Hamiltonian H_0 and the perturbing Hamiltonian H'

$$H_{\mathbf{k},\mathbf{p}} = H_0 + H' \quad (4.23)$$

The Hamiltonian $H_{\mathbf{k},\mathbf{p}}$ and its eigenfunction $u_{n,\mathbf{k}}$ satisfy the following equation [75]

$$H_{\mathbf{k},\mathbf{p}}u_{n,\mathbf{k}} = E_{n,\mathbf{k}}u_{n,\mathbf{k}}, \quad (4.24)$$

where $H_{\mathbf{k},\mathbf{p}}$ is

$$H_{\mathbf{k},\mathbf{p}} = \frac{\mathbf{p}^2}{2m} + V + \frac{\hbar}{m}\mathbf{k} \cdot \mathbf{p} + \frac{\hbar^2\mathbf{k}^2}{2m}. \quad (4.25)$$

where V is the potential energy of the system. Comparing Eq.(4.23) with Eq.(4.25), the unperturbed Hamiltonian \mathbf{H}_0 and the perturbation Hamiltonian \mathbf{H}' are [75]

$$H_0 = \frac{\mathbf{p}^2}{2m} + V, \quad H' = \frac{\hbar}{m}\mathbf{k} \cdot \mathbf{p} + \frac{\hbar^2\mathbf{k}^2}{2m},$$

where

$$\mathbf{k} \cdot \mathbf{p} = (-i\hbar\frac{\partial}{\partial x})k_x + (-i\hbar\frac{\partial}{\partial y})k_y + (-i\hbar\frac{\partial}{\partial z})k_z.$$

If we have \mathbf{k}_0 at which $(\partial E/\partial \mathbf{k})_{\mathbf{k}_0} = 0$, we should take the second order of the **k · p** perturbation. The solution of Eq.(4.23) will be an expression for $E_{n,\mathbf{k}}$ and $u_{n,\mathbf{k}}$, as follows [75]

$$u_{n,\mathbf{k}} = u_{n,0} + \frac{\hbar}{m} \sum_{n' \neq n} \frac{\langle u_{n,0} | \mathbf{k} \cdot \mathbf{p} | u_{n',0} \rangle}{E_{n,0} - E_{n',0}} u_{n',0}, \quad (4.26)$$

$$E_{n,\mathbf{k}} = E_{n,0} + \frac{\hbar^2\mathbf{k}^2}{2m} + \frac{\hbar^2}{m^2} \sum_{n' \neq n} \frac{|\langle u_{n,0} | \mathbf{k} \cdot \mathbf{p} | u_{n',0} \rangle|^2}{E_{n,0} - E_{n',0}}. \quad (4.27)$$

The matrix elements in Eq.(4.27) can be written as

$$\langle u_{n,0} | \mathbf{k} \cdot \mathbf{p} | u_{n',0} \rangle = \langle u_{n,0} | \mathbf{p} | u_{n',0} \rangle \cdot \mathbf{k}.$$

where $\langle u_{n,0} | \mathbf{P} | u_{n',0} \rangle$ is a typical transition matrix elements, which is used in absorption and emission spectroscopy. Then Eq.(4.27) can be rewritten as [75]

$$E_{n,\mathbf{k}} = E_{n,0} + \frac{\hbar^2 \mathbf{k}^2}{2m} + \frac{\hbar^2}{m^2} \sum_{ij} \sum_{n' \neq n} \frac{|\langle u_{n,0} | \mathbf{P} | u_{n',0} \rangle|^2 k_i k_j}{E_{n,0} - E_{n',0}}, \quad (4.28)$$

To evaluate the optical transition matrix elements, we need to compare Eq.(4.28) to the formula that includes the effective mass [75] (See the discussion of the effective mass in the next section), we get

$$E_n(\mathbf{k}) = E(\mathbf{k}_0) + \frac{\hbar^2}{2m} \sum_{ij} \left(\frac{m}{m^*}\right)_{ij} \mathbf{k}_i \mathbf{k}_j, \quad (4.29)$$

Again, by comparing Eq.(4.28) with Eq.(4.29) we get

$$\left(\frac{m}{m^*}\right)_{ij} = \delta_{ij} + \frac{2}{m} \sum_{n \neq n'} \frac{|\langle u_{n,0} | \mathbf{P} | u_{n',0} \rangle|^2}{E_{n,0} - E_{n',0}}. \quad (4.30)$$

In this approximation, we ignored the spin-orbit interaction term in the Hamiltonian. This term is only important for degenerate or nearly degenerate bands [75]. Eq.(4.30) allows us to obtain the optical transition matrix using only the effective mass and the the knowing of the band gap. For more details, see [75].

Effective masses

The description of the motion and the behaviour of electrons and holes in a solid is represented by the $E - \mathbf{k}$ dispersion curve (the band structure). If the electrons are free, the $E - \mathbf{k}$ dispersion curve becomes parabolic and will be approximated as

$$E = \frac{\hbar k^2}{2m_e}. \quad (4.31)$$

where $\hbar k = p$ represents the momentum, $k = \frac{2\pi}{\lambda}$ represents the wave vector and λ is the de Broglie wavelength. Fig.(4.1) shows the GaAs band structure. As we see the $E - \mathbf{k}$ relation is in the Brillouin zone (BZ). The most important region in the band structure that we are interested in is the part of the dispersion curve, which is located at $\Gamma = (0, 0, 0)$. The valence band maximum and the conduction band minimum in the band structure are also located at Γ and their energy difference determines the band gap of the solid. In subsequent equations, we will use \mathbf{k}_0 to represent $\Gamma = (0, 0, 0)$.

To calculate the effective mass for both an electron and a hole, we start by expanding the $E(\mathbf{k})$ around the point \mathbf{k}_0 into a Taylor series [88] as

$$E_n(\mathbf{k}) = E(\mathbf{k}_0) + \frac{1}{2} \frac{\partial^2 E_n}{\partial \mathbf{k}^2} \cdot (\mathbf{k} - \mathbf{k}_0)^2 + O, \quad (4.32)$$

where the letter O is higher order term, which are negligible. $E(\mathbf{k}_0)$ is either the minimum conduction band energy or the maximum valence band energy. By substituting Eq.(4.31) into Eq.(4.32) we get

$$E_n(\mathbf{k}) = E(\mathbf{k}_0) + \frac{\hbar^2}{2m^*} (\mathbf{k} - \mathbf{k}_0)^2 + O, \quad (4.33)$$

where m^* is either the effective mass of the electron, which corresponds to the minimum of the conduction band energy or the effective mass of the hole, which corresponds to the maximum of the valence band energy. More generally, in three dimensions, the reciprocal effective mass

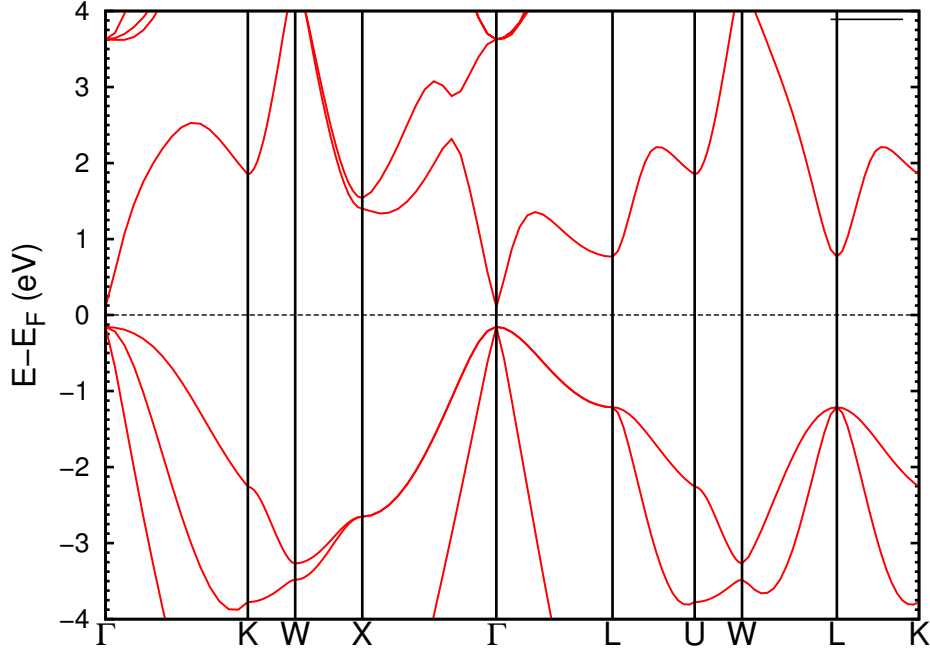


Figure 4.1: GaAs band structure with a high symmetry k-path coordinates in the BZ for GaAs bravais lattice.

in Eq.(4.33) can be defined as the reciprocal effective mass tensor $(\frac{1}{m^*})_{ij}$, such that Eq.(4.33) becomes [75][88]

$$E_n(\mathbf{k}) = E(\mathbf{k}_0) + \frac{\hbar^2}{2} \sum_{ij} (\frac{1}{m^*})_{ij} (\mathbf{k} - \mathbf{k}_0)_i (\mathbf{k} - \mathbf{k}_0)_j + O. \quad (4.34)$$

From the previous equation and Eq.(4.32), we can determine the effective mass as

$$(m^*)_{ij} = \frac{\hbar^2}{(\partial^2 E_n / \partial \mathbf{k}_i \partial \mathbf{k}_j)} \Big|_{\mathbf{k}=\mathbf{k}_0}, \quad (4.35)$$

where $\frac{\partial^2 E_n}{\partial \mathbf{k}^2}$ represents the curvature of the band. Eq.(4.35) shows that the curvature of the band is inversely proportional to the effective mass. In the case of GaAs Fig.(4.1), we see that the conduction band minimum has a larger curvature than the valence band maximum. This can be interpreted as the higher mobility of the hole than that of the electron, because the larger curvature implies smaller effective mass. For more details, see [88] [75].

Optical absorption and the excitonic effects

The momentum matrix elements for the transition from the vacuum $|0\rangle$ to the n exciton states $|n\rangle$ [73] is

$$\langle n|\mathbf{p}|0\rangle = \sum_{\mathbf{k}} \langle n|\mathbf{k}\rangle \langle \mathbf{c}\mathbf{k}|\mathbf{p}|\mathbf{k}v\rangle. \quad (4.36)$$

where $\langle \mathbf{c}\mathbf{k}|\mathbf{p}|\mathbf{k}v\rangle \cong \langle \mathbf{c}|\mathbf{p}|v\rangle$ over the range of \mathbf{k} involved in the transition. The probability of the transition [73] is proportional to

$$|\langle n|\mathbf{p}|0\rangle|^2 \propto |\langle \mathbf{c}|\mathbf{p}|v\rangle|^2 \left(\sum_{\mathbf{k}} \langle n|\mathbf{k}\rangle \right) \left(\sum_{\mathbf{k}'} \langle \mathbf{k}'|n\rangle \right). \quad (4.37)$$

$\langle \mathbf{k}|n\rangle$ can be determined from the relative wavefunction of the exciton, which is evaluated at r and was mentioned in Eq.(4.4) and Eq.(4.5). The relative wave function of the exciton [73] is

$$\phi_n(\mathbf{r}) = \sum_{\mathbf{k}} e^{i\mathbf{k}\cdot\mathbf{r}} \langle \mathbf{k}|n\rangle, \quad (4.38)$$

The lifetime is determine by an emission process, where photons will be created by the mutual annihilation of an electron and a hole. This happens when both electrons and holes having the same point in the space $\mathbf{r}_e = \mathbf{r}_h$ and the relative position is $\mathbf{r} = 0$. But the relative wavefunction $\phi_n(\mathbf{r})$ at $\mathbf{r} = 0$ [29][73] is

$$\phi_n(0) = \sum_{\mathbf{k}} \langle \mathbf{k}|n\rangle. \quad (4.39)$$

From Eq.(4.39) and Eq.(4.37), The transition probability [73] becomes proportional to

$$|\langle n|\mathbf{p}|0\rangle|^2 \propto |\langle c|\mathbf{p}|v\rangle|^2 |\phi_n(0)|^2. \quad (4.40)$$

$|\phi_n(0)|^2$ is nonzero only for hydrogen s states with zero angular momentum. The probability of the relative wavefunction is proportional to the derivative of the hydrogenic energy with respect to principle quantum number [29] as follows

$$|\phi_n(0)|^2 = \frac{1}{2\pi(\mathbf{r}_{exc})^3 E_B} \frac{dE_B(n)}{dn}, \quad (4.41)$$

From Eq.(4.8, 4.9), Eq.(4.41) becomes

$$|\phi_n(0)|^2 = \frac{1}{\pi(\mathbf{r}_{exc})^3 n^3}. \quad (4.42)$$

For more details, see [73][29].

4.3.2 Evaluating the dipole matrix elements that inter the exciton lifetime in the Wannier approach

Recall Eq.(4.22)

$$\gamma_i^f \propto \sum_{\mathbf{k}} |\langle v\mathbf{k}|\hat{\mathbf{e}} \cdot \mathbf{r}|c\mathbf{k}\rangle|^2$$

Here we focus on $|\langle v\mathbf{k}|\hat{\mathbf{e}} \cdot \mathbf{r}|c\mathbf{k}\rangle|^2$. This term is evaluated by using the following steps :

First, we start with the relation between the momentum operator and the position vector in the transition dipole matrix. Eq.(4.20) gives this relation as

$$|\langle v\mathbf{k}|\hat{\mathbf{e}} \cdot \mathbf{r}|c\mathbf{k}\rangle|^2 = \frac{1}{m_0^2 \omega^2} |\langle v\mathbf{k}|\hat{\mathbf{e}} \cdot \mathbf{p}|c\mathbf{k}\rangle|^2, \quad (4.43)$$

$|\langle v\mathbf{k}|\hat{\mathbf{e}} \cdot \mathbf{p}|c\mathbf{k}\rangle|^2$ can be evaluated using the $\mathbf{k} \cdot \mathbf{p}$ method, see Sec.(4.3.1), Eq.(4.30) as follows

$$\left[\left(\frac{m_0}{m^*} \right)_{ij} - \delta_{ij} \right] \frac{m_0 E_g}{2} = \sum_{\mathbf{k}} |\langle v\mathbf{k}|\hat{\mathbf{e}} \cdot \mathbf{p}|c\mathbf{k}\rangle|^2. \quad (4.44)$$

For exciton annihilation and creation the relative wavefunction $\phi_n(\mathbf{r})$ between the electron-hole pair Eq.(4.39) requires the position of the electron \mathbf{r}_e and the hole \mathbf{r}_h to be at the same point in space, see Sec.(4.3.1). The transition dipole matrix elements in Fermi's golden rule can be now written for the exciton transition as

$$\sum_{\mathbf{k}} |\langle v\mathbf{k}|\hat{\mathbf{e}} \cdot \mathbf{r}|c\mathbf{k}\rangle|^2 \approx V_{exc} \cdot |\phi_n(0)|^2 |\langle v\mathbf{k}_0|\hat{\mathbf{e}} \cdot \mathbf{r}|c\mathbf{k}_0\rangle|^2, \quad (4.45)$$

where V_{exc} is a suitable chosen exciton volume. Substituting the Eq.(4.45) into Eq.(4.22) we obtain

$$\gamma_i^f \propto V_{exc} |\phi_n(0)|^2 |\langle v\mathbf{k}_0 | \hat{\mathbf{e}} \cdot \mathbf{r} | c\mathbf{k}_0 \rangle|^2. \quad (4.46)$$

Finally, the lifetime follows from

$$\tau_{exc} = \frac{1}{\gamma_i^f}. \quad (4.47)$$

4.3.3 Bethe Salpeter approach with Fermi's golden rule

Evaluating the dipole matrix elements using the BSE approach is straightforward. We calculate the transition dipole matrix elements $|\langle v\mathbf{k}_0 | \hat{\mathbf{e}} \cdot \mathbf{r} | c\mathbf{k}_0 \rangle|^2$ (see Chapter.(3)), and then plug the results into Eq.(4.22). The lifetime is the reciprocal of the transition rate.

Chapter 5

Results

5.1 GaAs

We start with GaAs as a well known system and thus a perfect test for our main calculations. Ground state calculations were performed using the Quantum Espresso package [6]. We used a scalar relativistic norm conserving pseudopotential with the *GGA – PBE* Generalized gradient approximation for exchange correlation potential [96][99]. The electronic wave functions are expanded onto a plane-wave basis sets, which is truncated at an energy cutoff of 1088 eV using a k-point grid with dimensions $16 \times 16 \times 16$ in the Monkhorst-Pack scheme centred around $(0, 0, 0)$ [95]. Calculations of the excited state were performed using the Yambo package, which is based on many-body perturbation theory [7].

5.1.1 Crystal Structure

GaAs is a III-V direct band gap E_g semiconductor, with $E_g = 1.52$ eV at 0 Kelvin, which is obtained by fitting of photoluminescence data [101]. It has a zincblende crystal structure, which is a face centered cubic bravais lattice. Its space group is F-43m with lattice parameter $a = 5.731$ Å [100], see Fig.(5.1)

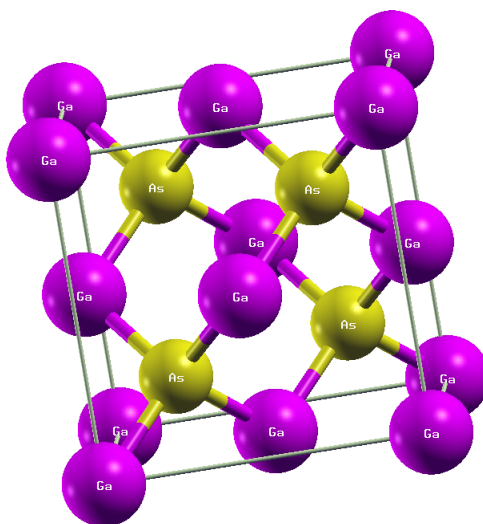


Figure 5.1: Crystal structure for GaAs.

5.1.2 Band structure and the band gap of GaAs

The calculated band structure using DFT for GaAs is shown in Fig.(4.1). The energies on the

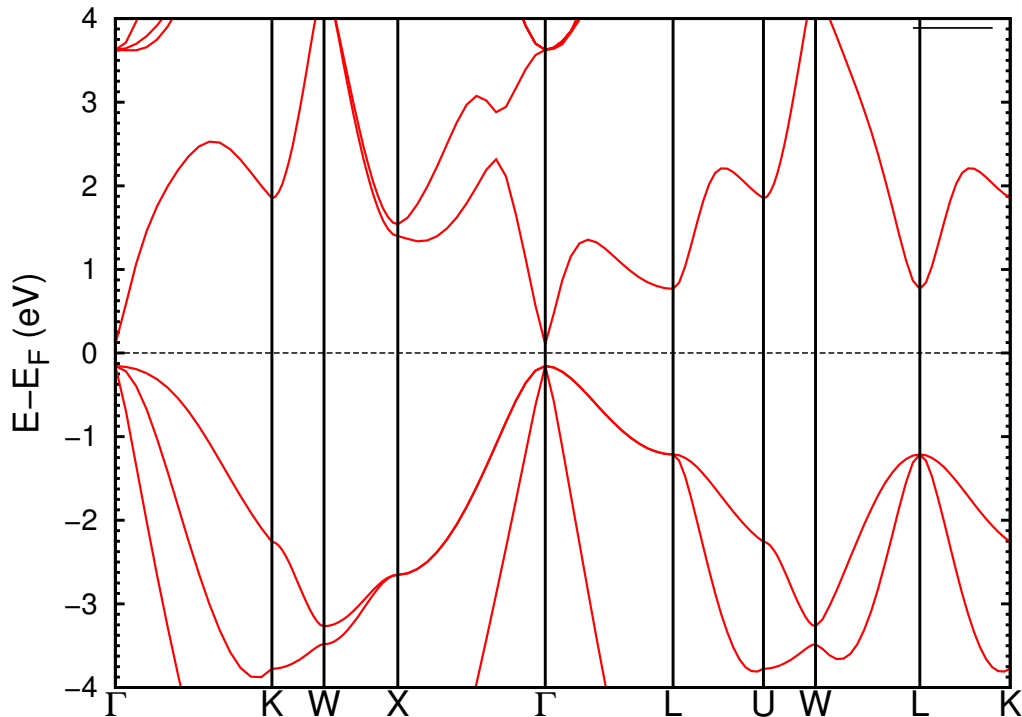


Figure 5.2: GaAs band structure.

y-axis are relative to the Fermi energy E_F , and the k-points on the x-axis are high symmetry k-points path in the Brillouin zone (BZ) for the GaAs bravais lattice [104]. The maximum of the valence band and the minimum of the conduction band are located at $\Gamma = (0, 0, 0)$ and the difference between their corresponding energies is the band gap energy, where the band gap is 0.26 eV based on GGA-PBE functional. In order to get the correct band gap, We calculated quasiparticle energies with a single shot GW approximation. Fig.(5.3) shows the difference between both approaches. The energies of the band 4, correspond to the maximum of the valence band and the energies of the band 5, correspond to the minimum of the conduction band. The quasiparticle correction of the band gap amounts to 0.6 eV and the quasiparticle band gap E_g^{QP} is 0.86 eV at k-point mesh with dimension $16 \times 16 \times 16$ centred around $(0, 0, 0)$.

We have found during the convergence tests at GW level that the dominant numerical parameter that limits the accuracy of the band gaps is the k-point grid. Table (5.1) shows the behaviour of the DFT band gap E_g^{DFT} and the quasiparticles band gap E_g^{QP} with increasing number of k-points. The DFT band gap E_g^{DFT} is less affected by changing the k-point grids but the quasiparticle band gap E_g^{QP} from the GW calculation has to be converged with increasing number of k-points. Thus our inability of performing GW calculations with a higher k-point grid prevents convergence. In order to get a converged value of the band gap, we need to select the k-point grids with dimensions of $50 \times 50 \times 50$ or more (see also the relation between the k-point grids and the dielectric function in Sec.(5.1.4) and Sec.(5.1.5)), this is an enormous computational effort, especially for a heavy calculation like GW. This can be circumvented by using a scissor operator as reported in the literature [101], which is equal to 1.52 eV at 0 Kelvin. We have also checked the influence of the scissor operator at BSE level in Sec.(5.1.5).

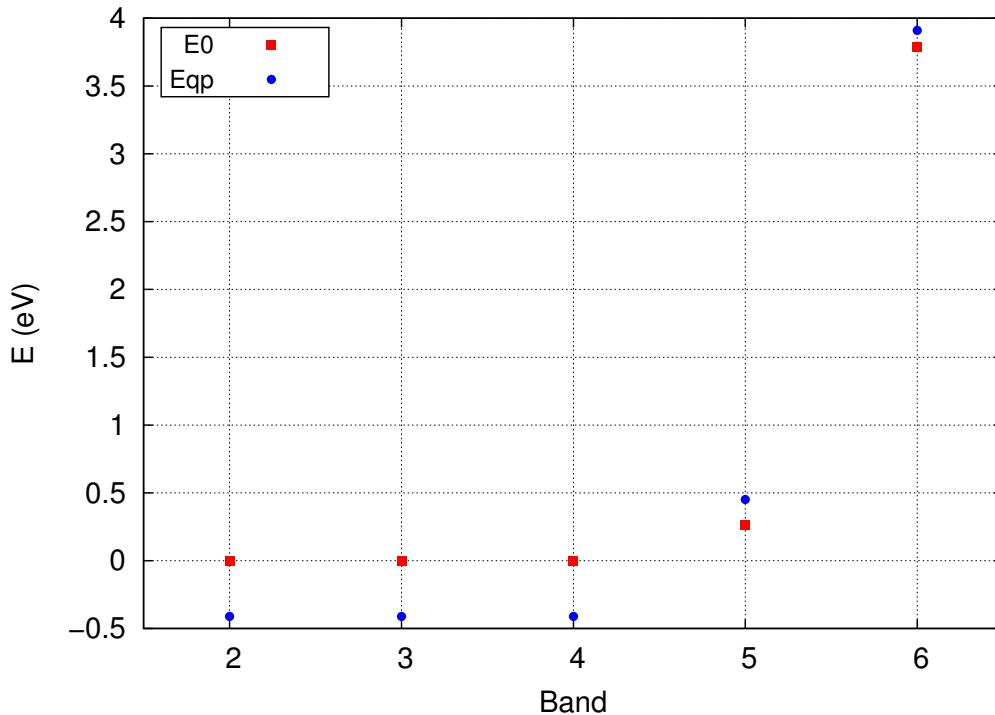


Figure 5.3: The difference in energies between the GW corected energies E_{qp} and DFT energies E_0 for GaAs at k-point mesh with dimension $16 \times 16 \times 16$ centred around Γ .

Table 5.1: k-point grids for E_g^{DFT} and E_g^{QP} calculations.

k-point set	E_g^{DFT}	E_g^{QP}
8 offset 0	0.262 eV	0.841 eV
10 offset 0	0.262 eV	0.847 eV
12 offset 0	0.263 eV	0.853 eV
14 offset 0	0.263 eV	0.858 eV
16 offset 0	0.263 eV	0.862 eV

5.1.3 Extracting the effective mass of an exciton from the band structure

We have discussed in detail the effective mass and the method for calculating it in chapter (4), Sec.(4.3.1) : We fit a parabola to the maximum of the valence band, and for the minimum of the conduction band in the $E - \mathbf{k}$ curve (DFT band structure) in Fig.(5.2). The maximum of the valence band and the minimum of the conduction band are located at $\Gamma = (0, 0, 0)$. Let us represent this point by \mathbf{k}_0 . We wrote a *Python* code to fit a parabola around the region, which includes the points E_{vm} (valence band maximum) and E_{cm} (conduction band minimum), and Γ . Recall Eq.(4.33)

$$E_n(\mathbf{k}) = E(\mathbf{k}_0) + \frac{\hbar^2}{2m^*}(\mathbf{k} - \mathbf{k}_0)^2 + \dots,$$

and compare it to the following polynomial equation

$$y = c_0 + c_1x + c_2x^2 + c_3x^3 + \dots.$$

From the fitting program, we then collect the value of the x^2 coefficient, which is supposed to

be $c_2 = \frac{\hbar^2}{2m^*}$. The effective mass finally can be written as

$$m^* = \frac{\hbar^2}{2c_2} \quad (5.1)$$

That way, we can find the value of the electron and hole effective masses and also from their values we can get the exciton effective mass as follows

$$m_e^* = 0.02 m_0, \quad m_h^* = 0.4 m_0, \quad \mu = 0.016 m_0. \quad (5.2)$$

where μ represents the exciton reduced mass. The values of electron and hole effective masses reported in [101] are $0.066 m_0$ and $0.5 m_0$, which are obtained by cyclotron resonance. If we compare the effective masses that we have calculated to the literature values, it is found that the hole effective mass is off by 20%, which is comparable. The electron effective mass is off by 70%, which is far from the literature value. The possible reason is related to the fitting method that we use, and the bands curvature in the band structure. The fitting procedure is more reliable if the band curvature is relatively small (in our case the band that corresponds to m_h^* for GaAs), and if the curvature is relatively large (the minimum conduction band that corresponds to m_e^* of GaAs). Otherwise, the fitting procedure will not be easy to fulfil. Consequently, it will need more k-points to fit it well.

5.1.4 The static dielectric constant

Next we calculate the static dielectric constant. There we have two ways to calculate it. The first one is based on many body approach, see Sec.(3.5). We will use this approach in this chapter. The second approach is Density Function Perturbation Theory (DFPT), see section (2.7), and [106]. This approach is implemented into the Quantum Espresso package [7]. Fig.(5.4) shows the static dielectric calculation with the DFPT approach at different sets of k-grids. A static dielectric constant can be deduced from this figure, which has a value ≈ 14.5 . We could not achieve a completely converged value for the static dielectric constant with respect to different k-point grids. It requires k-point grids with dimensions greater than $50 \times 50 \times 50$, which is computationally expensive. The static dielectric constant value that was reported in [101] amounts to 13 at 0 Kelvin. It is important to note that we did not converge our results with conduction (virtual) bands. It is fixed to 200 bands.

5.1.5 Absorption Spectrum

In the following we show the calculation of the dielectric function at different theories such as

- a) Independent-particle RPA (IP-RPA). In this level, the local field effect is neglected.
- b) RPA level including the local field effect.
- c) Bethe Salpeter equation.

Random phase approximation without Local field effects (IP-RPA)

A RPA dielectric function was calculated with k-point grids from $10 \times 10 \times 10$ to $35 \times 35 \times 35$ k-grid, increment by 5 at each time.

For the real part shown in Fig.(5.6) we noticed that:

- As the k-points increase, the value of the static dielectric constant decreases, which is the value corresponding to zero energy.

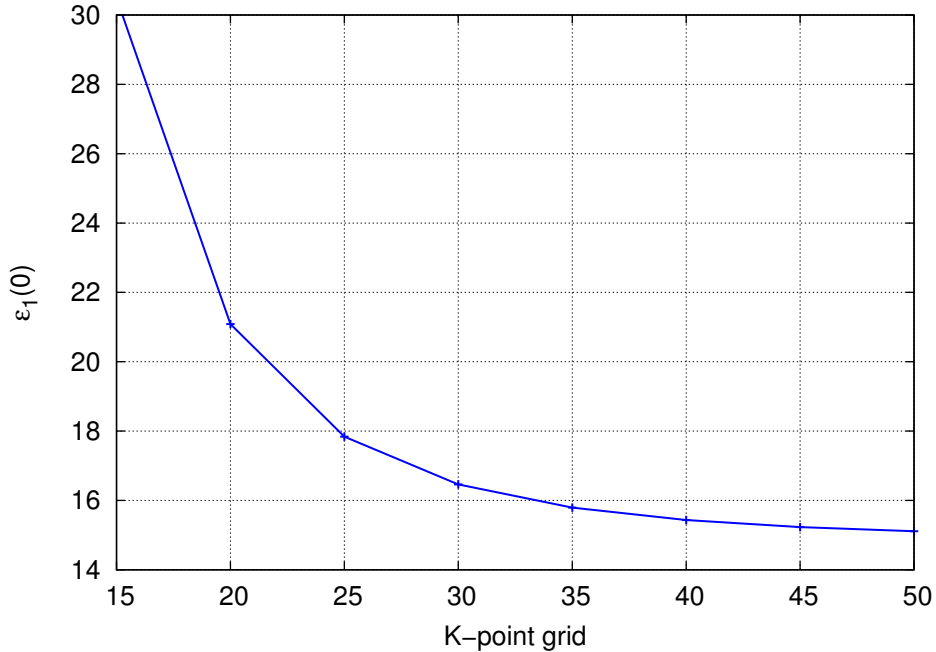


Figure 5.4: The convergence test of the static dielectric constant with respect to k-point grids for GaAs.

- As the k-points increase, the peaks are shifted towards lower energies, the height of the peaks decreases, and the energy difference between the peaks become smaller.

For the imaginary part shown in Fig.(5.5) we noticed that:

- As the k-points increase, the first peak remains the same for the whole set of k-point grids. It has the value 0.26 eV, which is the energy band gap corresponding to DFT calculation. The height of this peak decreases with increasing the k-point grid.
- As k-points increase, the energy difference between the peaks decreases and except for the first peak all other peaks are shifted to lower energies.

Each k-points grid recovers a different part of the total information of the system. If we further limit ourselves to grids with are centred around $\Gamma = (0, 0, 0)$ we find a peculiar behaviour. The first peak in the spectrum stays at the same position, while the other peaks seem to move towards lower energies. This can be explained as follows : The lowest possible energy transition is the direct transition $\Gamma - \Gamma$. As we always include this point, the position of the first peak remains fixed. The further we are away from the Γ -point the larger the energy difference between those bands and thus the transition energy. The closer a point is to Γ , the lower the transition energy in a k^2 -dispersion model. Therefore, it looks like the peaks in the spectrum are shifting towards lower energies, while we are actually just increasing the sampling density. One can consider a sampling to be dense enough, if such a behaviour is no longer observable.

Random phase approximation with Local field effect

The local field (LF) effect is related to dipole oscillations, induced by the external potential, see section (2.8). RPA with LF gives the complete physical picture of the system compared to RPA without LF [28] [29]. In Fig.(5.7), the difference between the absorption spectrum with LF and without LF effects are shown, where the difference appeared mostly in the strength of the absorption spectrum. The strength of the absorption spectrum within RPA without LF is higher

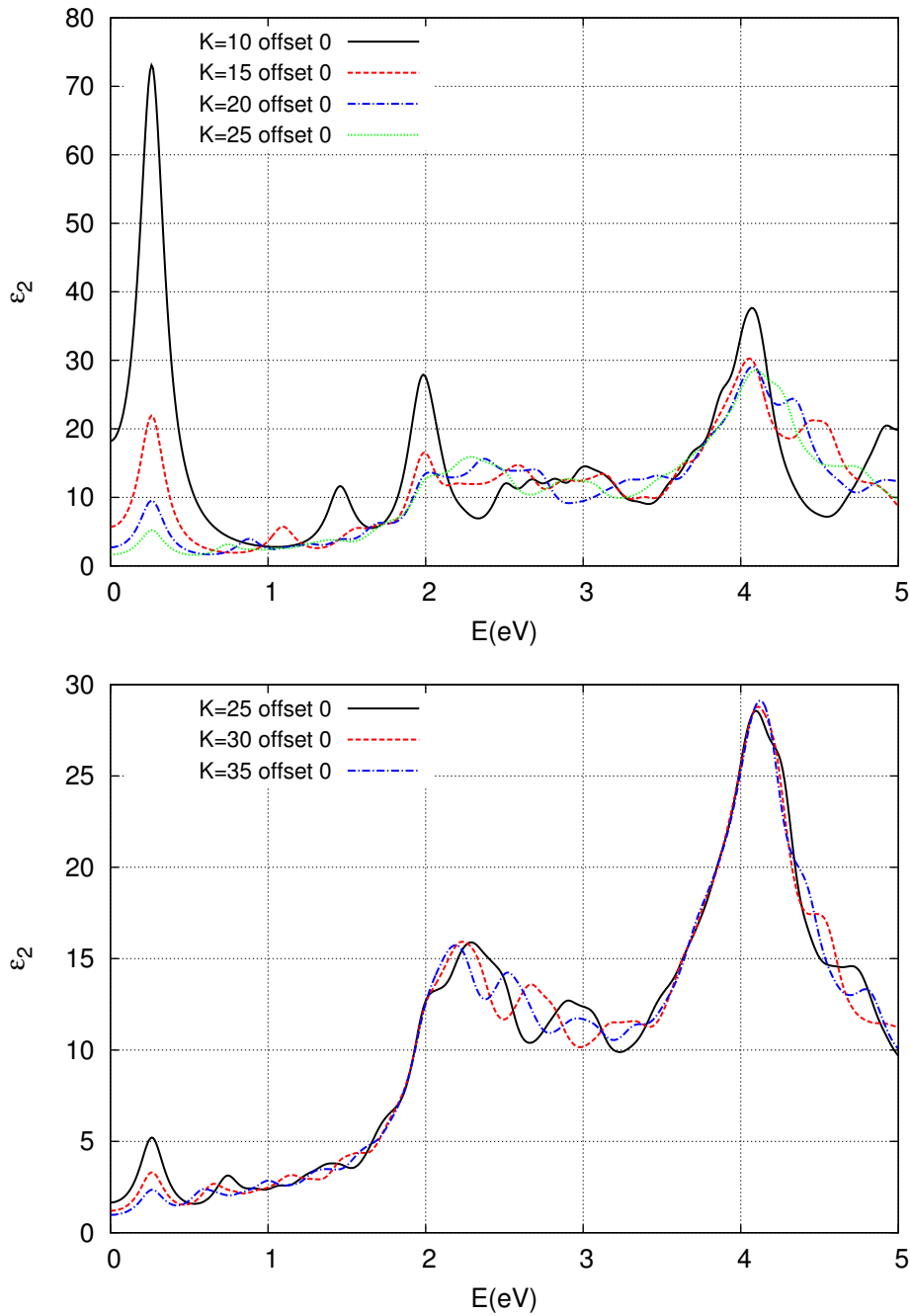


Figure 5.5: The imaginary part of the RPA dielectric function without local fields for different k-point grids.

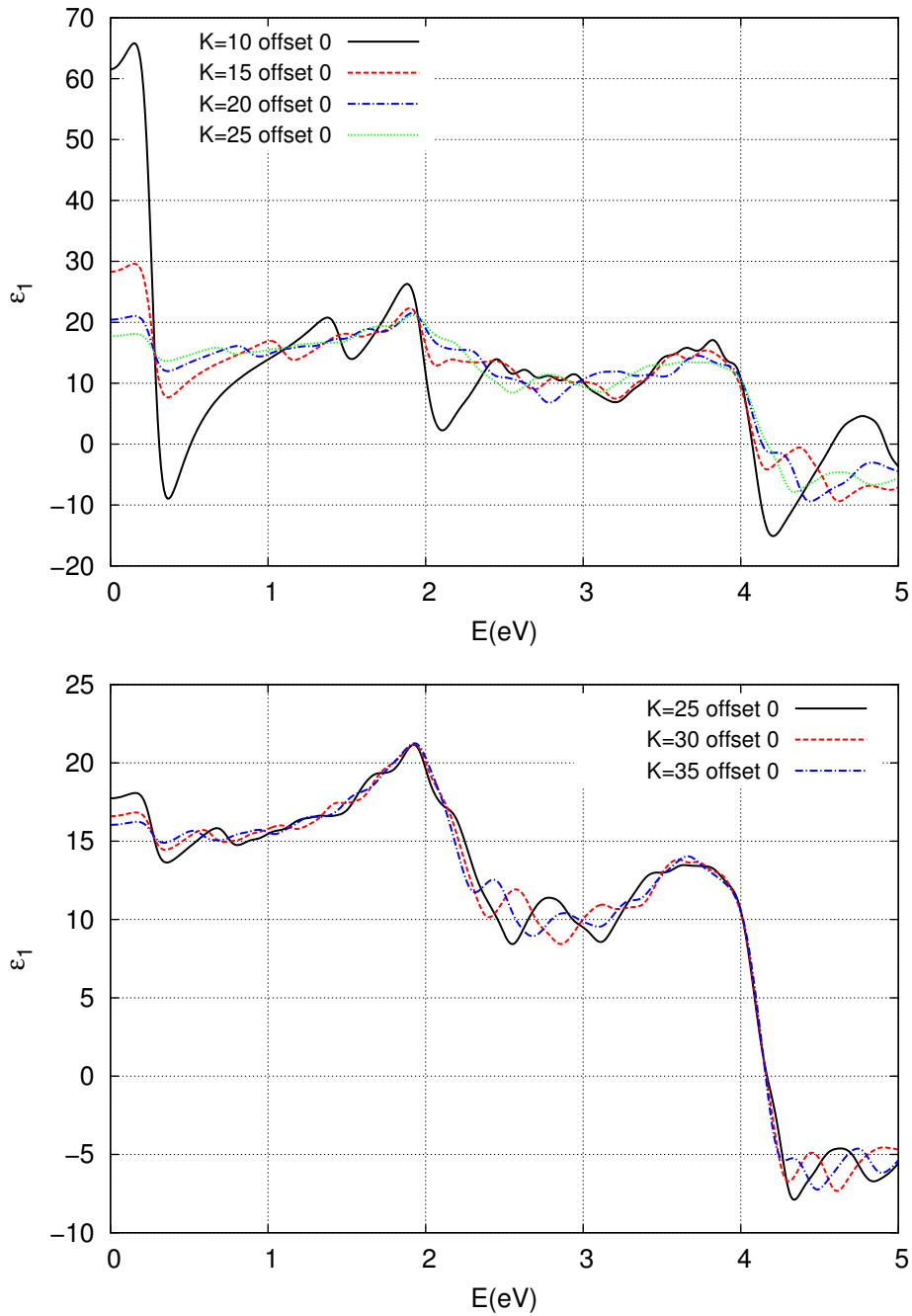


Figure 5.6: The real part of the RPA dielectric function without local fields for different k-point grids.

than the strength of the absorption spectrum within RPA with LF. This is because the induced LF reduces the overall field within the material itself due to the dipole-dipole interactions. Since the dielectric function is directly related to the response of the material to an external electric field. Therefore, the response function is affected by reducing the overall field within the material and in turn it will change the dipole matrix elements, which are used to evaluate the response function. The square of the dipole matrix elements in the oscillator matrix $\rho_{n'n\mathbf{k}}(\mathbf{q}, \mathbf{G}')$ in the response function equation Eq.(3.27) gives the strength of the transitions between the energy levels. Based on that, the absorption strength of the absorption spectrum within RPA with LF has to be less than the one without LF.

Bethe-Salpeter equation

The absorption spectrum within RPA shows disagreement with experiments, because the polarizability of the KS states is not the response of an interacting system, even if we include the GW eigenvalues (quasiparticle energies) and the corrected band gap that were calculated using GW approximation instead of the DFT band gap and KS eigenvalues. The reason for this failure is due to neglecting the electron-hole interaction, which originally comes from replacing the vertex function with delta functions (which is an unrealistic and very drastic approximation for the polarizability). This failure is resolved by the Bethe-Salpeter equation. For more details, see section (3.4.2). Fig.(5.8) shows us the discrepancies of the absorption spectrum between the two theories, BSE and IP-RPA. The first peak of IP-RPA is located at the band gap of GaAs (0.863 eV), while the first peak of BSE is at 0.842 eV. The difference between these two values gives the exciton binding energy, which has the value 20 meV. That shows us how the BSE treatment is important due to the e-h interaction inclusion. Also all peaks shifted (to the right in case of IP-RPA) and show the differences in their intensity.

The two graphs in Fig.(5.9) show the behaviour of the real part and the imaginary part of the BSE dielectric function with different sets of k-point grids. These behaviours are the same as the behaviours of the real part and the imaginary part of the RPA dielectric function, see section (5.1.5). As we see in Fig.(5.9) we have to use more k-point grids, due to numerical limitation. The reason for the limit in studying the BSE absorption spectrum with the higher k-point grids is dealing with complex and heavy calculation like BSE calculation with using the most expensive parameter, which is the k-point grids. The greater the number of divisions in the mesh is, the more memory is required, as well as CPU time taken. We also faced the same problem with GW calculation, see section (5.1.2).

There is a way to force a specific band gap with the so-called scissor-operator. We performed another analysis using this scissor-operator, instead of GW eigenvalues to check the effect of this method. We also compared it with the GW eigenvalues, see Fig.(5.10). The difference between BSE with including GW eigenvalues (quasiparticle corrections) and BSE with the scissor-operator in Fig.(5.10) appears only after the first peak of the absorption spectrum. The action of the scissor-operator simply opens the DFT gap and corrects the band structure, but we can not use it in many cases because it misses the self-energy correction for the particles. In our case the scissor-operator method is effective because we are interested in the bound excitons, where their energies are lower than the band gap by several milli-electron volts.

5.1.6 Exciton analysis

Bethe-Salpeter approach

In the BSE absorption spectrum, which is shown in Fig.(5.10), the first peak in the spectrum represents the bound exciton and the energy corresponding to this peak represents the energy

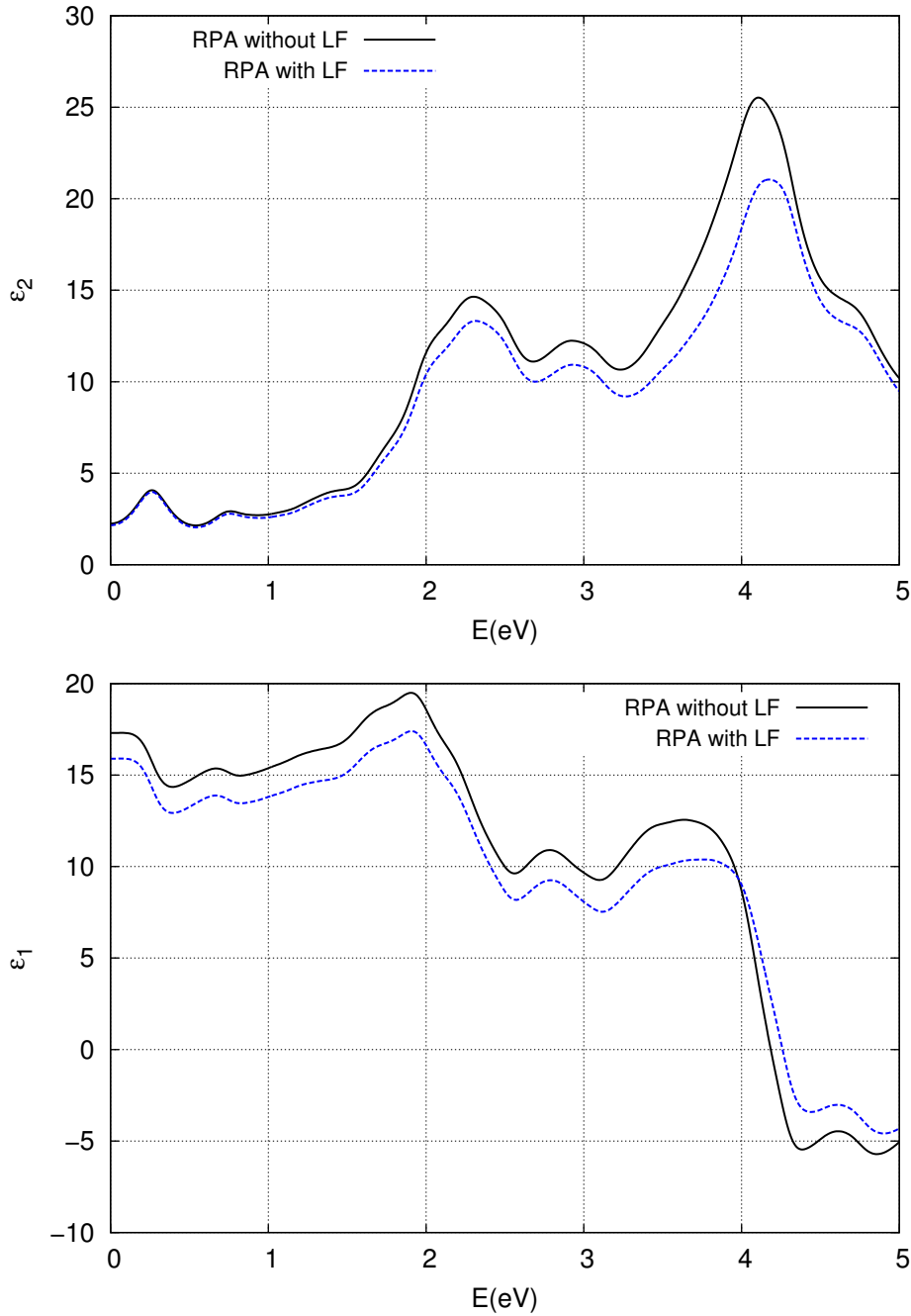


Figure 5.7: RPA dielectric function without and with local fields (LF) at the k-point grid $25 \times 25 \times 25$ around Γ . The imaginary part of the dielectric function is at the top, and the real part is at the bottom.

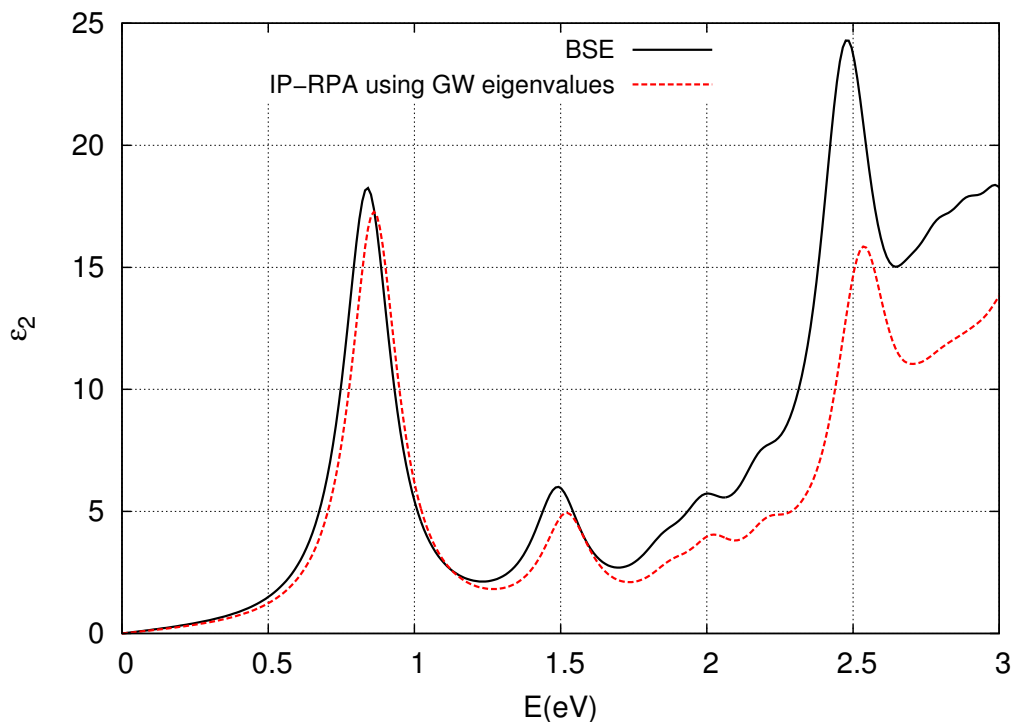


Figure 5.8: Absorption spectra of GaAs for BSE and IP-RPA using GW eigenvalues (quasiparticles correction) at k-point grids with dimension $16 \times 16 \times 16$ around Γ .

E_{exc} required to create this exciton. We would also like to add note that we have considering the effect of the k-point grids on the exciton energy and its binding energy E_B , thus, see table (5.2)

Table 5.2: k-point grids with respect to the exciton energy E_{exc} and exciton binding energy E_B .

k-point set	E_g^{QP}	E_{exc}	E_B
10 offset 0	0.847 eV	0.832 eV	15 meV
14 offset 0	0.858 eV	0.842 eV	16 meV
16 offset 0	0.862 eV	0.842 eV	20 meV

The first thing that we can realize in the table is increasing the values of E_g^{QP} and E_{exc} by increasing the k-point grid, but only E_{exc} starts to be converge at k-point grids of dimension $14 \times 14 \times 14$ centred around Γ . The difference between E_g^{QP} and E_{exc} gives the exciton binding energy E_B . We found that E_B fluctuates between 15 and 25 meV. That is because the E_g^{QP} changes with the k-point grids (not converged) and E_B depends of course on E^{QP} . We have also noticed that an increase in the k-point grids leads to a decrease in the value of the dielectric constant. Consequently, the binding energy increases, in agreement with Eq.(4.9).

The exciton analysis is preformed at k-point grid with dimensions $16 \times 16 \times 16$ centred around Γ . We look for the bound exciton in the transition region at Γ by looking for the highest strength excitons in the first peak region, which can be determined by analysing Fig.(5.11). The strength is given by the square of the dipole matrix element of the transition. It is directly related to the probability of absorption of the electromagnetic radiation for this transition. The lowest energetic exciton that has the highest strength in the first peak region has an energy of 0.842

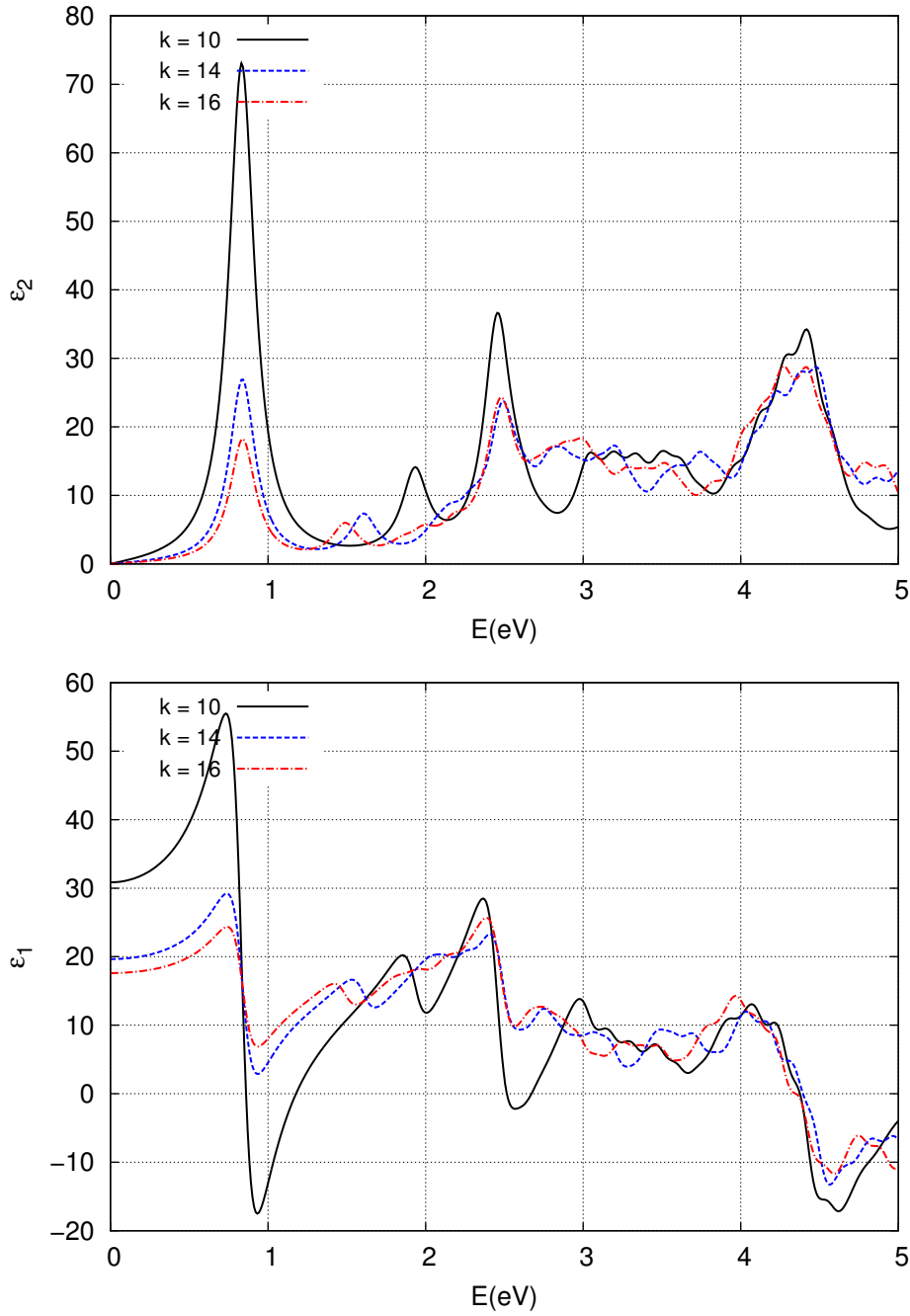


Figure 5.9: BSE dielectric function of GaAs for different set of k-point grids. The imaginary part of dielectric function is at the top, and the real part is at the bottom.

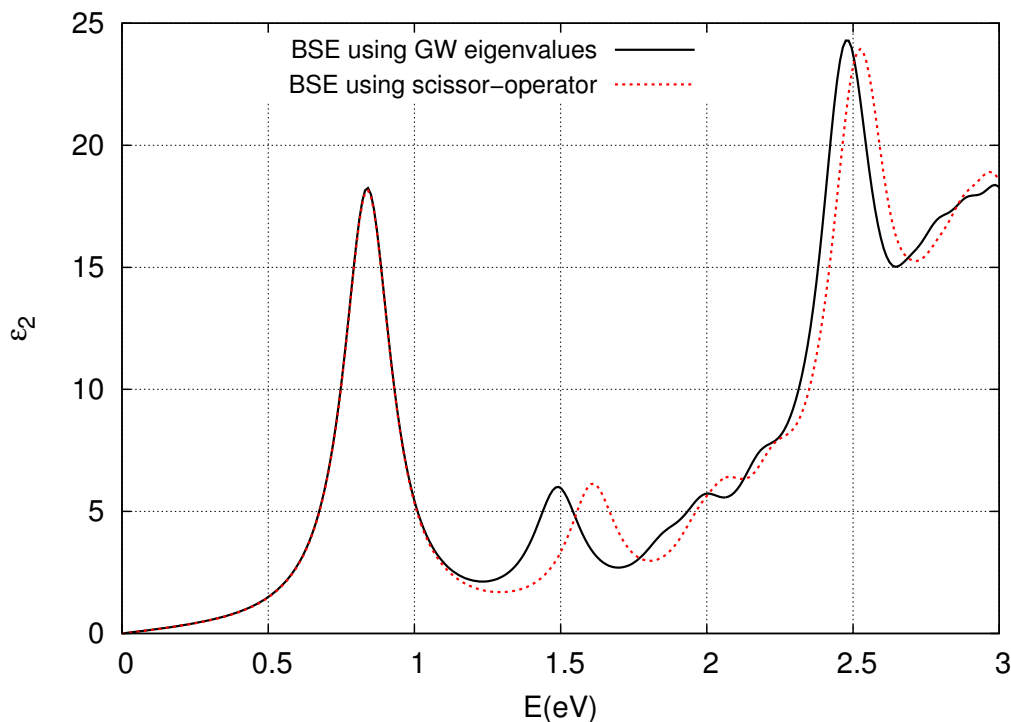


Figure 5.10: Absorption spectra of GaAs for BSE using GW eigenvalues and scissor operator for k-point grids with dimension $16 \times 16 \times 16$ around Γ .

eV. According to this value, we can calculate the exciton binding energy as follows

$$E_B = E_g - E_{exc} = 0.862 \text{ eV} - 0.842 \text{ eV} = 0.02 \text{ eV} = 20 \text{ meV}$$

We would also like to add that the exciton binding energy in GaAs has been studied by photoluminescence. It has value $4.2 \pm 0.3 \text{ meV}$ [102], and reported as an estimation 13 meV and 20 meV for the light and heavy hole excitons respectively in GaAs Quantum well with well size $L_z \approx 120 \text{ \AA}$ [103]. The exciton binding energy value that we calculated differs from the literature. The reason for this disagreement in our calculation could be related to the lack of convergence of numerical parameters and the limitation in the theoretical determination.

Sometimes the stability of the exciton with temperature is one of the obstacles that stops us from observing the exciton. We can estimate the highest temperature at which the exciton can be possible to observe. The minimum thermal energy that required to rip the exciton apart has to be $E_B \approx k_B T$, where the $E_B = 20 \text{ meV}$ and k_B is the Boltzman constant. So that we can expect that the exciton will not be stable above temperature $T \approx 232 \text{ K}$.

Exciton transitions

The transition states that are involved in the excitation for strongest (the highest strength) exciton in the first peak region. The data that stated in table (5.3) shows the transitions of single particle states to the excitation states. The weights that correspond to the transition states in the excitation is almost one. This means that the states that are corresponding to these weights are probably the only major contribution in the transition process at Γ point. Moreover, these weights imply that the product of the DFT wavefunctions for the conduction band and the valence band are close to their corresponding BSE wavefunction for e-h pair. From table (5.3) the highest transition probability is between band 4 and band 5, which is for

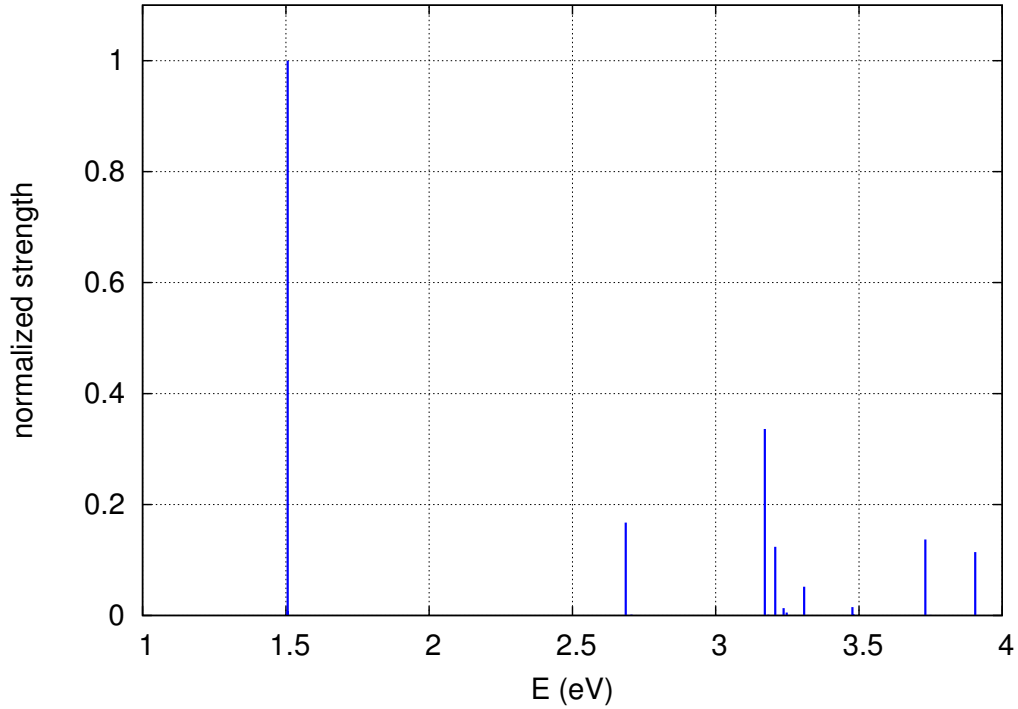


Figure 5.11: The strength of the excitons in energy range from 0 to 4 eV.

Table 5.3: The transition states involved in the excitation at Γ k-point

k-point		
	0.0	0.0
Valence band	Conduction band	Weight
4.0	5.0	0.99965
2.0	5.0	0.99964
3.0	5.0	0.99963

the heavy hole exciton and for the light hole exciton between is band 2 and band 5. These transitions happen at Γ point.

Exciton wavefunction

The exciton wavefunction shows the probability amplitude for an electron with respect to the hole, which is a function of hole and electron position. Fig.(5.12) shows the exciton wavefunction in three dimensions with three unit cell repeated into three dimension with respect to fixed hole position at the location of the central As atom. Fixing the hole position and calculating the wavefunction for the electron with respect to the fixed hole is the only available choice for the moment being. We choose a hole position in space according to the large density of the valence bands that mainly contribute to this exciton, where the whole picture of the exciton wavefunction depends on the position of the hole. In the Fig.(5.12), the exciton wavefunction is drawn for As atom and surrounded by Ga atoms at which the electronic properties happen between the Ga cation and As anion.

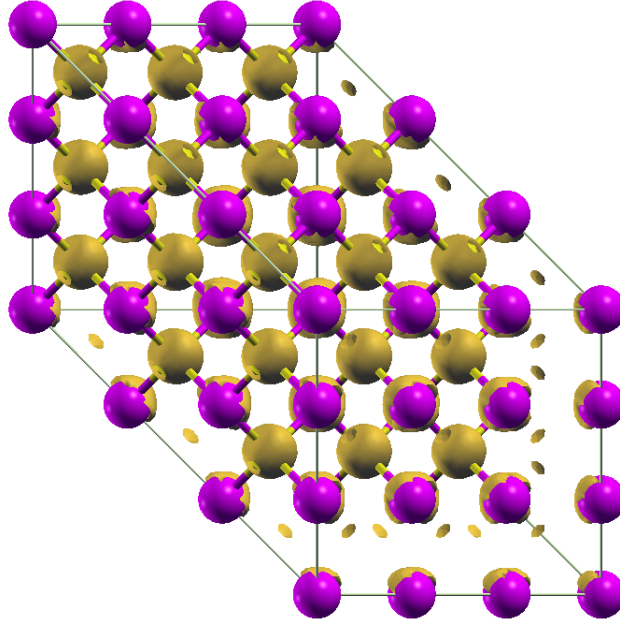


Figure 5.12: Exciton wavefunction for GaAs with isovalue of the isosurface 50% of the maximum value. The yellow balls are As atoms and the other balls are Ga atoms.

The Wannier approach

As the key numerical factor that determines the exciton lifetimes, we now calculate the dipole matrix elements in the Wannier approach, which is discussed in details in chapter (4), Sec(4.3.1). We start with calculation of the electron, hole, and exciton effective mass

$$m_e^* = 0.02 m_0, \quad m_h^* = 0.4 m_0, \quad \mu = 0.016 m_0 \quad (5.3)$$

where μ symbolize the exciton reduced mass. The exciton in the Wannier approach is modelled as a hydrogenic system. In this model, we can determine the excition properties as follows: For calculating the exciton binding energy with the orbital $n = 1$,

$$E_B = \frac{\mu}{m_0 \epsilon_r(0)^2} E_{Ry} = 1.3 \text{ meV}. \quad (5.4)$$

where $\epsilon_r(0) = 14.5$ is the static dielectric constant, see Sec.(5.1.4). The value of the exciton binding energy for GaAs is 4.2 ± 0.3 meV from photoluminescence study [102]. The value of the exciton binding energy that we calculated in the latter equation is underestimated because the exciton reduced mass is underestimated as stated in Sec.(5.1.3).

The stability of the exciton is one of the obstacles that we face, especially with temperature. The exciton binding energy allows us to estimate the highest temperature at which the exciton can be observed before it is ripped apart. The maximum thermal energy that is required to make the exciton stable towards the temperature is $E_B \approx k_B T$. We can expect that the exciton most likely will not be stable above ≈ 15 K. This temperature in a different analysis is ≈ 50 K in [72], due to using underestimated exciton reduced mass for calculating the exciton binding energy.

For calculating the exciton energy, we use

$$E_{ex} = E_g - E_B = 0.862(\text{eV}) - 1.3(\text{meV}) = 0.861 \text{ eV}. \quad (5.5)$$

where $E_g = 0.862$ eV is the energy gap, this value is calculated at k-point grid with dimension $16 \times 16 \times 16$ centred around Γ .

For calculating the exciton radius with the orbital $n = 1$,

$$r_{exc} = \frac{m_0}{\mu} \epsilon_r(0) n^2 r_{Ry} = 725 r_{Ry} \approx 38 \text{ nm.} \quad (5.6)$$

The exciton radius for GaAs is reported also in [72], and it has the value 13 nm. The radius of the Wannier exciton with orbital quantum number $n = 1$ as in Eq.(5.6) is a large radius which covers many unit cells. According to this value, we are able to estimate how many unit cells of GaAs, at which the exciton volume can cover. The unit cell dimensions of GaAs is $a = 5.731 \text{ \AA}$, and its volume is $1.88 \times 10^{-28} \text{ m}^3$. The volume that is occupied by the exciton with the radius $r_{exc} = \frac{4}{3}\pi r_{exc}^3$ is $2.35 \times 10^{-22} \text{ m}^3$. Therefore, the exciton volume covers 1.25×10^6 unit cells. It is also reported in [72] the exciton volume can contain 5×10^4 unit cells. We can conclude this part by saying the exciton binding energy and the exciton radius are directly related to the exciton reduced mass and the dielectric constant as well, see Eq.(5.4) and Eq.(5.6). The results and the analysis have a small deviation from the literature values due to the exciton reduced mass is underestimated as stated in Sec.(5.1.3).

The next step is to calculate the transition dipole moment. We start by evaluating the probability of the relative wave function for e-h pairs at zero separation

$$|\phi_n(0)|^2 = \frac{1}{\pi(r_{exc})^3 n^3} = 5.63 \times 10^{21} \text{ m}^{-3} \quad (5.7)$$

The dipole matrix element from the $\mathbf{k} \cdot \mathbf{p}$ method is

$$\left(\frac{m_0}{m^*}\right)_{ij} = \delta_{ij} + \frac{2}{m_0} \sum_{\mathbf{k}} \frac{|\langle v\mathbf{k}|\mathbf{p}|\mathbf{c}\mathbf{k}\rangle|^2}{E_g}, \quad (5.8)$$

$$|\langle v\mathbf{k}|\mathbf{p}|\mathbf{c}\mathbf{k}\rangle|^2 = 9.4 \times 10^{-50} (\text{Kg.m.s}^{-1})^2$$

The value that we obtained for the transition dipole matrix is comparable to the literature value, see table (5.4)

Table 5.4: The transition dipole matrix elements form the $\mathbf{k} \cdot \mathbf{p}$ method, and the literature.

$ \langle v\mathbf{k}_0 \mathbf{p} \mathbf{c}\mathbf{k}_0\rangle ^2$	Its source
$\approx 6.25 \times 10^{-49} (\text{Kg.m.s}^{-1})^2$	Literature [110][111]
$9.4 \times 10^{-50} (\text{Kg.m.s}^{-1})^2$	$\mathbf{k} \cdot \mathbf{p}$ method

The relation between the momentum \mathbf{p} matrix and the position \mathbf{r} matrix is

$$|\langle v\mathbf{k}|\hat{\mathbf{e}} \cdot \mathbf{r}|\mathbf{c}\mathbf{k}\rangle|^2 = \frac{1}{m_0^2 \omega^2} |\langle v\mathbf{k}|\hat{\mathbf{e}} \cdot \mathbf{p}|\mathbf{c}\mathbf{k}\rangle|^2 = 6.6 \times 10^{-20} \text{ m}^2 \quad (5.9)$$

The transition dipole matrix in the Wannier approach is discussed in Sec.(4.3.2) and represents in Eq.(4.45)

$$\begin{aligned} \sum_{\mathbf{k}} |\langle v\mathbf{k}|\hat{\mathbf{e}} \cdot \mathbf{r}|\mathbf{c}\mathbf{k}\rangle|^2 &\approx V_{exc} \cdot |\phi_n(0)|^2 |\langle v\mathbf{k}_0|\hat{\mathbf{e}} \cdot \mathbf{r}|\mathbf{c}\mathbf{k}_0\rangle|^2 \\ &\approx (2.3 \times 10^{-22}) \times (5.6 \times 10^{21}) \times (6.6 \times 10^{-20}) \approx 8.5 \times 10^{-20} \text{ m}^2 \end{aligned} \quad (5.10)$$

The transition rate, which is directly proportional to the dipole matrix elements

$$\gamma_i^f \propto V_{exc} \cdot |\phi_n(0)|^2 \cdot |\langle v\mathbf{k}_0|\hat{\mathbf{e}} \cdot \mathbf{r}|\mathbf{c}\mathbf{k}_0\rangle|^2. \quad (5.11)$$

where $V_{exc} = \frac{4\pi}{3}(r_{exc})^3 = 2.35 \times 10^{-22} \text{ m}^3$. The lifetime is simply the reciprocal of the transition rate.

5.2 $\alpha - CH_3NH_3PbI_3$

In the ground state calculations stage, the calculations were performed by using the Quantum espresso package [6]. The pseudopotential employed is a norm conserving pseudopotential with the $GGA-PBE$ for exchange correlation potential [96]. The pseudopotential is fully relativistic, where includes spin orbital coupling (SOC) for lead and iodine atoms, and scalar-relativistic pseudopotential for the rest [97]. The electronic wave functions are expanded onto a plane-wave basis sets, which is truncated to an energy cutoff of 816 eV using a k-point grid with dimensions $6 \times 6 \times 6$ Monkhorst-Pack centred around $\Gamma = (0, 0, 0)$ [95]. Calculations of the excited state were performed by using the Yambo package [7].

5.2.1 Crystal Structure

In this work, we deal with organic-inorganic hybrid metal perovskites, which have a general formula ABX_3 , where A symbolizes the organic cation methylammonium CH_3NH_3 , B is Sn or Pb and X_3 symbolizes I, Cl, or Br. These materials have a power conversion efficiency (PCE), reaching up to 20% with low cost production methods within a period of five years [94].

Through this work, we are going to use α phase methylammonium lead iodine $\alpha-CH_3NH_3PbI_3$, which has tetragonal crystal structure with space group P4mm and the lattice parameters are $a = b = 6.3115 \text{ \AA}$ $c = 6.3161 \text{ \AA}$ [94]. The crystal structure of this material is shown in Fig.(5.13) and Fig.(5.14)

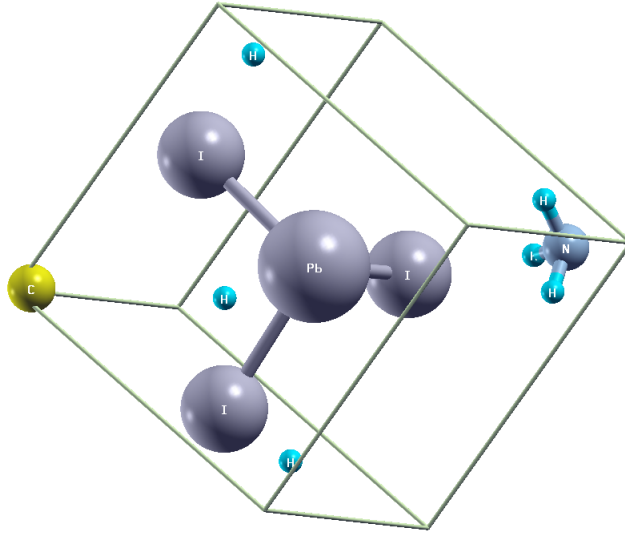


Figure 5.13: Crystal structure of perovskite $\alpha - CH_3NH_3PbI_3$.

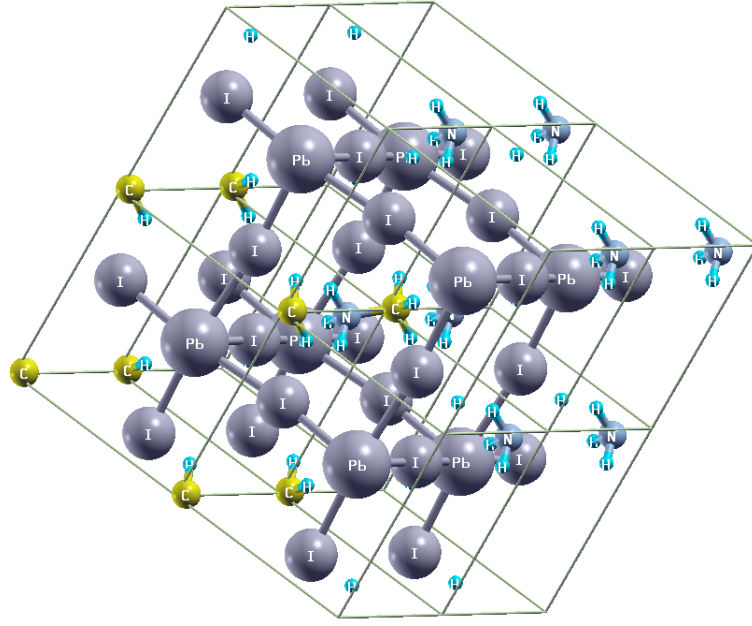


Figure 5.14: Crystal structure of perovskite $\alpha - CH_3NH_3PbI_3$ with two unit cells repeated into three dimensions.

5.2.2 Band structure and the band gap of $\alpha - CH_3NH_3PbI_3$

The DFT band structure for $\alpha - CH_3NH_3PbI_3$ is shown in the Fig.(5.15). The energies on

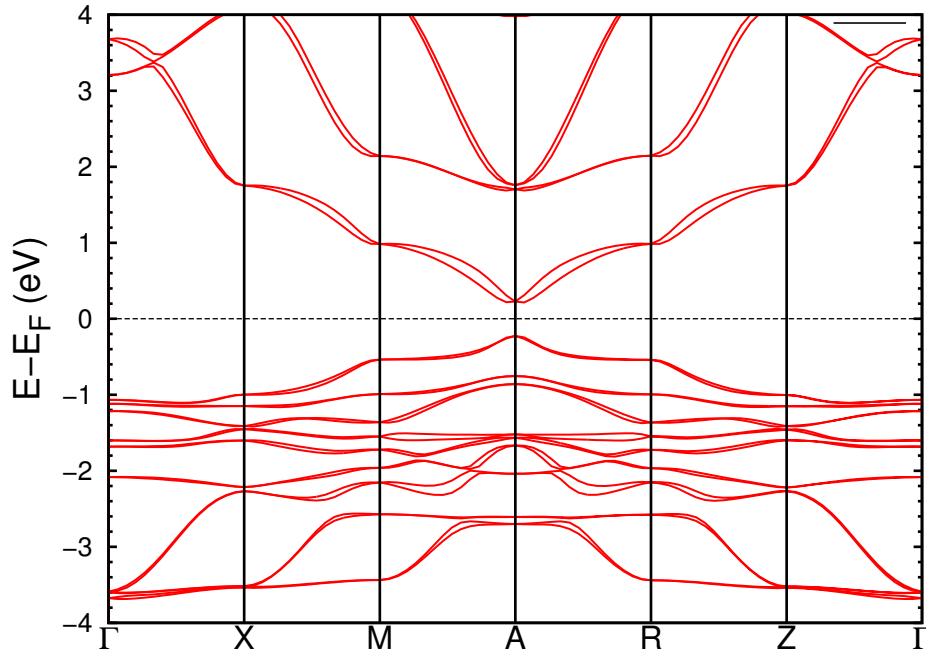


Figure 5.15: DFT Band structure of $\alpha - CH_3NH_3PbI_3$

the y-axis are relative to E_F and the k-points on the x-axis are high symmetry k-points path coordinates in the BZ for the $\alpha - CH_3NH_3PbI_3$ bravais lattice [104]. The maximum of the valence band and the minimum of the conduction band are located at $A = (0.5, 0.5, 0.5)$. The location of the electronic band gap is reported in [107] at point A for this structure. The band

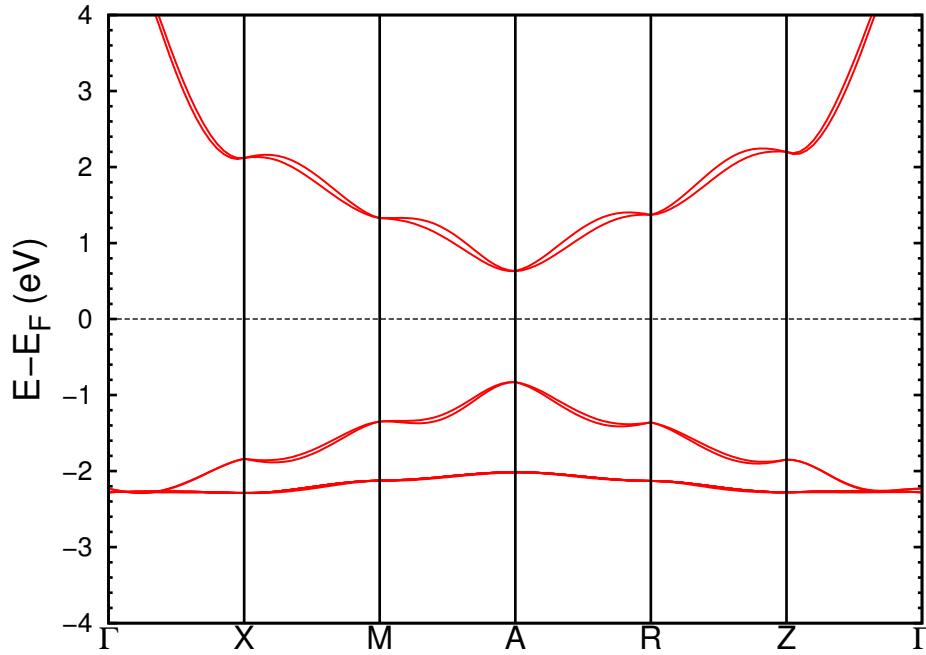


Figure 5.16: GW Band structure of $\alpha - CH_3NH_3PbI_3$ for the three bands above and three bands below the Fermi level.

structure in Fig.(5.15) shows that the energy band gap has a value $E_g = 0.45$ eV. This value is too small for a semiconductor. We include the corrected energies from GW calculations in order to get the correct band gap. We draw the GW band structure, which is shown in Fig.(5.16). We included the GW eigenvalues (quasiparticles corrections) for the three bands above and three bands below the Fermi level. The corrected band gap is $E_g = 1.55$ eV. The experimental band

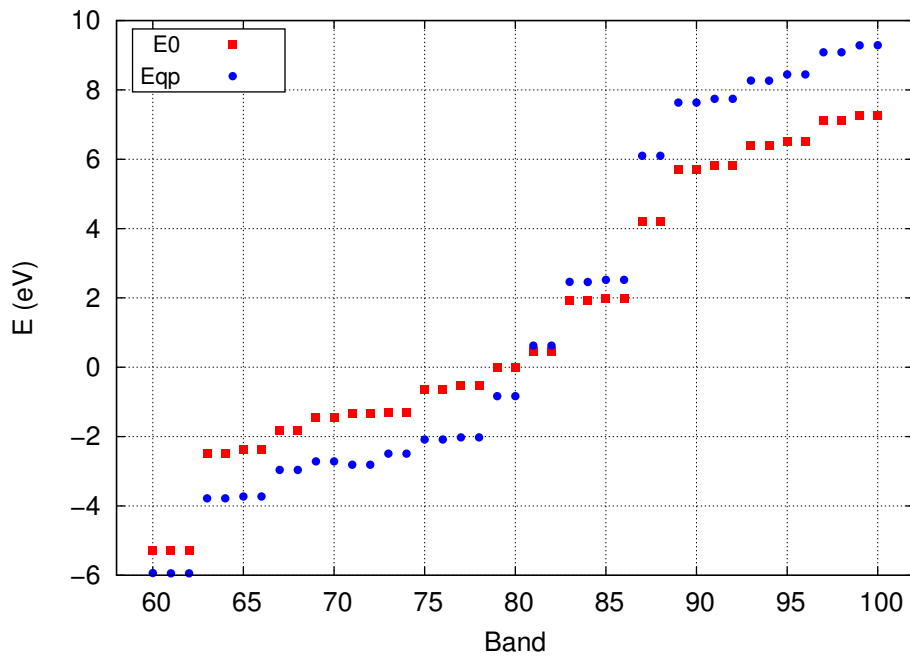


Figure 5.17: The difference in energies between the GW corrected energies and DFT energies of $CH_3NH_3PbI_3$.

gap of a similar structure is determined by the fitting of photoluminescence data and equals 1.52 eV [98]. Fig.(5.17) shows to what extent the GW corrected energies differ from the DFT energies. By looking at the values of the energies between the band 80, which is the maximum of the valence band and the band 81, which is the minimum of the conduction band, we can obtain the correction of the band gap, which equals 1.1 eV.

5.2.3 Extracting the effective mass of an exciton from the band structure

We follow the same procedure for calculating the effective mass for GaAs in Sec.(5.1.3). This method is discussed in chapter (4), Sec.(4.3.1)). The values of the effective mass of the electron and hole are as follows

$$m_e^* = 0.22 m_0, \quad m_h^* = 0.14 m_0, \quad \mu = 0.086 m_0. \quad (5.12)$$

where μ is the exciton reduced mass. As discussed in Sec.(5.1.3), the fitting method for calculating the effective mass is an approximate method and comparable to the literature if the band curvature is not extremely small. In the case of the $\alpha - CH_3NH_3PbI_3$ band structure in Fig.(5.16), the highest valence band curvature and the lowest band curvature are not small. Consequently, we fully expect that the effective mass that we calculated for this structure is very close to the actual values.

5.2.4 The static dielectric constant

The static dielectric constant for $\alpha - CH_3NH_3PbI_3$ is calculated using the same method as discussed in Sec.(5.1.4). Fig.(5.4) shows the static dielectric constant calculated at different sets of k-point grids. A static dielectric constant can be deduced from Fig.(B.1), which has a value ≈ 6.7 . Achieving a completely converged value for the static dielectric constant with respect to different k-point grids is computationally expensive. It requires k-point grids with dimensions greater than $11 \times 11 \times 11$ in order to achieve a satisfactory converged value for the static dielectric constant.

5.2.5 Absorption Spectrum.

We studied the optical absorption at different theories in section.(5.1.5). In this section, we will go directly through the absorption spectrum at the BSE level.

In the beginning, we need to see what will happen for the optical absorption spectrum and the exciton behaviour in the system if we change the system dependent parameters in both the ground state calculation and the excited state calculation. The convergence test for these parameters is done for both GaAs and $\alpha - CH_3NH_3PbI_3$. We get the same behaviour for these parameters for both systems. We mention this study in detail due to its importance in this work. We invite the reader to see appendix (B).

The absorption spectrum at the BSE level of theory

The convergence tests that we have done in appendix (B) allow us to optimise numerical parameters in both the ground state calculations and the excited state calculations. We used these converged parameters to do the final calculations. Based on that we can judge or analyse the results that we get in a more satisfactory way.

After diagonalizing the excitonic matrix, we can get the macroscopic dielectric function. The imaginary part of the macroscopic dielectric function is directly related to the absorption spectrum, as shown in Fig.(5.19). The static dielectric constant can be determined from the real part of the dielectric function, which is the value of the real part of the dielectric function that corresponds to zero energy. This value equals ≈ 7.5 .

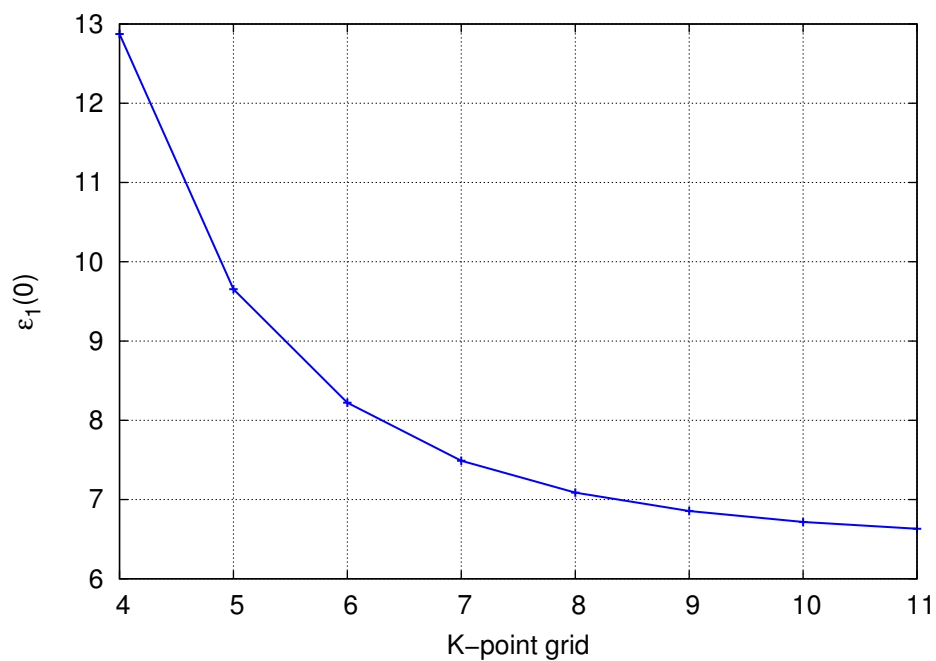


Figure 5.18: The converged test of the static dielectric constant with respect to k-point grids for $\alpha - CH_3NH_3PbI_3$.

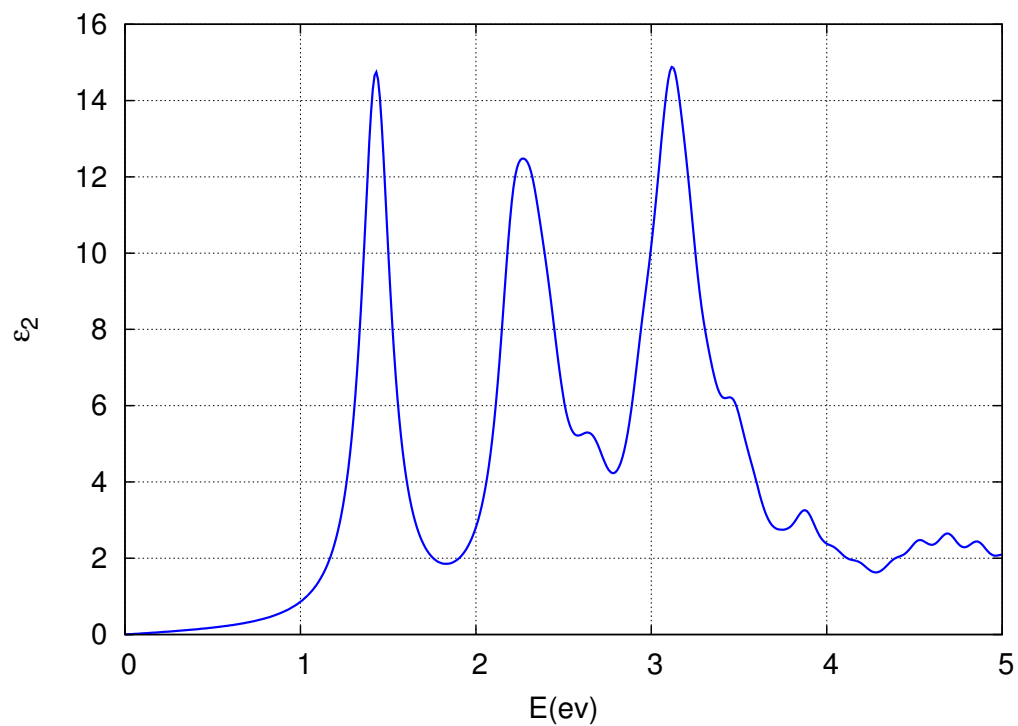


Figure 5.19: Absorption spectrum of $\alpha - CH_3NH_3PbI_3$.

5.2.6 Exciton analysis

Bethe-Salpeter approach.

The first peak in the spectrum Fig.(5.19) represents the bound exciton. The energy corresponding to this peak represents the energy required to create this exciton E_{exc} . The most accurate way to find the exciton is by looking for the highest strength of the excitons in the first peak region, which can be determined from the Fig.(5.20). The exciton energy with the highest strength

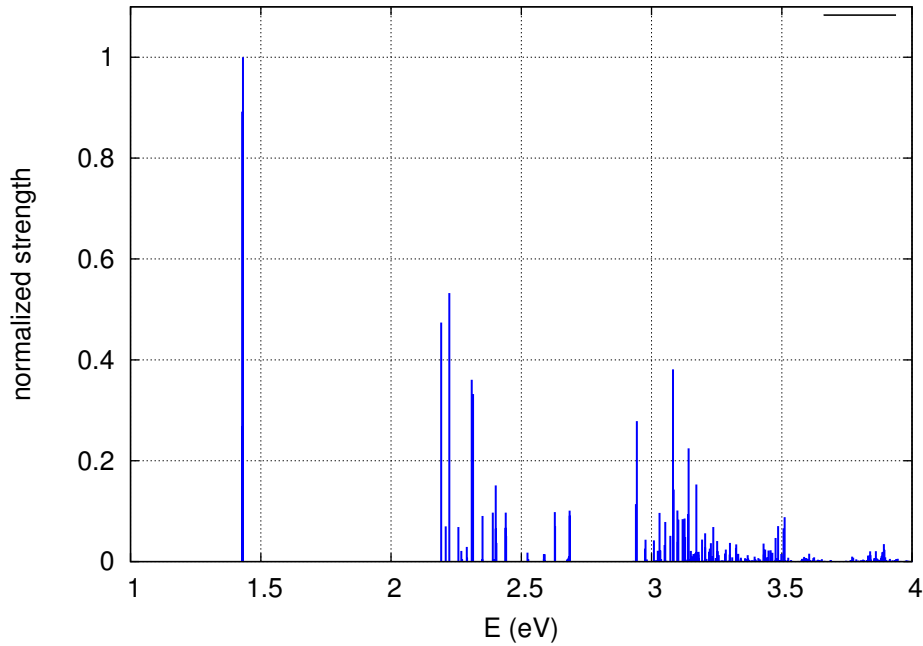


Figure 5.20: The strength of the excitons in energy range from 0 to 4 eV.

in the first peak has 1.433 eV. Then we can calculate the exciton binding energy as follows

$$E_B = E_g - E_{exc} = 1.55 - 1.433 = 0.117 \text{ eV} = 117 \text{ meV}$$

The experimental value of the exciton binding energy for 3D Perovskite is reported in the range of 19-50 meV. All the experimental evidence shows that getting the exciton binding energy in an accurate estimation is challenging due to its dependence on the temperature and the intensity of the excitations i.e light intensity [94].

Exciton transitions.

For the transition states that are involved in the excitation for the highest strength exciton in the first peak region. The data that stated in the table (5.5) shows the transitions of single particle states to the excitation states. We can see that the highest transition probability between band 80 and band 82, which is for the heavy hole exciton and for the light hole exciton between band 79 and band 89. These transitions happen at the A point.

Exciton Wave function

Fig.(5.21) shows the exciton wavefunction of an electron with respect to the fixed hole position, which is fixed at the location of Pb atom. The exciton wavefunction shows that the electronic properties of this perovskite, which is shown in Fig.(5.21), is dominated by the Pb and I ions. Fig.(5.22) shows the electron wavefunction of band 82 at point A , at which the electron part of

Table 5.5: The transition states involved in the excitation at A k-point

k-point -0.5 -0.5 -0.5		
Valence band	Conduction band	Weight
79	82	0.98429
80	81	0.98421
80	82	0.98417
79	81	0.98408

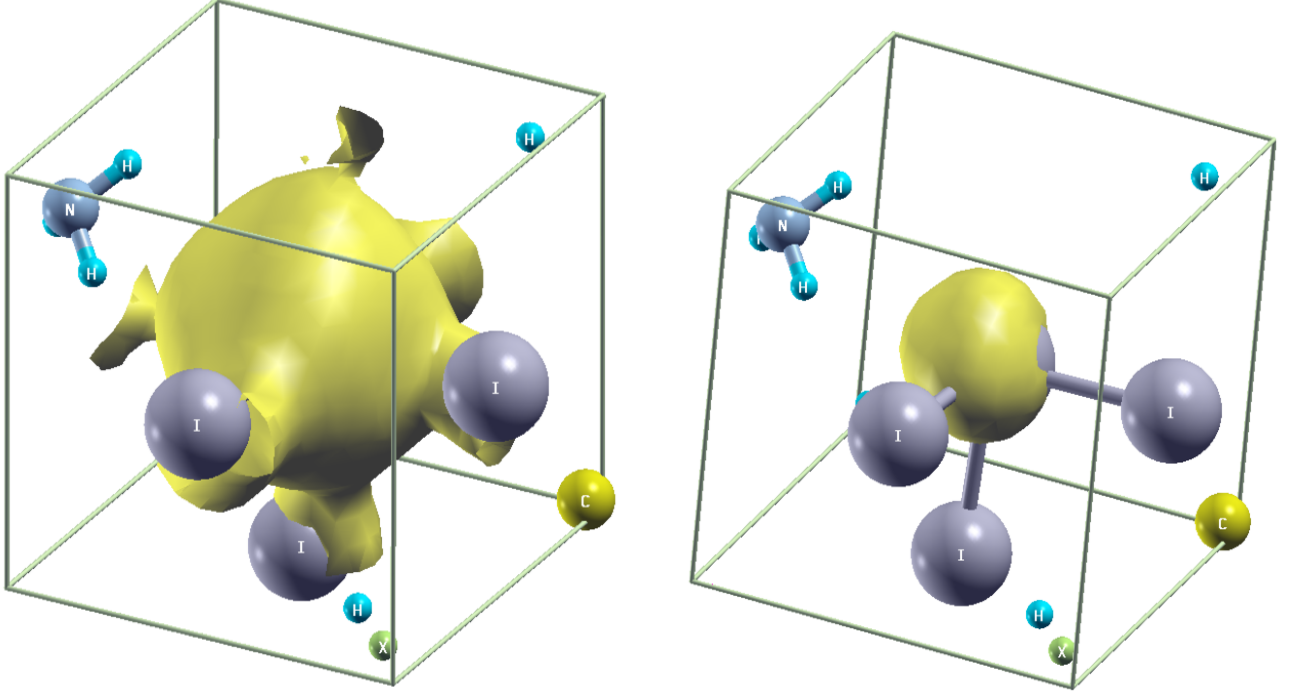


Figure 5.21: Exciton wave function of $\alpha - CH_3NH_3PbI_3$ in three dimensions with different isovalues of the isosurface. The figure on the left has 90% of the maximum value of the isosurface and the figure on the right has 40% of the maximum value of the isosurface.

the exciton is located. The electron wavefunction has the same behaviour as in Fig.(5.21) for the exciton wavefunction. These results show that the electronic properties of $\alpha - CH_3NH_3PbI_3$ are dominated by the Pb and I ions, and the cation CH_3NH_3 does not contribute to the electronic properties, as confirmed in [94]. Although hybrid perovskite devices exhibit high power convergence efficiency, the probability of using them for long term use is low because of their unstable nature and their devolution in ambient environment. This leads to a reduction in the performance within short time of exposure to the ambient environment. The stability problem in the perovskite materials (ABX_3) is due to the size of the cation A [94] (in our case CH_3NH_3).

Wannier approach.

In this approach, we aim to determine the dipole matrix element, which is a key numerical property for the calculation of transition rates. We have discussed in detail how to calculate the dipole matrix element in chapter (4), Sec.(4.3.1). We follow the same procedure for calculating the exciton properties and the dipole matrix elements for GaAs in Sec.(5.1.6).

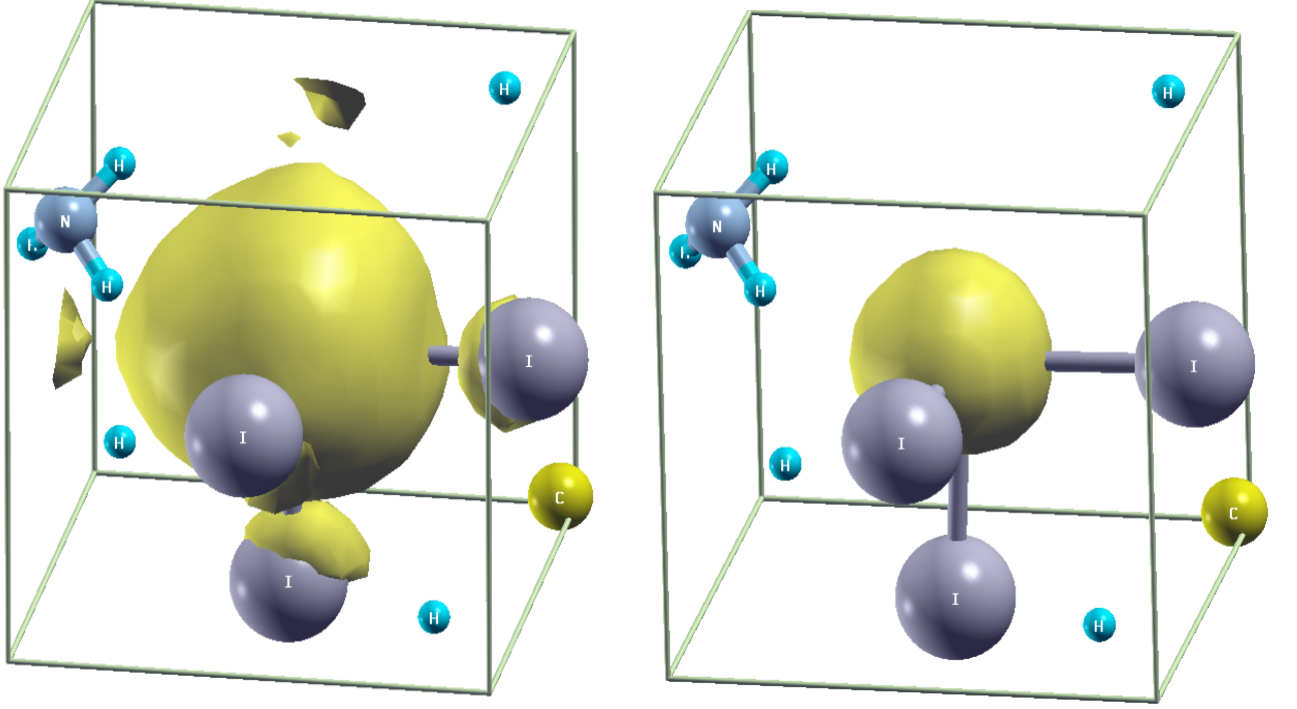


Figure 5.22: Electron wave function of $\alpha - CH_3NH_3PbI_3$ of band 82 at k-point A, at which the electron part of the exciton is located. We used different isovalues of the isosurface. The figure on the left has 90% from the maximum value of the isosurface and the figure on the right has 40% from the maximum value of the isosurface.

The exciton binding energy with the orbital quantum number $n = 1$ is

$$E_B = \frac{\mu}{m_0 \epsilon_r(0)^2} E_{Ry} = 26 \text{ meV}. \quad (5.13)$$

where $\epsilon_r(0) = 6.7$ is the static dielectric function, see Fig.(B.1). The value of the exciton binding energy for 3D perovskites is reported in the range of 19 - 50 meV by using Time-resolved photoluminescence technique [94]. If you look at the values of the exciton binding energy that we have obtained for $\alpha - CH_3NH_3PbI_3$ using the Wannier approach and BSE approach. We find that, up to a numerical level used for estimating the exciton energy and exciton binding energy, the Wannier approach tends to be more reliable than BSE approach. From knowledge of the value of the exciton binding energy, we can estimate the highest temperature, at which the exciton can be observed before it is ripped apart. The thermal energy that is required to rip the exciton apart is $E_B \approx k_B T$, where $E_B = 26 \text{ meV}$. We expect that the exciton will be unstable above $\approx 301 \text{ K}$.

The exciton energy, which is required to create an exciton from the ground state to the 1st exciton state

$$E_{ex} = E_g - E_B = 1.55(\text{eV}) - 26(\text{meV}) = 1.524 \text{ eV}, \quad (5.14)$$

where $E_g = 1.55 \text{ eV}$ is the energy gap, we have calculated in Sec.(5.2.2).

The exciton radius with the orbital $n = 1$,

$$r_{exc} = \frac{m_0}{\mu} \epsilon_r(0) n^2 r_{Ry} = 78 r_{Ry} \approx 4.12 \text{ nm}. \quad (5.15)$$

From the value of the exciton radius , we can estimate how large or small this exciton is by comparing its volume with the unit cell volume. The volume of $\alpha - CH_3NH_3PbI_3$, which has a tetragonal bravais lattice with unit cell dimensions $a = b = 0.631$ nm, and $c = 0.6316$ nm is 2.52×10^{-28} m³. The volume occupied by the exciton with radius $r_{exc} \approx 4.12$ nm is 2.93×10^{-25} m³. From this we deduce that the exciton volume covers ≈ 1162 unit cells.

In order to calculate the transition dipole moment, we have to calculate the following :

- The probability of the relative wave function for e-h pair at zero separation

$$|\phi_n(0)|^2 = \frac{1}{\pi(r_{exc})^3 n^3} = 4.55 \times 10^{24} \text{ m}^{-3}. \quad (5.16)$$

- The dipole matrix element from the $\mathbf{k} \cdot \mathbf{p}$ method

$$\left(\frac{m_0}{m^*}\right)_{ij} = \delta_{ij} + \frac{2}{m_0} \sum_{\mathbf{k}} \frac{|\langle v\mathbf{k}|\mathbf{p}|\mathbf{c}\mathbf{k}\rangle|^2}{E_g}, \quad (5.17)$$

$$|\langle v\mathbf{k}|\mathbf{p}|\mathbf{c}\mathbf{k}\rangle|^2 = 7 \times 10^{-49} (\text{Kg.m.s}^{-1})^2.$$

- The matrix elements of the position vector, which determines from the matrix element of the momentum operator

$$|\langle v\mathbf{k}|\hat{\mathbf{e}} \cdot \mathbf{r}|\mathbf{c}\mathbf{k}\rangle|^2 = \frac{1}{m_0^2 \omega^2} |\langle v\mathbf{k}|\hat{\mathbf{e}} \cdot \mathbf{p}|\mathbf{c}\mathbf{k}\rangle|^2 = 1.5 \times 10^{-19} \text{ m}^2. \quad (5.18)$$

- Transition dipole matrix in the Wannier approach, which is represented in Eq.(4.45)

$$\sum_{\mathbf{k}} |\langle v\mathbf{k}|\hat{\mathbf{e}} \cdot \mathbf{r}|\mathbf{c}\mathbf{k}\rangle|^2 \approx V_{exc} \cdot |\phi_n(0)|^2 |\langle v\mathbf{k}_0|\hat{\mathbf{e}} \cdot \mathbf{r}|\mathbf{c}\mathbf{k}_0\rangle|^2 = (2.9 \times 10^{-25}) \times (4.5 \times 10^{24}) \times (1.5 \times 10^{-19}), \quad (5.19)$$

$$\sum_{\mathbf{k}} |\langle v\mathbf{k}|\hat{\mathbf{e}} \cdot \mathbf{r}|\mathbf{c}\mathbf{k}\rangle|^2 = 2 \times 10^{-19} \text{ m}^2.$$

The relation between the transition rate and the dipole matrix elements is discussed in detail in Sec.(4.3.2). The transition rate is directly proportional to the dipole matrix elements

$$\gamma_i^f \propto V_{exc} \cdot |\phi_n(0)|^2 \cdot |\langle v\mathbf{k}_0|\hat{\mathbf{e}} \cdot \mathbf{r}|\mathbf{c}\mathbf{k}_0\rangle|^2, \quad (5.20)$$

where $V_{exc} = \frac{4\pi}{3}(r_{exc})^3 = 2.93 \times 10^{-25}$ m³. The lifetime is the reciprocal of the transition rate.

Chapter 6

Summary and Discussion

This chapter is a summary and reviews the objective of this work, the methodology used, the results of this work, and concludes with some future work.

6.1 Summary and conclusion

The objective of this research is to propose a general theoretical framework to determine the radiative lifetime of excitons and the optical properties of 3D hybrid perovskites $CH_3NH_3PbI_3$ and to carry out numerical studies of the material properties involved. The reason for studying the radiative lifetime of excitons is to understand the nature of the optical excitation as it has strong impact on the efficiency of photovoltaic cells. The 3D hybrid perovskites $CH_3NH_3PbI_3$ are chosen because they are found to possess very high electron and hole mobility and this family has been suggested as a new class of hybrid photovoltaic semiconductor [3][5]. The ability to calculate the optical properties and the radiative lifetime of excitons on the basis of numerical data using efficient numerical techniques allows for the efficiency of the solar cell to be estimated. This allows for the best candidate materials for solar cells to be identified.

Numerical research was performed in this study, beginning with GaAs as a reference system and then 3D hybrid perovskite $\alpha - CH_3NH_3PbI_3$. The numerical study is based on two tools. The first one is based on the Density Functional Theory (DFT) for ground state calculations and structure optimization, which is included in the Quantum Espresso code. The second is based on the Many-body perturbation theory for calculating the quasiparticles, the optical properties, and obtaining the electron-hole wavefunctions and the exciton properties, which are based on the Bethe-Salpeter equation (BSE). These are included in the Yambo code. The following accomplishment for both GaAs and $\alpha - CH_3NH_3PbI_3$ have been made in this work.

6.1.1 Basic Calculations

- The crystal structure, the calculated band structure using DFT and the corrected band gap using GW calculation have been done. The corrected band gap and the band structure were comparable to the literature. The only problem encountered is the limitation of the k-point grids that we have used.
- The electrons and holes effective masses have been obtained and their results are comparable to the literature.
- The convergence study of the static dielectric constant with respect to the k-point grids shows the necessity of this study for the static dielectric constant calculation. Its converged results are comparable to the literature.

- Calculate the absorption spectrum using different theories, such as the Independent-particle Random phase approximation (IP-RPA), RPA with local field effect (LF), and BSE. RPA with LF showed some differences in the spectrum when compared with IP-RPA and that is due to inclusion of the LF, which is related to the dipole oscillation induced by the external potential. The absorption spectrum between the BSE level and IP-RPA using GW eigenvalues showed discrepancies and disagreement. This is because the electronic correlation response function does not include electron-hole interactions. The BSE includes the electron-hole interaction by relating the response function with the two particle Green's function for the electron and hole.

6.1.2 Exciton analysis

For the exciton analysis, we used two approaches. The first one is the BSE to obtain the electron-hole wavefunctions, exciton energy, and its binding energy. The second is the Wannier approach to obtain the exciton radius, exciton binding energy, and exciton energy :

- For the exciton properties, the Wannier approach tends to be more reliable than the BSE approach up to a numerical level used for estimating the exciton energy and exciton binding energy.
- The exciton wave function and the electron part of the exciton wavefunction obtained from BSE showed that the electronic properties that are contributed by certain atoms are the same as those reported in the literature.

6.1.3 The theoretical framework for calculating the radiative lifetime of the excitons

In the transition rate formula based on Fermi's golden rule in Eq.(4.22), the radiative lifetimes of the excitons can be calculated in two ways :

- Using the exciton eigenstates from the solution of the BSE and applying them to Fermi's Golden rule to describe the theoretical framework for transition rate and exciton lifetimes.
- Calculating the dipole matrix elements, which are functions of the effective mass of electron and hole pairs and the electronic band gap. This matrix is proportional to the transition rates, and inverse proportional to the lifetimes.

We were able to calculate the dipole matrix elements by using the second approach, the values obtained agree with the literature values. For the first approach, the results did not deliver adequate correspondence to the literature. More work is required for better agreement.

6.2 Future work

Current work has a number of open questions, which are left. These questions are needed to be answered in the future :

- Attempting to determine the missing details required to calculate the transition rate by using BSE as a primary technique.
- Giving a theoretical framework to determine other exciton properties such as the drift velocity, the diffusion rate, annihilation rate, etc.

Appendix A

Many-body perturbation theory and Bethe-Salpeter equation implementation.

In this Appendix, we are going to mention in detail the way and the process of how the Yambo code works in terms of computational and theoretical side [6]. This Appendix is based on the Yambo documentation and follows on from the discussion of Chapter (3). In this Appendix a lot of information is repeated to deliver a complete picture.

First of all, Yambo code allows us to calculate :

- Quasiparticles energies within the GW approximation.
- Optical properties at different levels of theory.
- Exciton wavefunctions energy and exciton properties based on the Bethe-Salpeter equation.

Yambo uses the Plasmon Pole Approximation (PPA) for dielectric screening and the norm-conserving pseudopotential. It is a plane wave code, hence all operators and wave functions are expanded as

$$\phi_i(\mathbf{r}) = \sum_{\mathbf{G}}^{N_G} c_i e^{-i\mathbf{G}\cdot\mathbf{r}}$$

where \mathbf{G} is the reciprocal lattice vector. Yambo relies on the Kohn-Sham eigenstates and eigenvalues, that are generated by using PWscf code such as Quantum Espresso package [7], which will be used as input. When Yambo is first run, there are basic operations performed followed by this code, which are called initialization run level. In this level, Yambo does the following

- Set up k-points grids by expanding them to the full BZ and generate momentum transfer vectors $q = \mathbf{k} - \mathbf{k}'$ into a point mesh and then check if the grids are uniform.
- Set up reciprocal lattice grids \mathbf{G} and reorder the reciprocal lattice vectors into spherical shells, where the reciprocal lattice shells are the set of all \mathbf{G} vectors, which are connected by symmetry operations.
- Do some symmetry operations, which act on the \mathbf{G} space and \mathbf{k} space in order to establish the corresponding maps.
- Yambo calculates the Fermi level, the occupations, etc.

Yambo uses 3D complex Fast Fourier Transforms (FFT) to transform the parameters, which are a function of real space \mathbf{r} into the corresponding values in reciprocal space \mathbf{q} , \mathbf{k} and \mathbf{G} and the inverse of FFT to get the transform back again. In optical properties calculation we often don't use the FFT because these calculation will be mostly done at $\mathbf{q} \rightarrow 0$ and $\mathbf{G}, \mathbf{G}' = 0$. The calculations of the excited state levels are very complex tasks and that is because we have a large number of system dependent parameters. At each stage of the calculation we should modify these parameters until they converge before doing our main calculation, as we did in the DFT calculation stage, see Sec.(2.6, 2.5) and appendix (B).

Now we are going to describe the calculation in Yambo in more detail. It is divided into two main part

- a) The GW approximation and quasiparticle (QP) corrections.
- b) The Bethe Salpeter equation (BSE) and the solution of the BS matrix.

A.0.1 GWA and QP corrections

- a) The starting point will be from the non-interacting electron-hole (e-h) or independent particle Green's function G_0 , recall Eq.(3.12)

$$G_0(\mathbf{r}_1, \mathbf{r}_2, \omega) = 2 \sum_n \sum_{\mathbf{k} \in \text{BZ}} \phi_{n\mathbf{k}}(\mathbf{r}_1) \phi_{n\mathbf{k}}^*(\mathbf{r}_2) \left[\frac{f_{n\mathbf{k}}}{\omega - \epsilon_{n\mathbf{k}} - i\eta} + \frac{1 - f_{n\mathbf{k}}}{\omega - \epsilon_{n\mathbf{k}} + i\eta} \right]$$

The solution can be represented by the KS equation, because the eigenstates of DFT are for the system of independent particles and all particle effects are zero $\Sigma = 0$. In Yambo, we can modify the energy range, the energy steps, at which the energy range is divided into uniform steps and selecting the e-h pairs energy by modifying the representative parameters in the program, which have the symbols *EnRnge*, *ETSteps* and *EhEngy* respectively.

- b) Evaluating the integral that involves the oscillator matrix, which is used for calculating the Polarizability and self-energy. The oscillator matrix is defined as

$$\rho_{nn'}(\mathbf{k}, \mathbf{q}, \mathbf{G}) = \langle n\mathbf{k} | e^{i(\mathbf{q}+\mathbf{G}) \cdot \mathbf{r}} | n'\mathbf{k} - \mathbf{q} \rangle = \sum_{G'} u_{n\mathbf{k}-\mathbf{q}}^\dagger(G') u_{n'\mathbf{k}}(G + G') \quad (\text{A.1})$$

The oscillator matrix is evaluated by transforming the real space product of the two wavefunctions using a Fast Fourier Transform (FFT). The product of the periodic part of the orbitals in the third term of the latter equation is evaluated by using the Fourier component in the \mathbf{G} -sphere with the radius R_{WF} , which has the size of two times the radius of the \mathbf{G} -sphere. This is used for the wavefunctions. Note that a FFT box with a sphere radius of $2 \times R_{WF}$ is enclosed, because we need to avoid distortion and errors in the FFT. In Yambo, the input variables *NGsBlk* specifies the FFT box for the oscillator matrix, this variable increases the computational requirements of the code.

- c) Calculating the exchange self-energy. The exchange self-energy matrix element is defined in Eq.(3.35), recall it

$$\Sigma_{n\mathbf{k}}^x = - \sum_{n'} \int_{\text{BZ}} \frac{d\mathbf{q}}{(2\pi)^3} \sum_G v(\mathbf{q} + \mathbf{G}) |\rho_{nn'}(\mathbf{k}, \mathbf{q}, \mathbf{G})|^2 f_{n'}(\mathbf{k} - \mathbf{q})$$

In Yambo, we can control the summation of the reciprocal space \mathbf{G} by modifying the parameter *EXXRLvcs*. The matrix elements are selected by setting the k-points number and the bands range at each k-point. This is achieved by modifying the parameter

QPKrange. The way of integrating over the BZ in the reciprocal lattice and the problem of the divergence of the Coulomb interaction can be treated with the Random Integration Method (RIM), see [69].

- d) The way of treating the oscillator matrix at the optical limit, at which $G = 0$ and $q \rightarrow 0$ is very important to get accurate optical properties. The oscillator matrix in Eq.(A.1) at the optical limit is defined as

$$\lim_{q \rightarrow 0} \rho_{nn'}(\mathbf{k}, \mathbf{q}, \mathbf{0}) = \lim_{q \rightarrow 0} \langle n, \mathbf{k} - \mathbf{q} | e^{i\mathbf{q} \cdot \mathbf{r}} | n', \mathbf{k} \rangle \approx -i\mathbf{q} \cdot \langle n, \mathbf{k} - \mathbf{q} | \mathbf{r} | n', \mathbf{k} \rangle + O(\mathbf{q}^2) \quad (\text{A.2})$$

The last term in the latter equation is a linear expansion of the oscillator matrix up to the first order of \mathbf{q} . Due to the matrix elements of the position operator being not well defined, the first order of the linear expansion is evaluated by using the following form, for details see [54]

$$\lim_{q \rightarrow 0} \rho_{nn'}(\mathbf{k}, \mathbf{q}, \mathbf{0}) \approx \frac{\langle n, \mathbf{k} | -i\mathbf{q} \cdot \nabla + i\mathbf{q} \cdot [V_{nl}, \mathbf{r}] | n', \mathbf{k} \rangle}{\epsilon_{n'\mathbf{k}} - \epsilon_{n\mathbf{k}}} \quad (\text{A.3})$$

where V_{nl} represents the nonlocal part of the pseudopotential. The two wavefunctions at \mathbf{k} and $\mathbf{k} - \mathbf{q}$ are neglected due to introducing terms that are quadratic in \mathbf{q} . The commutator of the nonlocal part of the pseudopotential is strongly affected by the inverse dielectric matrix. Studying the optical properties at the RPA level and BSE level is required to include the nonlocal part commutator of the pseudopotential.

- e) For calculating the frequency dependent part of the self energy, we are going to use the PPA for calculating the screened interaction W . Let us start with the analytical expression of the frequency dependent self-energy, recall Eq.(3.36)

$$\Sigma^c(n\mathbf{k}) = i \sum_{n'} \int_{\text{BZ}} \frac{dq}{(2\pi)^3} \sum_{\mathbf{G}, \mathbf{G}'} \frac{4\pi}{|\mathbf{q} + \mathbf{G}|^2} \rho_{n,n'}(\mathbf{k}, \mathbf{q}, \mathbf{G}) \rho_{n,n'}^*(\mathbf{k}, \mathbf{q}, \mathbf{G}') \times \\ \int d\omega' G_{n', \mathbf{k}-\mathbf{q}}^0(\omega - \omega') \epsilon_{\mathbf{G}, \mathbf{G}'}^{-1}(\mathbf{q}, \omega')$$

The summation over the reciprocal lattice is modified by parameter *NGsBlk*, the band summation is modified by *GbndRange* and the matrix elements are determined by *QPKrange* (similar to $\Sigma_{n\mathbf{k}}^x$). The later equation will be solved if the integration over the frequency can be simplified and the inverse dielectric function can be defined. We are going to mention in details the method of calculating this. Starting with the formula, which relates $\epsilon_{\mathbf{G}, \mathbf{G}'}^{-1}(\mathbf{q}, \omega)$ to the exact response function, recall Eq.(3.28)

$$\epsilon_{\mathbf{G}, \mathbf{G}'}^{-1}(\mathbf{q}, \omega) = \delta_{\mathbf{G}, \mathbf{G}'} + v(\mathbf{q} + \mathbf{G}) \tilde{\chi}_{\mathbf{G}, \mathbf{G}'}(\mathbf{q}, \omega).$$

By using RPA, which is the first approximation to the response function as discussed in section (3.4.2), recall Eq.(3.24)

$$\tilde{\chi} \approx \chi^0(1, 2) = -iG_0(1, 2)G_0(2, 1^+)$$

The non-interacting response function can be determine by using Eq.(3.36), recall it

$$\chi_{\mathbf{G}, \mathbf{G}'}^0(\mathbf{q}, \omega) = 2 \sum_{nn'} \int_{\text{BZ}} \frac{d\mathbf{k}}{(2\pi)^3} \rho_{n', n\mathbf{k}}^*(\mathbf{q}, \mathbf{G}) \rho_{n', n\mathbf{k}}(\mathbf{q}, \mathbf{G}') f_{n\mathbf{k}-\mathbf{q}}(1 - f_{n'\mathbf{k}})$$

$$\times \left[\frac{1}{\omega + \varepsilon_{n\mathbf{k}-\mathbf{q}} - \varepsilon_{n'\mathbf{k}} + i\eta} - \frac{1}{\omega + \varepsilon_{n'\mathbf{k}-\mathbf{q}} - \varepsilon_{n\mathbf{k}} - i\eta} \right]$$

The size of the response function in reciprocal space is controlled by the parameter *NGsBlkXp*, the band summation is governed by the parameter *BndsRnXp* and we are able to control the number of transferred momenta in the oscillator matrix, at which the response function is calculated by modifying the *QPntsRXp* variable.

If we don't want to include charge oscillations, which is induced the external potential. In other words, doing the calculation without a local field, that will be done by setting the *NGsBlkXp* = 1.

PPA solves $\Sigma_{n\mathbf{k}}^c$ equation by achieving an integration over the frequency by considering only all weight of a single excitation at the plasmon pole frequency, see section (3.4.3), recall Eq.(3.37)

$$\epsilon_{G,G'}^{-1}(q, w) \approx \delta_{\mathbf{G},\mathbf{G}'} + \left[\frac{R_{G,G'}(q)}{\omega - \tilde{\omega}_{G,G'}(q) + i\delta} - \frac{R_{G,G'}(q)}{\omega + \tilde{\omega}_{G,G'}(q) - i\delta} \right]$$

where $\tilde{\omega} = E_{\text{PPA}} \sqrt{\frac{\epsilon_2^{-1}}{\epsilon_1^{-1} - \epsilon_2^{-1}}}$ is the energy and $R = -\frac{\epsilon_1^{-1}\tilde{\omega}}{2}$ is the residual. These parameters are evaluated the dielectric matrix by imposing the PPA model at $w = 0$ frequency and $w = iE_{\text{PPA}}$ plasmon pole frequency [70]

$$\begin{aligned} \epsilon_1^{-1} &= \tilde{\epsilon}^{-1}(0 + i0) = -\frac{2R}{\tilde{\omega}} \\ \epsilon_2^{-1} &= \tilde{\epsilon}^{-1}(iE_{\text{PPA}}) = -\frac{2R\tilde{\omega}}{E_0^2 + \tilde{\omega}^2} \end{aligned}$$

where E_{PPA} is the PPA imaginary energy and considered as a user-defined parameter.

- f) The last step is solving the Dyson equation and then getting the QP's correction, recall Eq.(3.12)

$$G_{n\mathbf{k}}(\omega) = \frac{1}{\omega - \varepsilon_{n\mathbf{k}} - [\Sigma_{n\mathbf{k}}^x + \Sigma_{n\mathbf{k}}^c(\omega) - V_{n\mathbf{k}}^{xc}]}$$

The later equation is the Dyson equation for a semiconductor. we have discussed the method of calculating $\Sigma_{n\mathbf{k}}^x$, $\Sigma_{n\mathbf{k}}^c(\omega)$ and the exchange-correlation matrix element $V_{n\mathbf{k}}^{xc} \equiv \langle n\mathbf{k} | V_{xc}(\mathbf{r}) | n\mathbf{k} \rangle$, which corresponds to the exchange-correlation matrix elements that was used in the ground state calculation. The Dyson equation is solved by using the Newton algorithm, at which the quasiparticles energies of this algorithm are defined by

$$\varepsilon_{n\mathbf{k}}^{QP} = \varepsilon_{n\mathbf{k}} + Z_{n\mathbf{k}} [\Sigma_{n\mathbf{k}}^x + \Sigma_{n\mathbf{k}}^c(\varepsilon_{n\mathbf{k}}) - V_{n\mathbf{k}}^{xc}]$$

where Z is the re-normalization factor. It is defined by :

$$Z_{n\mathbf{k}} \equiv \left[1 - \frac{\partial \Sigma_{n\mathbf{k}}^c(\omega)}{\partial \omega} \Big|_{\omega=\varepsilon_{n\mathbf{k}}} \right]^{-1}$$

The method of calculating the derivative quantity in the latter equation is the finite difference method. For more details, see [61][62][64].

A.0.2 Bethe Salpeter equation (BSE) and the solution of the BS matrix

- a) In the beginning, we should first calculate the static screening because we need it to construct the BSE kernel. Starting with the formula that relates the inverse dielectric function to the exact response function, recall Eq.(3.28)

$$\epsilon_{\mathbf{G},\mathbf{G}'}^{-1}(\mathbf{q}, w) = \delta_{\mathbf{G},\mathbf{G}'} + v(\mathbf{q} + \mathbf{G})\tilde{\chi}_{\mathbf{G},\mathbf{G}'}(\mathbf{q}, \omega).$$

The approximation that is used in this step to evaluate the inverse dielectric function is called the static approximation, at which the screening process has to be instantaneous process, see [71]. This means that the response function, which is used in building the BSE kernel has to be evaluated at $\omega = 0$ and hence we can easily evaluate $\epsilon_{\mathbf{G},\mathbf{G}'}^{-1}(\mathbf{q}, w)$ at $\omega = 0$ as well.

The relation between the non-interacting response function and the exact one is represented in the following equation

$$\tilde{\chi}_{\mathbf{G},\mathbf{G}'}(\mathbf{q}, w) = \left[\delta_{\mathbf{G},\mathbf{G}'} - v(\mathbf{q} + \mathbf{G})\chi_{\mathbf{G},\mathbf{G}'}^0(\mathbf{q}, \omega) \right]^{-1} \chi_{\mathbf{G},\mathbf{G}'}^0(\mathbf{q}, \omega)$$

The non-interacting response function can be determine by using Eq.(3.36), recall it

$$\begin{aligned} \chi_{\mathbf{G},\mathbf{G}'}^0(\mathbf{q}, \omega) &= 2 \sum_{nn'} \int_{\text{BZ}} \frac{d\mathbf{k}}{(2\pi)^3} \rho_{n'\mathbf{k}}^*(\mathbf{q}, \mathbf{G}) \rho_{n'\mathbf{k}}(\mathbf{q}, \mathbf{G}') f_{n\mathbf{k}-\mathbf{q}} (1 - f_{n'\mathbf{k}}) \\ &\times \left[\frac{1}{\omega + \varepsilon_{n\mathbf{k}-\mathbf{q}} - \varepsilon_{n'\mathbf{k}} + i\eta} - \frac{1}{\omega + \varepsilon_{n'\mathbf{k}-\mathbf{q}} - \varepsilon_{n\mathbf{k}} - i\eta} \right] \end{aligned}$$

In the later equation we can control the size of the response function in reciprocal space by the parameter *NGsBlkXs*, the band summation is governed by the parameter *BndsRnXs* and the number of transferred momenta in the oscillator matrix is governed by the *QPntsRXs* parameter.

- b) For solving BSE, let us start with the inverse BSE, because it is easier to deal with, recall Eq.(3.53)

$$L = \left[(L^0)^{-1} - \Xi \right]^{-1}$$

where L^0 is the non-interacting e-h pairs Green's function. The energies in L^0 are for single particle energies and they are by default the Kohn-Sham eigenvalues, but in Yambo we have ability to includes the QP energies (GW eigenvalues). The parameter that is used to include the QP energies is *KfnQPdb*. We can rewrite L in terms of the excitonic Hamiltonian as follows

$$L_{v\mathbf{c}\mathbf{k}, v'\mathbf{c}'\mathbf{k}'} = [H^{exc} - I\omega]_{v\mathbf{c}\mathbf{k}, v'\mathbf{c}'\mathbf{k}'}^{-1} (f_{c'} - f_{v'})$$

where

$$H_{v\mathbf{c}\mathbf{k}, v'\mathbf{c}'\mathbf{k}'}^{exc} = (\varepsilon_{v\mathbf{k}} - \varepsilon_{c'\mathbf{k}'}) \delta_{(v\ v')} \cdot \delta_{(c\ c')} \cdot \delta_{(k\ k')} + (f_{c\mathbf{k}} - f_{v\mathbf{k}}) \left[2\tilde{V}_{v\mathbf{c}\mathbf{k}, v'\mathbf{c}'\mathbf{k}'} - W_{v\mathbf{c}\mathbf{k}, v'\mathbf{c}'\mathbf{k}'} \right]$$

The last part in the latter equations is the Bethe-Salpeter Kernel (BSK), the first part is the unscreened short range exchange interaction

$$\tilde{V}_{v\mathbf{c}\mathbf{k}, v'\mathbf{c}'\mathbf{k}'} = \frac{1}{\Omega N_q} \sum_{\mathbf{G} \neq 0} \rho_{v\mathbf{c}}(\mathbf{k}, \mathbf{q} = 0, \mathbf{G}) \rho_{v'\mathbf{c}'}^*(\mathbf{k}_1, \mathbf{q} = 0, \mathbf{G})$$

The summation over the G components is governed by the parameter $BSENGexx$. This parameter takes into account the local field effects. The second part is the screened coulomb interaction between the e-h pairs

$$W_{v\mathbf{c}\mathbf{k}, v'\mathbf{c}'\mathbf{k}'} = \frac{1}{\Omega N_q} \sum_{\mathbf{G}, \mathbf{G}'} \rho_{v\mathbf{v}'}(\mathbf{k}, \mathbf{q}, \mathbf{G}) \rho_{\mathbf{c}\mathbf{c}'}^*(\mathbf{k}', \mathbf{q}, \mathbf{G}') \epsilon_{\mathbf{G}, \mathbf{G}'}^{-1}(\mathbf{q}, \omega) v(\mathbf{q}, \mathbf{G}')$$

The size of $W_{v\mathbf{c}\mathbf{k}, v'\mathbf{c}'\mathbf{k}'}$ matrix is governed by $BSENGBIK$ parameter. The occupied valence states and the unoccupied conduction states are included in the basis of L and specified in Yambo by $BSEBnads$ and $BSEehEny$ in the BS Hamiltonian. The $BSEBnads$ parameter allows to include the occupied valence states and unoccupied conduction states with all their k-points specified, at which the e-h basis of the BSE kernel Ξ is established. There is ability to impose the limit of e-h energy by modifying $BSEehEny$ parameter.

The equation for the effective two particle of the excitonic system is defined as

$$\sum_{n_3 n_4} (\varepsilon_{n_1\mathbf{k}} - \varepsilon_{n_2\mathbf{k}'}) \delta_{(n_1 n_3)} \cdot \delta_{(n_2 n_4)} \cdot \delta_{(k k')} \quad (A.4)$$

$$+ (f_{n_2\mathbf{k}} - f_{n_1\mathbf{k}}) \left[2\tilde{V}_{n_1n_2\mathbf{k}, n_3n_4\mathbf{k}'} - W_{n_1n_2\mathbf{k}, n_3n_4\mathbf{k}'} \right] A_{\lambda}^{(n_3n_4)} = E_{\lambda} A_{\lambda}^{(n_1n_2)}.$$

Now, we can construct the two particle excitonic Hamiltonian matrix, recall Eq.(3.57)

$$H_{(vc),(v'c')}^{exc} = \begin{pmatrix} H_{(vc),(v'c')}^{exc,res} & H_{(vc),(c'v')}^{coupling} \\ - \left[H_{(vc),(c'v')}^{coupling} \right]^* & - \left[H_{(vc),(v'c')}^{exc,res} \right]^* \end{pmatrix}$$

In the excitonic Hamiltonian, we have the resonant part, which includes the interaction of (v, c) with (v', c') and the coupling part, which describes the interaction of (v, c) with (c', v') . For more details on the excitonic Hamiltonian, see section (3.6). There is a possibility to calculate only the resonant part or the coupling part of the Hamiltonian, we can specify that by using the parameter $BSKmod$.

Once we diagonalize the excitonic Hamiltonian, we obtain the exciton energies as eigenvalues and the exciton wavefunctions as eigenvectors. The next step is evaluating the macroscopic dielectric function. A useful spectral representation [9] to determine L is

$$[H^{exc} - I\omega]^{-1} = \sum_{\lambda, \lambda'} = \frac{|A_{\lambda}\rangle S_{\lambda, \lambda'}^{-1} \langle A_{\lambda'}|}{\omega - E_{\lambda}}, \quad (A.5)$$

where $S_{\lambda, \lambda'} = \langle A_{\lambda} | A_{\lambda'} \rangle$ is the overlap matrix of the excitonic Hamiltonian. Using the eigenvalues $\{E_{\lambda}\}$ and eigenvectors $\{A_{\lambda}\}$ of the excitonic Hamiltonian, we may write the polarizability function in transition space as

$$L_{(n_1, n_2), (n_3, n_4)}(\omega) = \sum_{\lambda, \lambda'} \frac{A_{\lambda}^{(n_1, n_2)} S_{\lambda, \lambda'}^{-1} A_{\lambda'}^{*(n_3, n_4)}}{\omega - E_{\lambda}} (f_{n_4} - f_{n_3}). \quad (A.6)$$

Now, the macroscopic dielectric function can be evaluated by substituting this L into equation (3.50), which defines the macroscopic dielectric function with the optical limit of $\mathbf{G} = \mathbf{G}' = 0$, along an particular \mathbf{q} space. The final form of the macroscopic dielectric function becomes

$$\begin{aligned}
& \epsilon_M(\omega) \\
& = 1 - \lim_{q \rightarrow 0} \left[v_{G=0}(q) \sum_{\lambda\lambda'} \left[\sum_{n_1, n_2} \langle n_1 | e^{-iq \cdot r_1} | n_2 \rangle \frac{A_{\lambda}^{n_1 n_2} S_{\lambda\lambda'}^{-1}}{\omega - E_{\lambda} + i\eta} \sum_{n_3 n_4} \langle n_4 | e^{iq \cdot r_2} | n_3 \rangle A^{*(n_3 n_4)} (f_{n_4} - f_{n_3}) \right] \right], \tag{A.7}
\end{aligned}$$

where the matrix elements $\langle n_1 | e^{-iq \cdot r_1} | n_2 \rangle$ is the dipole operator matrix elements in the transition space. The imaginary constant in the last expression $i\eta$ is added to the frequency ω , which shifts the poles away from the real axis. To this end, the absorption spectrum is the relation between the imaginary part of the macroscopic dielectric function and the energy or frequency.

In a conclusion, the calculation process has been simplified with a flowchart in Fig (3.6), which shows a typical numerical implementation of the BSE.

Appendix B

Convergence test of $\alpha - CH_3NH_3PbI_3$

B.1 Convergence test for system dependent parameters at the ground states calculation

We have two main system dependent parameters for the ground state calculation. These two are the size of the k-point grids and the cut off energy of the plane wave basis set. These parameters are described in Quantum Espresso code [7] with the symbols `ecutwfc` and `k-points`. The following is a complete description of these parameters

B.1.1 Convergence test with respect to cut off energy

The two figures in Fig.(B.1) are the real part ϵ_1 and the imaginary part ϵ_2 of the macroscopic dielectric function with cut off energies 40 Rydberg (Ry), 60 Ry, and 80 Ry, which are approximately equivalent to 544 eV, 816 eV, and 1088.5 eV. For the lower value of cut off energy 40 Ry, the peaks are shifted slightly towards the higher energies for both ϵ_1 and ϵ_2 . The value 60 Ry for the cut off energy shows complete convergence.

B.1.2 Convergence test with respect to k-points

At the first glance, in Fig.(B.2) we realize that the set of k-point grids have different offset values. That is because the band gap of this system is located at k-point $A = (0.5, 0.5, 0.5)$, and that is required to select the k-point grids around A at each different set. In general, k-points dominate the quality of the calculation for ϵ_1 and ϵ_2 . We find the same behaviour as in the Random Phase Approximation (RPA) level for this study and the explanation of those behaviours is delivered in Sec.(5.1.5). The only difference that appears is related to ϵ_2 . In the case of the RPA level, the first peak has the same value of energy at different sets of k-point grids and this value is always the DFT band gap, but in the case of BSE level, the first peak does not correspond to the band gap (in this level quasiparticle band gap), due to the inclusion of e-h interactions. The energy of the first peak also increases with increasing the k-point grids. It is difficult to see these changes from the Fig.(B.2).

B.2 Convergence test for system dependent parameters at the excited states calculation

The parameters we need to converge are divided into two categories : parameters for calculating the static dielectric matrix, and other parameters for building up the BS kernel. These parameters are discussed in appendix (A).

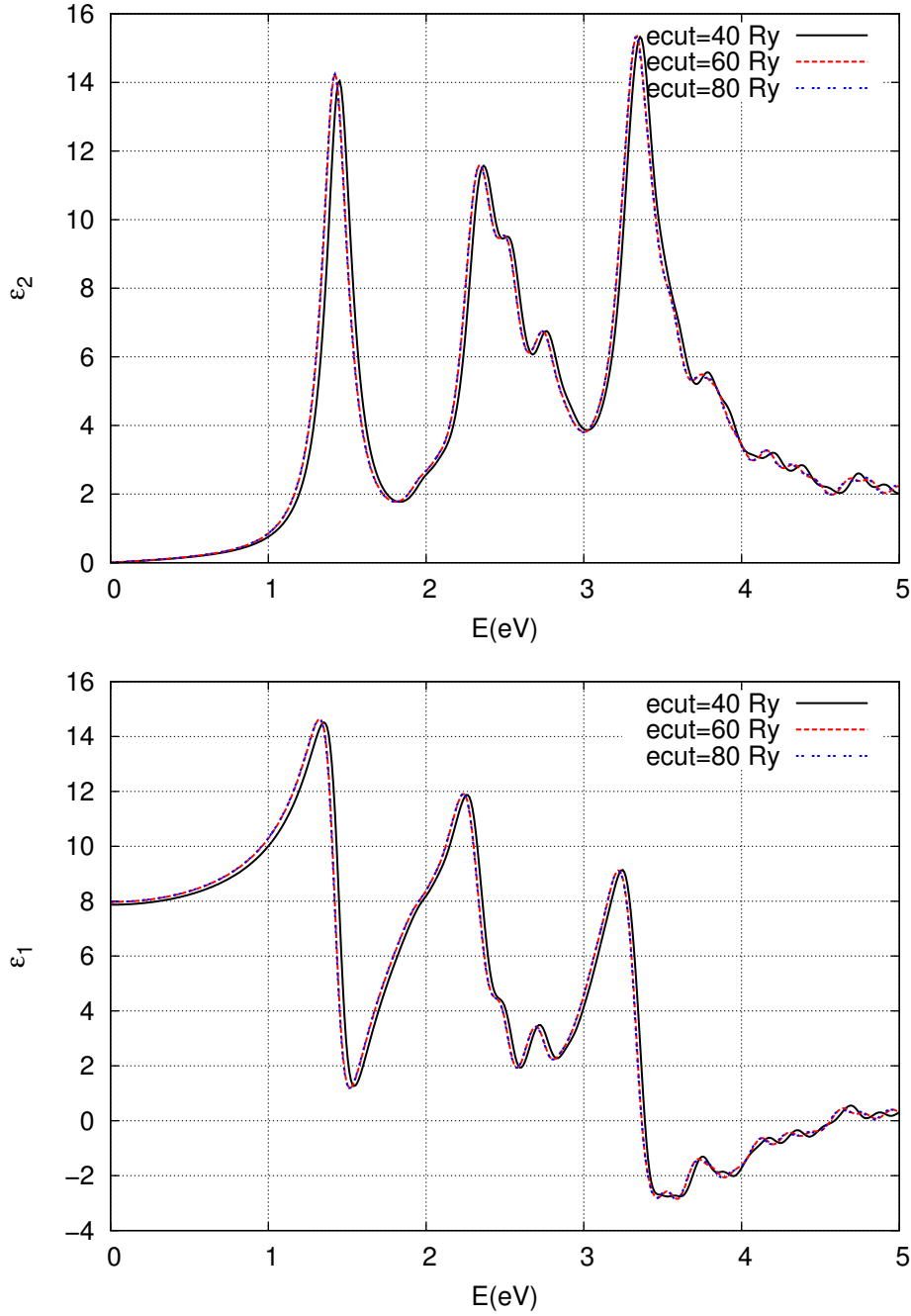


Figure B.1: The real part (ϵ_1) and the imaginary part (ϵ_2) of the macroscopic dielectric function for $\alpha - CH_3NH_3PbI_3$ at k-point grids with dimension $4 \times 4 \times 4$ around Γ and different value of the cut off energy. ϵ_2 is shown at the top, and ϵ_1 is shown at the bottom.

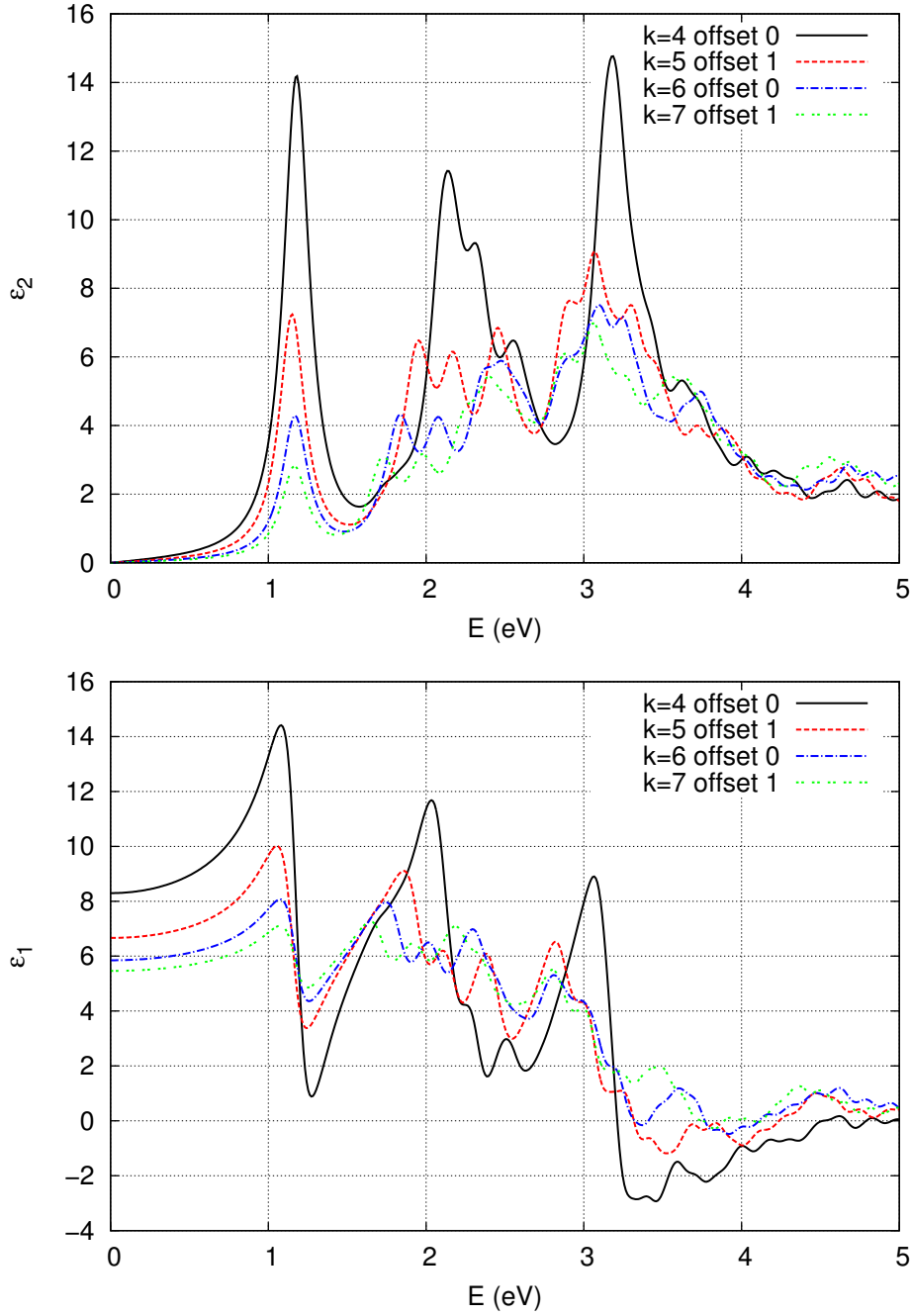


Figure B.2: ϵ_1 and ϵ_2 for $\alpha - CH_3NH_3PbI_3$ at different sets of k-point grids. ϵ_2 is shown at the top, and ϵ_1 is shown at the bottom.

B.2.1 Convergence test for the parameters that are responsible for calculating the static dielectric function

These parameters are described in Yambo code [6] with the symbols BndsRnXs, NGsBlkXs, and QPntsRXs. The following are the complete description of them

- BndsRnXs controls the bands number that are used in the summation of the response function. In Fig.(B.3), ϵ_1 and ϵ_2 are affected by the number of bands that are used in the summation of the response function, which is used in calculating the static dielectric function. The black bold line that represents 80 bands (this number is the number occupied bands in $\alpha - CH_3NH_3PbI_3$) behaves in a totally different way. Based on that, the bands number that are using in this calculation should be greater than the number of occupied bands. BndRnXs parameter in Fig.(B.3) starts to be converged at the band 160.
- NGsBlkXs governs the size of the response function in the reciprocal lattice, which is using in the static dielectric function calculation. Its value in \mathbf{G} vector shells. In Fig.(B.4), ϵ_1 and ϵ_2 are slightly affected by the size of the response function. NGsBlkXs parameter starts to be converged at the value 41 Reciprocal lattice (RL). It is important to notice that the value of NGsBlkXs is in closed RL.
- QPntsRXs is the transferred momenta number in the oscillator matrix, at which the response function is calculated. In Fig.(B.5), ϵ_1 and ϵ_2 are strongly affected by the number of the transferred momenta used through the dielectric function calculation. Its value is limited by the k-points size. In the case of selecting the lower k-point size the QPntsRXs should be equivalent to the total k-point size that using through the calculation.

B.2.2 Convergence test for the parameters that are responsible for establishing BS Kernel.

These parameters are described in Yambo with the symbols BSENGexx, BSENGBlk, and BSEBands. The following is a complete description of these parameters

- BSENGexx controls the summation over \mathbf{G} components in the exchange part of BS kernel $\tilde{\mathbf{V}}$. This parameter takes into account the local field effect. In Fig.(B.6), ϵ_1 and ϵ_2 are slightly affected by the summation over \mathbf{G} components in the exchange part of the BS kernel. The BSENGexx parameter is completely converged at the value 2000 RL.
- BSENGBlk governs the size of the screened coulomb potential matrix $W(\mathbf{G}, \mathbf{G}')$, its \mathbf{G} vectors in a closed vector shells. In Fig.(B.7), ϵ_1 and ϵ_2 are slightly affected by the summation over \mathbf{G} components in the exchange part of BS kernel. The BSENGBlk parameter is completely converged at the value 41 RL. BSENGBlk values must be in RL closed shells like NGsBlkXs parameter. We have noticed during the calculation, the size of the response function during the static dielectric function calculation NGsBlkXs must be greater than or equal to the size of $W(\mathbf{G}, \mathbf{G}')$ matrix BSENGBlk to allow the calculation be proceed.
- BSEBands governs the number of occupied valence states and unoccupied conduction states with their k-points in the basis of L, at which the e-h basis of the BSE kernel and the corresponding the excitonic Hamiltonian are established. In Fig.(B.8), we studied this parameter carefully. Because this parameter is a key parameter for establishing the BS kernel. In the first column in Fig.(B.8) from the left, we fixed the number of occupied states (It is ten bands below the Fermi level) and increasing the number of unoccupied sates by ten states above the Fermi level for three times. We did the same in the second column, where the number of unoccupied bands (It is ten band above the Fermi level) is

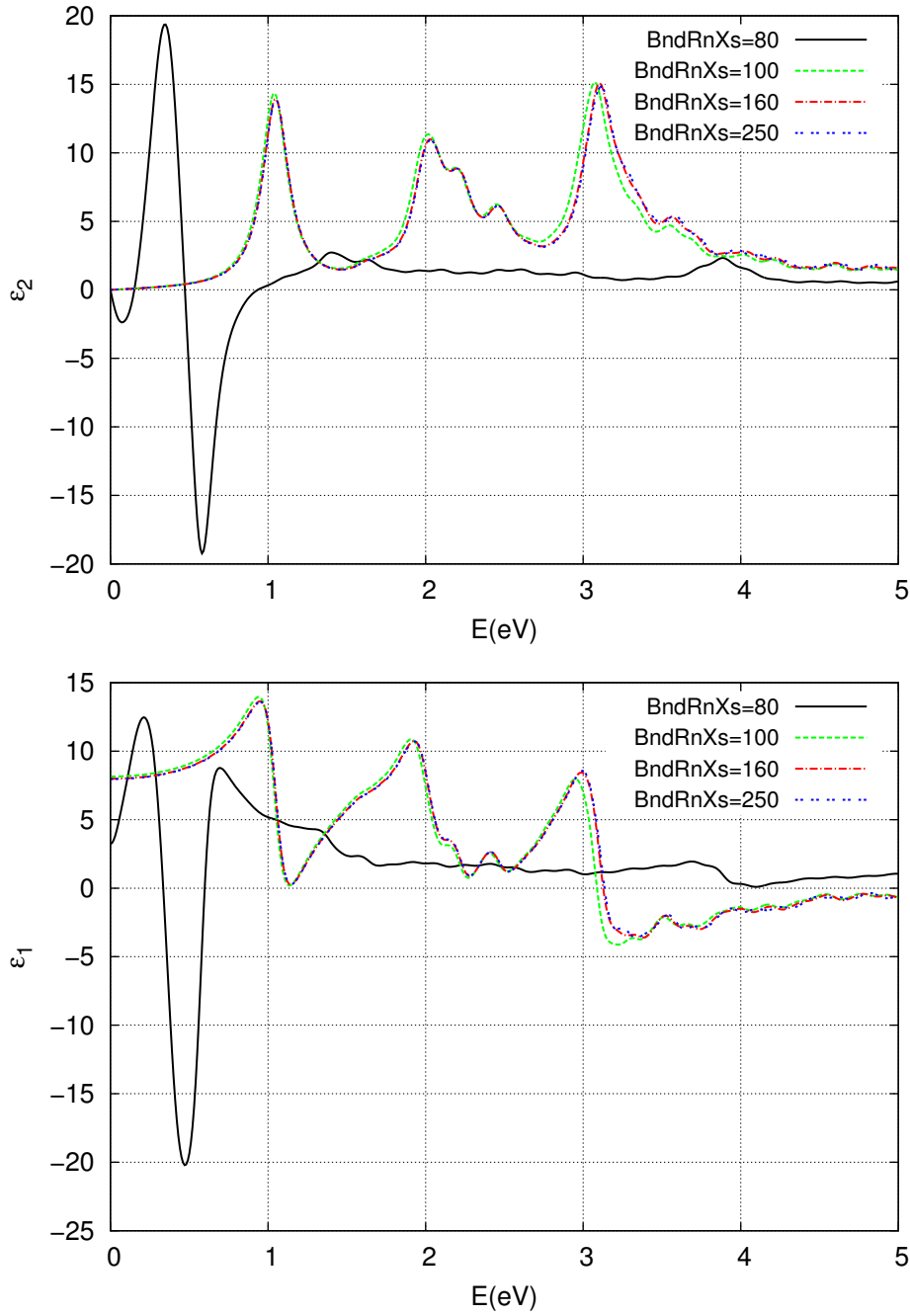


Figure B.3: ϵ_1 and ϵ_2 for $\alpha - CH_3NH_3PbI_3$ at different value of the $BndsRnXs$ parameter. ϵ_2 is shown at the top, and ϵ_1 is shown at the bottom.

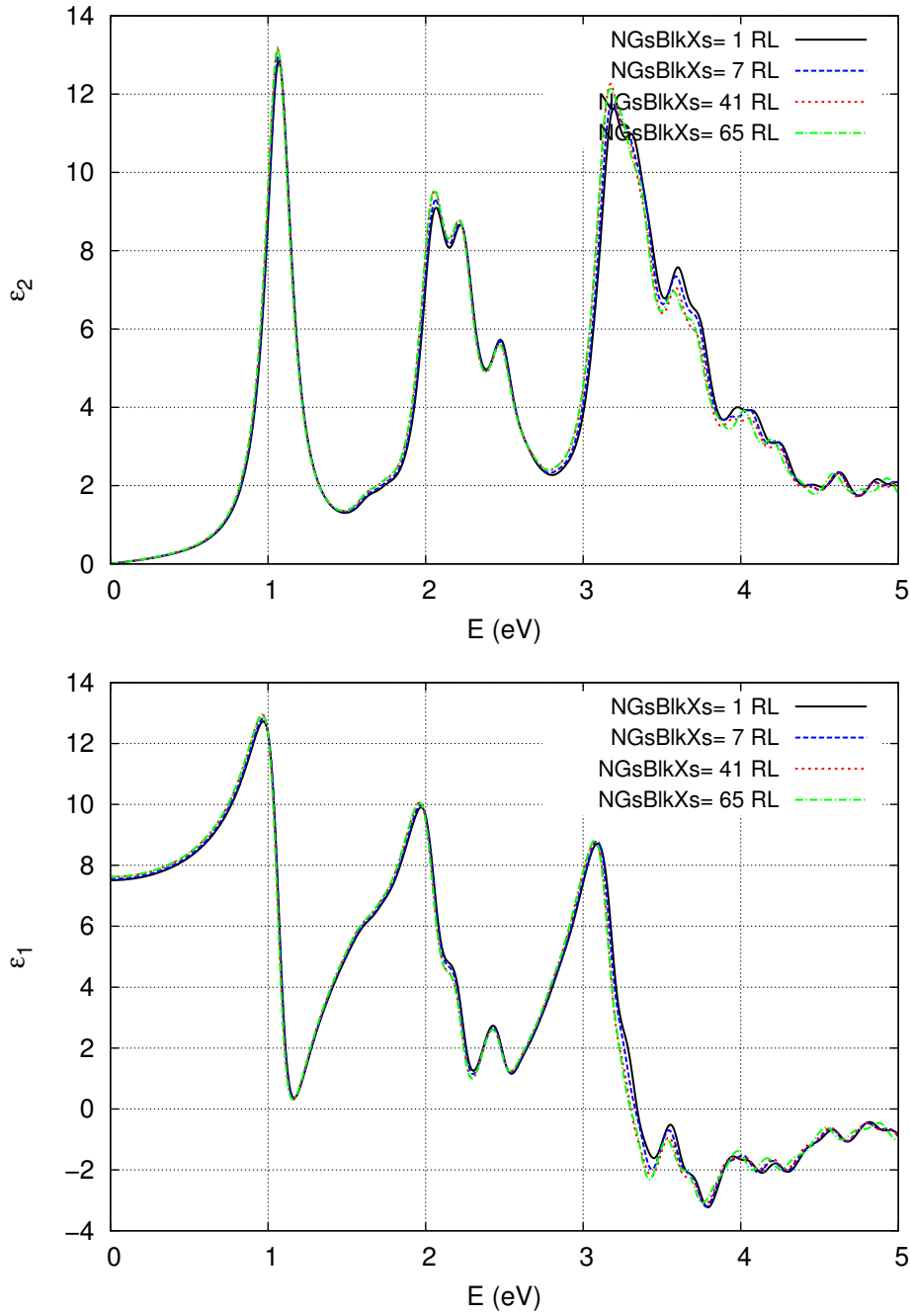


Figure B.4: ϵ_1 and ϵ_2 for $\alpha - CH_3NH_3PbI_3$ at different value of the NGSBlkXs parameter. ϵ_2 is shown at the top, and ϵ_1 is shown at the bottom.

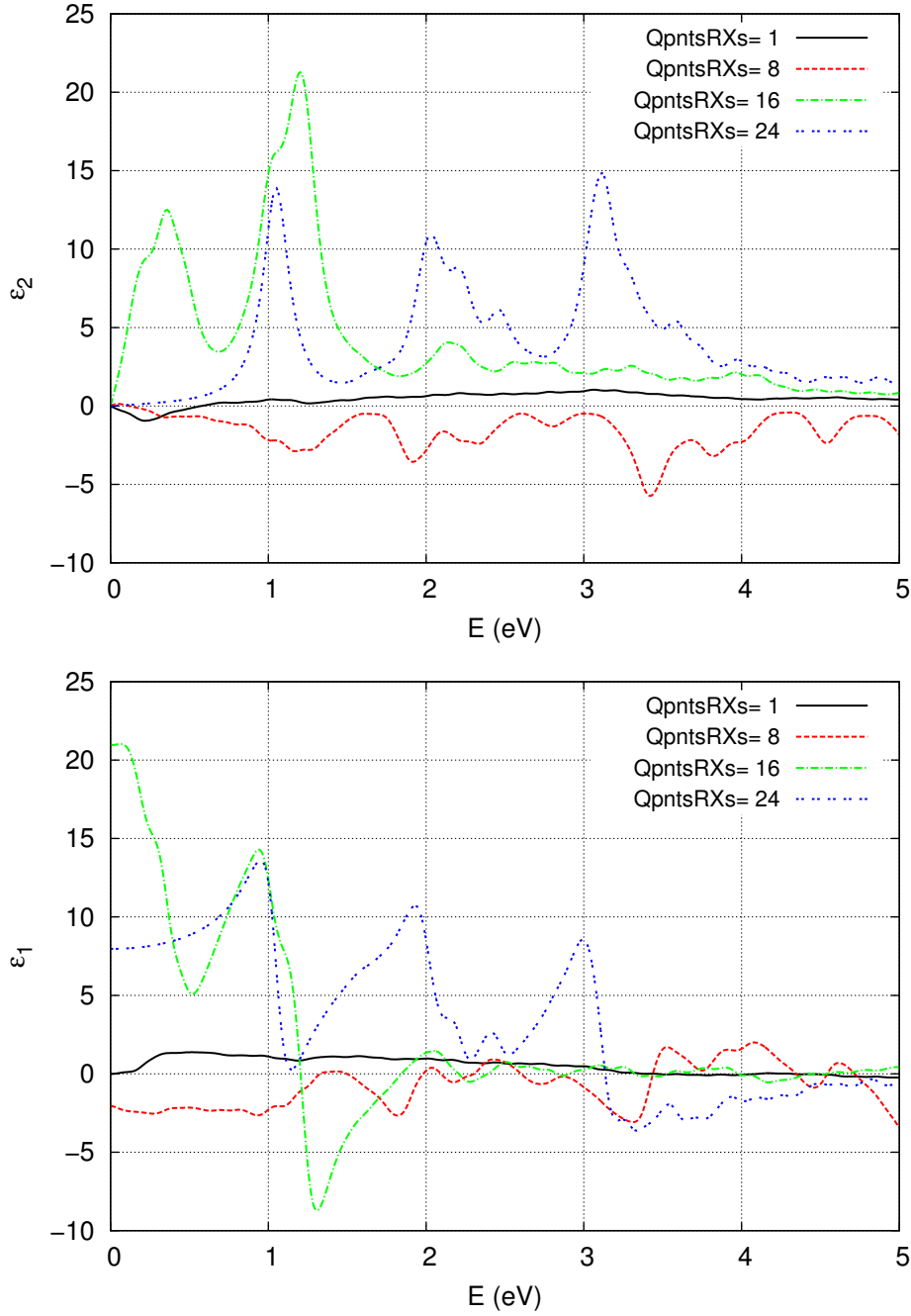


Figure B.5: ϵ_1 and ϵ_2 for $\alpha - CH_3NH_3PbI_3$ at different value of QpntsRXs parameter. ϵ_2 is shown at the top, and ϵ_1 is shown at the bottom.

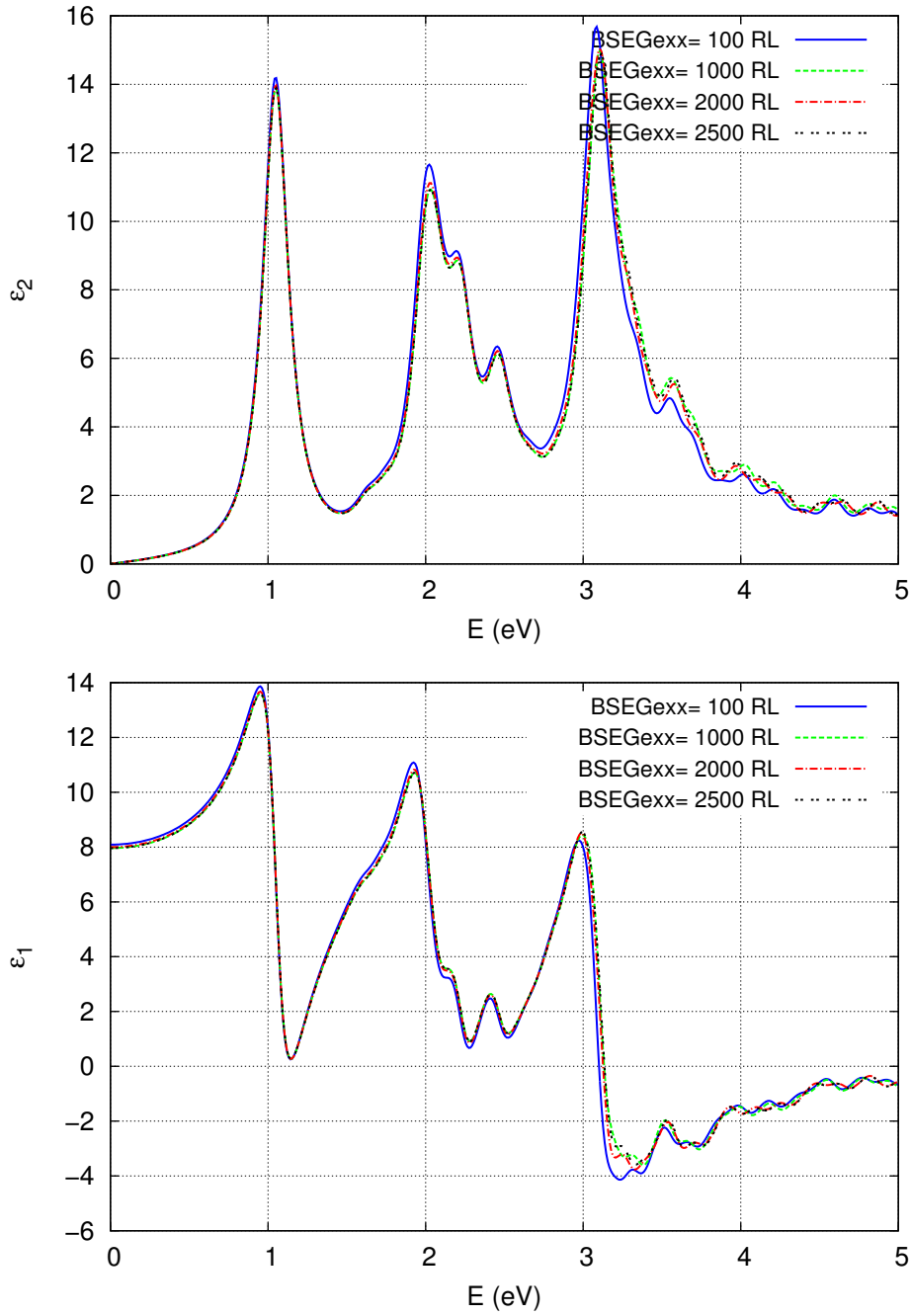


Figure B.6: ϵ_1 and ϵ_2 for $\alpha - CH_3NH_3PbI_3$ at different value of BSEGexx parameter. ϵ_2 is shown at the top, and ϵ_1 is shown at the bottom.

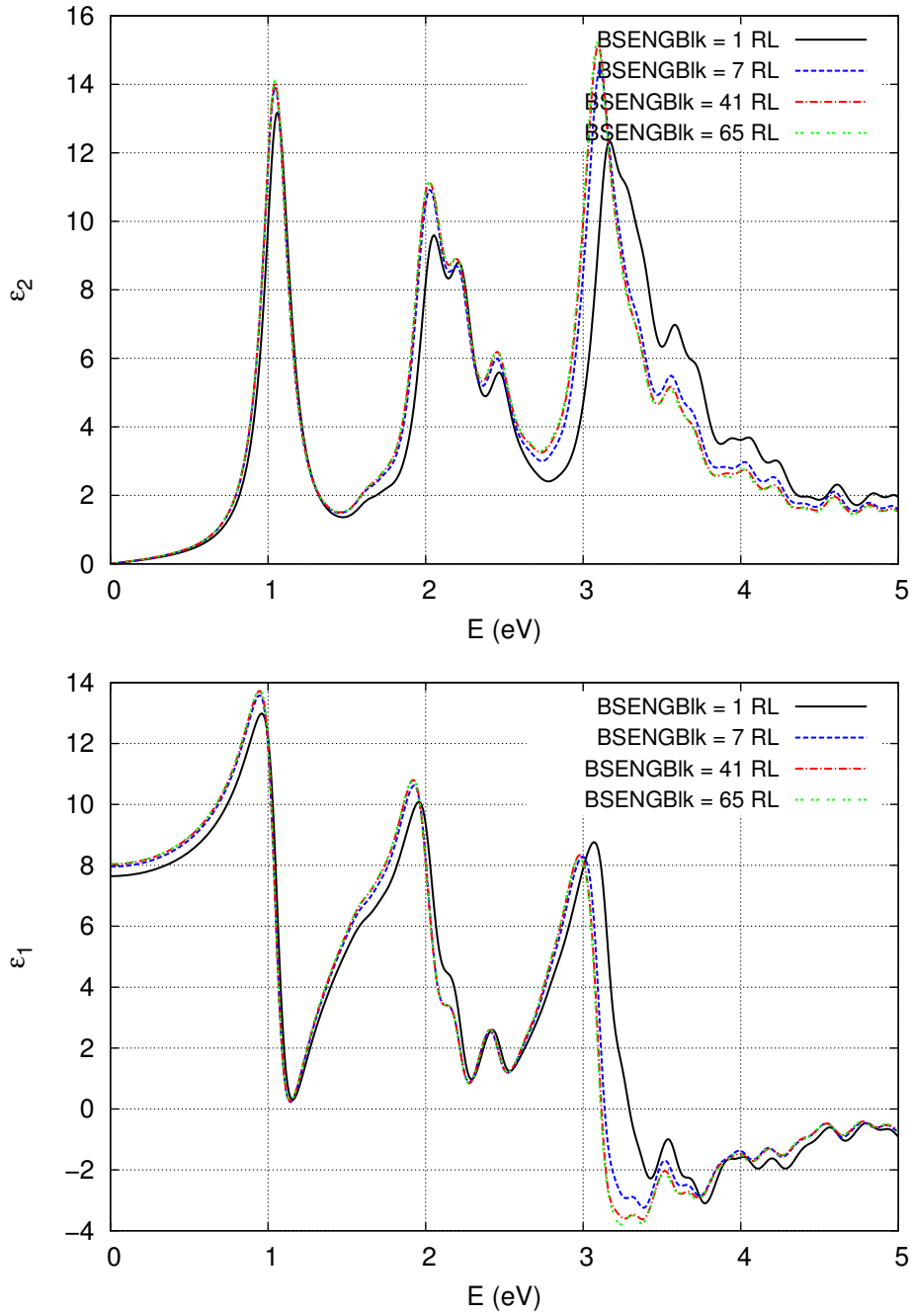


Figure B.7: ϵ_1 and ϵ_2 for $\alpha - CH_3NH_3PbI_3$ at different value of BSENGBlk parameter. ϵ_2 is shown at the top, and ϵ_1 is shown at the bottom.

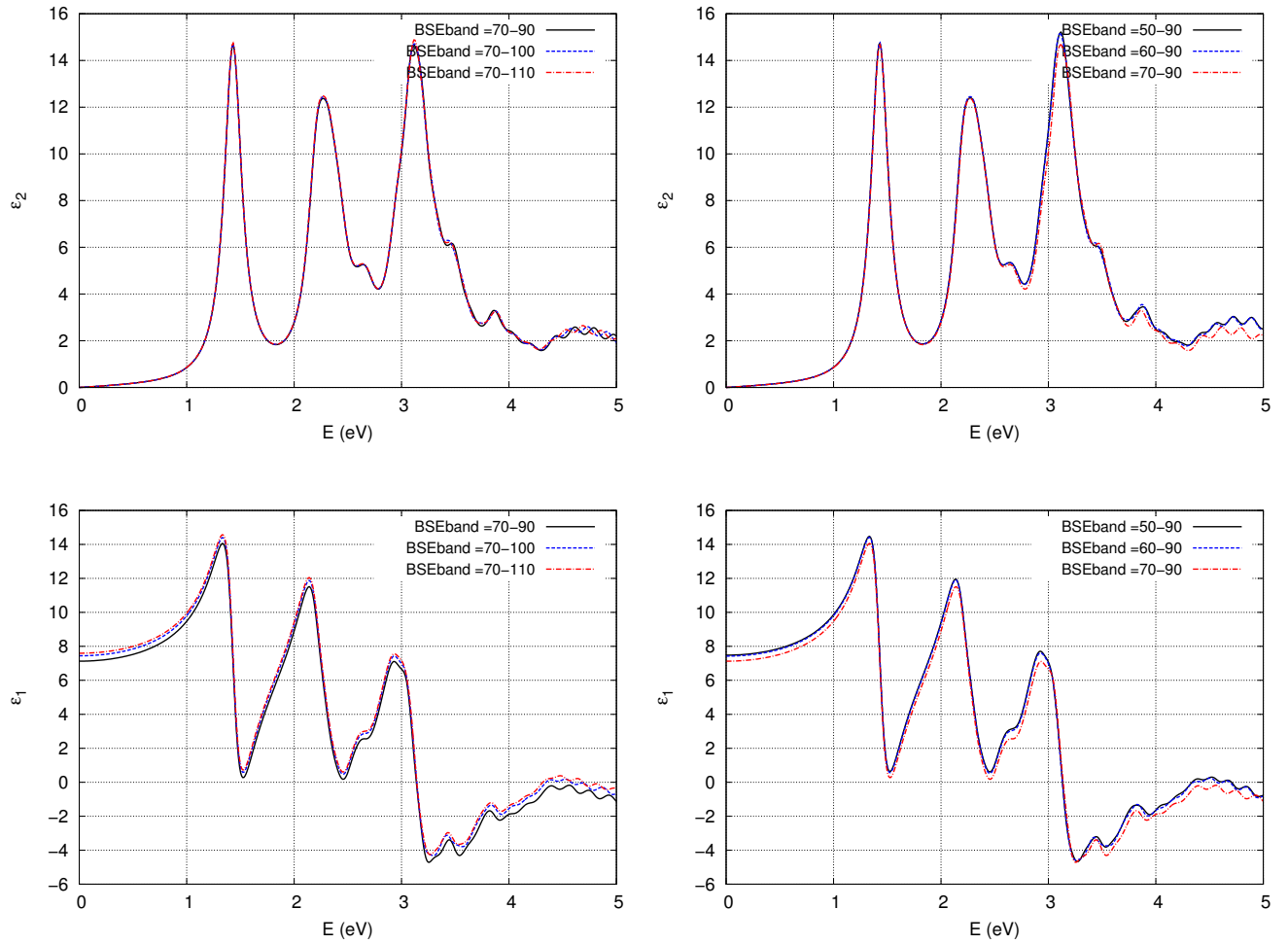


Figure B.8: ϵ_1 and ϵ_2 for $\alpha - CH_3NH_3PbI_3$ at different value of BSEBand parameter. In the first column from the left the number of occupied states is fixed. In the second column the number of unoccupied states is fixed.

fixed and increasing the number of occupied sates by ten states below the Fermi level for three times. ϵ_2 for the two columns does not affect significantly by the large number of occupied and unoccupied states. It is enough to add ten states above and blew the Fermi level, but ϵ_1 for the two columns needs at least 20 states above and below the Fermi level to converge BSEBand parameter. This parameter is an expensive parameter. The higher the value of this parameter is, the more memory is required as well as the more CPU time of the calculation will takes.

There is also the plane wave cut off parameter of the wave functions, where it is used in this stage of the calculation. It represents by the symbol FFTGvecs in Yambo. In Fig.(B.9), the completely converged value is 2000 RL. The lower value of FFTGvecs affects the orthonormalization of the wavefunctions that are used.

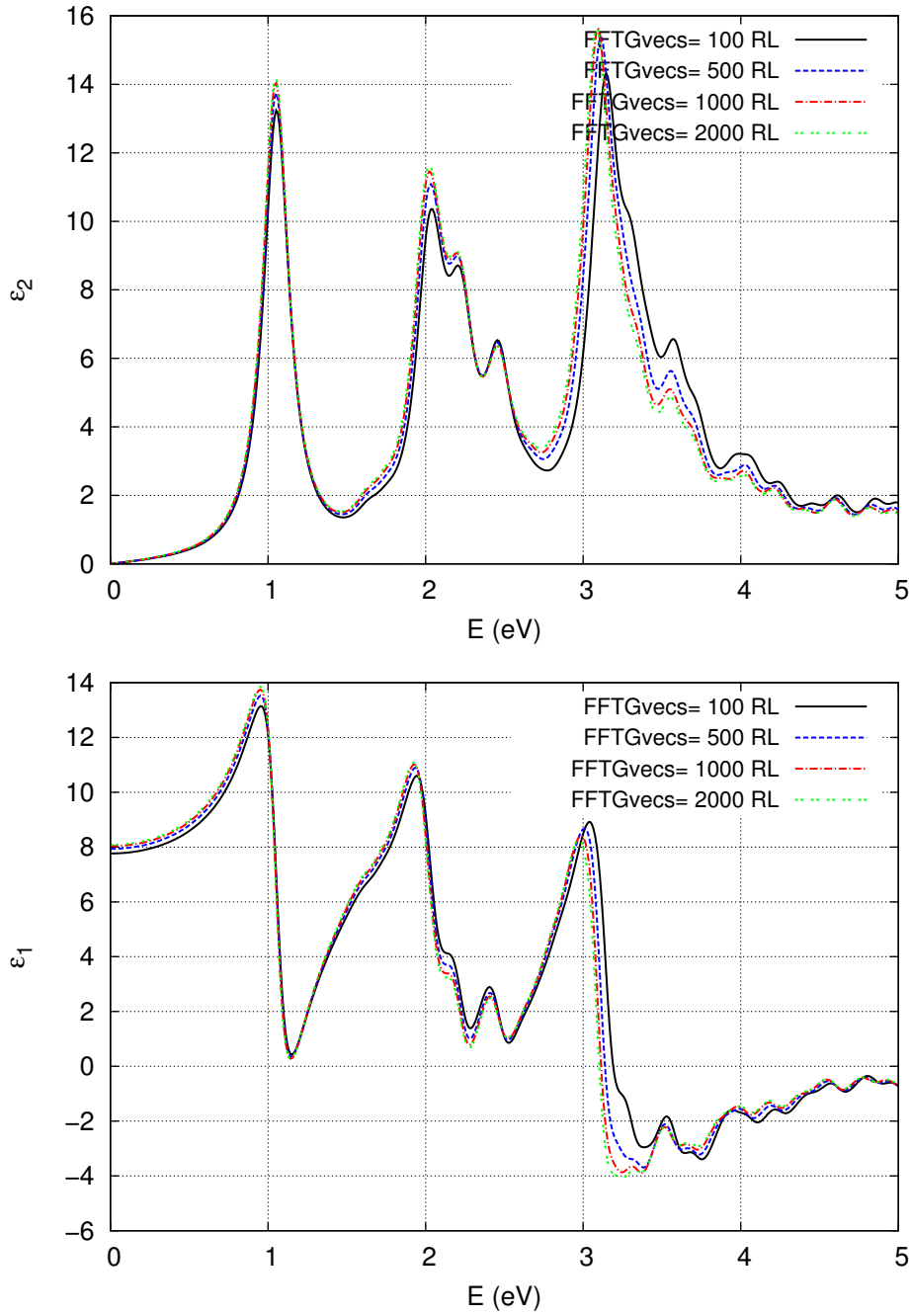


Figure B.9: ϵ_1 and ϵ_2 for $\alpha - CH_3NH_3PbI_3$ at different value of FFTGvecs parameter. ϵ_2 is shown at the top, and ϵ_1 is shown at the bottom.

Appendix C

The relation between the matrix elements of a momentum operator and the matrix elements of a position vector

The Hamiltonian of a single particle

$$H = \frac{p^2}{2m} + V, \quad [V, \mathbf{r}] = 0,$$

The commutation relation between the position \mathbf{r} and the Hamiltonian \mathbf{H} [92] are

$$\begin{aligned} [H, \mathbf{r}] &= \left[\frac{p^2}{2m} + V, \mathbf{r} \right] = \left[\frac{p^2}{2m}, \mathbf{r} \right], \\ [H, \mathbf{r}] &= -i\hbar \frac{\mathbf{P}}{m}. \end{aligned} \tag{C.1}$$

The relation between the momentum operator and the commutator is then Then

$$-\frac{i\hbar}{m} \langle v\mathbf{k} | \mathbf{p} | c\mathbf{k} \rangle = \langle v\mathbf{k} | [H, \mathbf{r}] | c\mathbf{k} \rangle, \tag{C.2}$$

where

$$\langle v\mathbf{k} | [H, \mathbf{r}] | c\mathbf{k} \rangle = \langle v\mathbf{k} | (H\mathbf{r} - \mathbf{r}H) | c\mathbf{k} \rangle,$$

and

$$H|v\mathbf{k}\rangle = E_i|v\mathbf{k}\rangle, \quad H|c\mathbf{k}\rangle = E_f|c\mathbf{k}\rangle,$$

then

$$\langle v\mathbf{k} | (H\mathbf{r} - \mathbf{r}H) | c\mathbf{k} \rangle = (\langle v\mathbf{k} | H) \mathbf{r} | c\mathbf{k} \rangle - \langle v\mathbf{k} | \mathbf{r} (H | c\mathbf{k} \rangle) = (E_i - E_f) \langle v\mathbf{k} | \mathbf{r} | c\mathbf{k} \rangle.$$

applying the last result to Eq.(C.2), we get i.e.

$$\langle v\mathbf{k} | \mathbf{p} | c\mathbf{k} \rangle = \frac{im}{\hbar} (E_i - E_f) \langle v\mathbf{k} | \mathbf{r} | c\mathbf{k} \rangle. \tag{C.3}$$

References

- [1] Dr. Neil Robertson et al. The Solar Spark project, the University of Edinburgh. <http://www.thesolarspark.co.uk/the-science/solar-power/excitonic-solar-cells>. [online; accessed on 2016-03-18].
- [2] Catalin D. Spataru, Sohrab Ismail-Beigi, Rodrigo B. Capaz and Steven G. Louie. Theory and Ab Initio Calculation of Radiative Lifetime of Excitons in Semiconducting Carbon Nanotubes. *Phys. Lett.* 95, 247402 (2005).
- [3] Constantinos C and Kanatzidis. Semiconducting Tin and Lead Iodine Perovskite with Organic Cations. *Inorganic Chemistry*. 52, 9019 (2013).
- [4] Jacky Even, Laurent Pedesseau, Jean-Marc Jancu, and Claudine Katan. DFT and $k \cdot p$ modelling of the phase transitions of lead and tin halide perovskites for photovoltaic cells. *Phys. Status Solidi*. RRL.8, 31 (2014).
- [5] Jacky Even, Laurent Pedesseau, Jean-Marc Jancu, and Claudine Katan. Importance of Spin Orbit Coupling in Hybrid Organic/Inorganic Perovskites for Photovoltaic Applications. *J. Phys. Chem. Lett.* 4, 2999 (2013).
- [6] A. Marini, C. Hogan, M. Grüning, D. Varsano. An ab initio tool for excited state calculations. *Computer Physics Communications*. 180, 1392 (2009).
- [7] Paolo Giannozzi and Stefano Baroni, et al. QUANTUM ESPRESSO: a modular and open-source software project for quantum simulations of materials. *Journal of Physics: Condensed Matter*. 21,39 (2009).
- [8] B. Farid et al. GW approach to the calculation of electron self-energies in semiconductors. *Phys. Rev.* B38, 7530 (1988).
- [9] S. Albrecht. Ecole Polytechnique. *Ph.D. thesis*. Palaiseau, Paris, (1999).
- [10] M.S. Hybertsen and S.G. Louie. Electron correlation in semiconductors and insulators: Band gaps and quasiparticle energies. *Phys. Rev.* B34, 5390 (1986).
- [11] L. Hedin. New Method for Calculating the One particle Green's Function with Application to the Electron Problem. *Phys. Rev.* 139, A796 (1965).
- [12] Roger Haydock and N. W. Ashcroft. Electronic States in Complicated Materials: The Recursion Method. *The Royal Society*. 334, 549 (1991).
- [13] R. M. Martin. Electronic structure: Basic theory and practical methods. Cambridge University Press, Cambridge (2004).
- [14] H. Monkhorst, J. Pack. Special points for Brillouin-zone integrations. *Phys. Rev.* B13, 5188 (1976).

- [15] M. L. Cohen and V. Heine. The fitting of pseudopotentials to experimental data and their subsequent application. *Solid State Physics*. Vol. 24, eds. H. Ehrenreich, F. Seitz, and D. Turnbull, Academic Press, New York, (1970).
- [16] J. Phillips, L. Kleinman. New Method for Calculating Wave Functions in Crystals and Molecules. *Phys. Rev.* 116, 287 (1959).
- [17] G. B. Bachelet, D. R. Hamann, and M. Schlüter. Pseudopotentials that work: From H to Pu. *Phys. Rev.* B26, 4199 (1982).
- [18] N. Troullier and Jose Luis Martins. Efficient pseudopotentials for plane-wave calculations. *Phys. Rev.* B43, 1993 (1991).
- [19] A. Rappe, K. Rabe, E. Kaxiras, J. Joannopoulos. Optimized pseudopotentials. *Phys. Rev.* B41, 1227 (1990).
- [20] L. Kleinman, D. Bylander. Efficacious Form for Model Pseudopotentials. *Phys. Rev. Lett.* 48, 1425 (1982).
- [21] J. Hutter, H. Lúthí, M. Parrinello. Electronic structure optimization in plane-wave-based density functional calculations by direct inversion in the iterative subspace. *Comput. Mater. Sci.* 2, 244 (1994).
- [22] D. Vanderbilt. Soft self-consistent pseudopotentials in a generalized eigenvalue formalism. *Phys. Rev.* B41, 7892 (1990).
- [23] G. Kresse, D. Joubert. From ultrasoft pseudopotentials to the projector augmented-wave method. *Phys. Rev.* B59, 1758 (1999).
- [24] D. Hamann, M. Schluter, C. Chiang. Norm-conserving pseudopotentials. *Phys. Rev. Lett.* 43, 1494 (1979).
- [25] N. Holzwarth, G. Matthews, R. Dunning, A. Tackett, Y. Zeng. Comparison of the projector augmented-wave, pseudopotential, and linearized augmented-plane-wave formalisms for density-functional calculations of solids. *Phys. Rev. Lett.* B55, 2005 (1997).
- [26] P. E. Blöchl. Projector augmented-wave method. *Phys. Rev. Lett.* B50, 17953 (1994).
- [27] M. Gajdoš, K. Hummer, G. Kresse, J. Furthmüller, and F. Bechstedt. Linear optical properties in the projector-augmented wave methodology. *Phys. Rev. Lett.* B73, 045112 (2006).
- [28] N. Wiser. Dielectric Constant with Local Field Effects Included. *Phys. Rev.* 129, 62 (1963).
- [29] G. D. Mahan. *Condensed Matter in a Nutshell*. Princeton University Press, Princeton, (2011).
- [30] M. Born and J. M. Oppenheimer. Quantum theory of the molecules. *Ann. d. Physik.* 84, 457 (1927).
- [31] D. R. Hartree. The wave mechanics of an atom with a non-Coulomb central field. *Proc. Cambridge Philos. Soc.* 24, 89 (1928).
- [32] P. Hohenberg and W. Kohn. Inhomogeneous Electron Gas. *Phys. Rev.* B864, 136 (1964).
- [33] Mel Levy. Universal variational functionals of electron densities, first-order density matrices, and natural spin-orbitals and solution of the v-representability problem. *Proc. Natl. Acad. Sci. USA.* 76, 6062, (1979).

- [34] W. Kohn and L. J. Sham. Self-Consistent Equations Including Exchange and Correlation Effects. *Phys. Rev.* 140, A1133 (1965).
- [35] W. Kohn and L. J. Sham. Self-Consistent Equations Including Exchange and Correlation Effects. *Phys. Rev.* 140, A1133 (1965).
- [36] D. M. Ceperley and B. J. Alder. Ground State of the Electron Gas by a Stochastic Method. *Phys. Rev. Lett.* 45, 566 (1980).
- [37] T. C. Leung, C. T. Chan, B. N. Harmon. Ground-state properties of Fe, Co, Ni, and their monoxides: Results of the generalized gradient approximation. *Phys. Rev.* B44, 2923 (1991).
- [38] P. Rinke, A. Qteish, J. Neugebauer, C. Freysoldt, M. Scheffler. Combining GW calculations with exact-exchange density-functional theory: an analysis of valence-band photoemission for compound semiconductors. *New J. Phys.* 7, 126 (2005).
- [39] Singh, David J., Nordstrom, Lars. Planewaves, Pseudopotentials, and the LAPW Method. Springer, New York, (2006).
- [40] Ozolins V V, Körling M. Full-potential calculations using the generalized gradient approximation: Structural properties of transition metals. *Phys. Rev.* B48, 18304 (1993).
- [41] A. El-Barbary. First principles characterisation of defects in irradiated graphitic materials. *Ph.D. thesis.* University of Sussex (2005).
- [42] E. I. Proynov, E. Ruiz, A. Vela, D. Salahub. Supplement: Proceedings of the International Symposium on Atomic, Molecular, and Condensed Matter Theory and Computational Methods. *Int. J Quantum Chem.* 56, 61 (1995).
- [43] Abrikosov, Gorkov, and Dzyaloshinskii. Methods of Quantum Field Theory in Statistical Physics. Dover, New York, (1975).
- [44] Fetter, and Walecka. Quantum theory of many particle systems. McGrawHill, New York, (1971).
- [45] R.D Mattuck. A guide to Feynman diagrams in the many body problem. Dover, New York, (1992).
- [46] R.D Mattuck. Electronic band structures of molybdenum and tungsten dichalcogenides by the GW approach. *The Journal of Physical Chemistry C.* 116, 7664 (2012).
- [47] V. M. Galitskii and A. B. Migdal. Application of Quantum field theory methods to Many body problem. *Sov. Phys. JETP.* 7, 96 (1958).
- [48] F. J. Dyson. The Radiation Theories of Tomonaga, Schwinger, and Feynman. *Phys. Rev.* 75, 486 (1949).
- [49] F. J. Dyson. The S Matrix in Quantum Electrodynamics. *Phys. Rev.* 75, 1736, (1949).
- [50] M. S. Hybertsen and S. G. Louie. First-principles theory of quasiparticles: Calculation of band gaps in semiconductors and insulators. *Phys. Rev. Lett.* 55, 1418 (1985).
- [51] I. Campillo, J. M. Pitarke, A. Rubio, E. Zarate, and P. M. Echenique. Inelastic Lifetimes of Hot Electrons in Real Metals. *Phys. Rev. Lett.* 83, 2230 (1999).
- [52] C. D. Spataru, M. A. Cazalilla, A. Rubio, L. X. Benedict, P. M. Echenique, and S. G. Louie Anomalous quasiparticle lifetime in graphite: Band structure effects.. *Phys. Rev. Lett.* 87, 246405 (2001).

- [53] L. Hedin and S. Lundqvist. Solid State Physics 23, F.Seitz, D: Turnbull and H. Ehrenreich, Editors. *Academic Press, New York*.(1969).
- [54] Giovanni Onida, Lucia Reining, R. W. Godby, R. Del Sole, and Wanda Andreoni. Ab Initio Calculations of the Quasiparticle and Absorption Spectra of Clusters: The Sodium Tetramer. *Phys. Rev. Lett.* 75, 818, (1995).
- [55] R. W. Godby. Topics in Applied Physics. Springer, New York, 69 (1992).
- [56] David Bohm and David Pines. A Collective Description of Electron Interactions. I. Magnetic Interactions. *Phys. Rev.* 82, 625 (1951).
- [57] David Bohm and David Pines. A Collective Description of Electron Interactions: II. Collective vs Individual Particle Aspects of the Interactions. *Phys. Rev.* 85, 338 (1952).
- [58] David Bohm and David Pines. A Collective Description of Electron Interactions: III. Coulomb Interactions in a Degenerate Electron Gas. *Phys. Rev.* 92, 609 (1953).
- [59] Stephen L. Adler. Quantum Theory of the Dielectric Constant in Real Solids. *Phys. Rev.* 126, 413 (1962).
- [60] E. E. Salpeter and H. A. Bethe. A Relativistic Equation for Bound-State Problems. *Phys. Rev.* 84, 1232 (1951).
- [61] F. Aryasetiawan, O. Gunnarsson. The GW Method. *Rep. Prog. Phys.* 61, 237 (1998).
- [62] G. Baym and L. P. Kadanoff. Conservation Laws and Correlation Functions. *Phys. Rev.* 124, 287 (1961).
- [63] G. Baym and L. P. Kadanoff. Conservation Laws and Correlation Functions. *Phys. Rev.* 124, 287 (1961).
- [64] Arno Schindlmayr, P. Garcia-Gonzalez, and R. W. Godby. Diagrammatic self-energy approximations and the total particle number. *Phys. Rev.* B64, 235106 (2001).
- [65] R. Haydock. The recursive solution of the Schrödinger equation. *Comput. Phys. Commun.* 20, 11 (1980).
- [66] L. X. Benedict and E. L. Shirley. Ab initio $\epsilon_2(\omega)$ interaction: Application to GaN and CaF₂. *Phys. Rev.* B59, 5441 (1999).
- [67] M. Marsili. Electronic and optical properties of the (111)2 × 1 diamond surface: an ab-initio study. *Ph.D. thesis*, Universita di Roma "Tor Vergata", (2006).
- [68] R. Del Sole and R. Ghirlanda. Optical properties of semiconductors within the independent-quasiparticle approximation. *Phys. Rev.* B48, 11789 (1993).
- [69] O. Pulci, G. Onida, R. Del Sole, L. Reining. Ab initio calculation of excitonic effects in the optical spectra of semiconductors. *Phys. Rev. Lett.* 81, 5374 (1998).
- [70] G. Onida, L. Reining, A. Rubio. Electronic excitations: density-functional versus many-body Green's-function approaches. *Rev. Mod. Phys.* 74, 601 (2002).
- [71] A. Marini, R. Del Sole. Dynamical Excitonic Effects in Metals and Semiconductors. *Phys. Rev. Lett.* 91, 176402 (2003).
- [72] Mark Fox. Optical properties of solids. Oxford University Press Inc., New York, (2010).

- [73] Charles Kittel. Quantum Theory of Solids, Second Edition. John Wiley and Sons, New York (1987).
- [74] Enrico Fermi. Nuclear Physics.. University of Chicago Press, Chicago, (1974).
- [75] William Jones and Norman H. March. Theoretical Solid State physics Vol.1.. John Wiley and Sons, New York (1973).
- [76] P. A. M. Dirac. Nuclear Physics.. Proc. R. Soc. Lond. A 114, 243, (1927).
- [77] Enrico Fermi. Versuch einer Theorie der beta-Strahlen. I Z. Physik. 88, 161, (1934).
- [78] Wilson F L. Fermi's theory of Beta decay Am. J. Phys. 36, 1150, (1968).
- [79] P. A. M. Dirac. The Principles of Quantum Mechanics. Oxford University Press. (1958).
- [80] Messiah A. Quantum Mechanics. Dover Publications, New York (2014).
- [81] Landau L D and Lifshitz E M. Quantum Mechanics 3rd ed. Elsevier, Singapore (1965).
- [82] Cohen-Tannoudji C, Diu B and Laloe F. Quantum Mechanics. Wiley-VCH, New York (1990).
- [83] Weinberg S. Lectures on Quantum Mechanics. Cambridge University Press, New York (2013).
- [84] Sakurai J J. Modern Quantum Mechanics. Addison-Wesley, New York (1994).
- [85] Zeng J Y. Quantum Mechanics 3rd ed. Science Press, Beijing (2000).
- [86] Merzbacher E. Quantum Mechanics 2nd ed. John Wiley and Sons, London (1970).
- [87] Ballentine L E. Quantum Mechanics. A Modern Development. World Scientific, Singapore (2000).
- [88] Prof. Dr. Helmut Föll. Semiconductors. <http://www.tf.uni-kiel.de/matwis/amat/semi/en/>. [online; accessed on 2016-03-22].
- [89] Wikipedia. Transition dipole moment. https://en.wikipedia.org/wiki/Transition_dipole_moment. [online; accessed on 2016-03-22].
- [90] Prof. Charles G. Torre. Quantum Mechanics, Charged Particle in Electromagnetic field. <http://ocw.usu.edu/physics/classical-mechanics/>. [online; accessed on 2016-03-22].
- [91] Prof. Gang Chen Nano to Macro processes. <http://dspace.mit.edu/handle/1721.1/77604>. [online; accessed on 2016-03-22].
- [92] Prof. Richard Fitzpatrick. Quantum Mechanics, Electric dipole approximation. <http://farside.ph.utexas.edu/teaching/qmech/Quantum/node118.html>. [online; accessed on 2016-03-22].
- [93] Stefano Baroni, Stefano de Gironcoli, Andrea Dal Corso, and Paolo Giannozzi. Phonons and related crystal properties from density-functional perturbation theory. *Rev. Mod. Phys.* 73, 515 (2001).
- [94] Qi Chen, Nicholas De Marco, Yang (Michael) Yang, et al. Under the spotlight: The organic inorganic hybrid halide perovskite for optoelectronic applications. *Nano Today*. 10, 35 (2015).

- [95] H. Monkhorst, J. Pack. Special points for Brillouin-zone integrations. *Phys.Rev.* B13, 5188 (1976).
- [96] John P. Perdew, Kieron Burke, and Matthias Ernzerhof. Generalized Gradient Approximation Made Simple. *Phys. Rev. Lett.* 77, 3865 (1996).
- [97] D. R. Hamann. Optimized norm-conserving Vanderbilt pseudopotentials. *Phys. Rev.* B88, 085117 (2013).
- [98] Constantinos C. Stoumpos, Christos D. Malliakas, et al. Semiconducting Tin and Lead Iodide Perovskites with Organic Cations: Phase Transitions, High Mobilities, and Near Infrared Photoluminescent Properties. *Inorg. Chem.* 52, 9019 (2013).
- [99] Goedecker, Hartwigsen, Hutter, and Teter. Pseudopotential type: NC. *Phys.Rev.* B54, 1703 (1996).
- [100] M. Levinstein, S. Rumyantsev and M. Shur. Handbook Series on Semiconductor Parameters vol.1,2, World Scientific, London, (1996, 1999).
- [101] Kittel, C. Introduction to Solid State Physics 6th Ed, John Wiley, New York (1986).
- [102] S.B. Nam, D.C. Reynolds, et al. Free-exciton energy spectrum in GaAs. *Phys. Rev.* B13, 761 (1976).
- [103] B.A. Vojak, N.Holonyak Jr. et al. The exciton in recombination in $Al_xGa_{1-x}As - GaAs$ quantum-well heterostructures. *Solid state commun.* 35, 477 (1980).
- [104] Wahyu Setyawan, Stefano Curtarolo. High-throughput electronic band structure calculations: Challenges and tools. *Computational Materials Science.* 49, 299 (2010).
- [105] N. Bouarissa, H. Aourag1. Effective masses of electrons and heavy holes in InAs, InSb, GaSb, GaAs and some of their ternary compounds. *Infrared Physics and Technology* 40, 343 (1999).
- [106] Stefano Baroni, Stefano de Gironcoli, Andrea Dal Corso, and Paolo Giannozzi. Phonons and related crystal properties from density-functional perturbation theory. *Rev. Mod. Phys.* 73, 515 (2001).
- [107] Jacky Even, Laurent Pedesseau, Jean-Marc Jancu, and Claudine Katan. DFT and $k \cdot p$ modelling of the phase transitions of lead and tin halide perovskites for photovoltaic cells. *Phys. Status Solidi RRL.* 8, 31 (2014).
- [108] NASA Earth observatory . <http://earthobservatory.nasa.gov/Features/EnergyBalance/page4.php>. [online; accessed on 2016-04-25].
- [109] C. J. Hwang. Lifetimes of free and bound excitons in high purity GaAs. *Phys. Rev.* B8, 646 (1973).
- [110] P. Lawaetz. Valence-Band Parameters in Cubic Semiconductors. *Phys. Rev.* B4, 3460 (1971).
- [111] P. Pfeffer and W. Zawadzki. Five-level $\mathbf{k} \cdot \mathbf{p}$ model for the conduction and valence bands of GaAs and InP. *Phys. Rev.* B53, 12813 (1996).